UNIVERSITÀ DEGLI STUDI DI ROMA "TOR VERGATA"

FACOLTA' DI SCIENZE MATEMATICHE, FISICHE E NATURALI

DOTTORATO DI RICERCA IN

FISICA

XXI CICLO
2005-2008

Carbon Nanotubes for Solar Energy Conversion

Claudia Scilletta

A.A. 2008/2009

Docenti Guida: Prof. M. De Crescenzi, Dr. P. Castrucci, and Dr. E. Cappelli

Coordinatore: Prof. P. Picozza

To my love
and to my wonderful family

Index

Introduction

The exponential energy demand in the world is exhausting the available fossil fuel supply. Moreover, the energy production system based on fossil fuels has serious drawbacks in environment impact. To meet the increasing energy demand in the near future, humankind will be forced to seek environment-compatible clean alternative energy resources. Among the alternatives, solar energy stands is the most attractive, due to largest availability (120,000 TW per year), but, until now, the energy produced from solar radiation supplies a little fraction of the present energy needs. Regarding the electricity production, that produced by solar to electricity conversion is only the 0.015% of the total electricity demand. This is due to the high production cost and to the not optimized conversion efficiency. A great part of the research activity in this field is consequently devoted to increase the conversion efficiency, lowering at the same time the production cost.

It has been demonstrated that nanotechnology and nanomaterials could offer valid solutions to improve the conversion efficiency exploiting effects induced by mesoscopic scales. In this research field, the research on carbon nanotubes CNTs as building blocks for solar energy conversion devices is developing. The CNTs are composed by one or more graphene layers rolled up into cylindrical shape. Their unique optical and electronic properties, high electrochemical stability, large surface area, and cylindrical morphology able to provide reactive edges to chemical functionalization and surface modification, make them suitable for assembling innovative nanostructures for energy conversion devices.

The research activity of the group of Pr. M. De Crescenzi at Department of Physics of University of Rome “Tor Vergata” is addressed towards this direction.

The work presented in this thesis has been devoted to investigate the physical mechanisms underlying the photoresponse of MWCNTs when exploited in electrochemical cells and solid-state devices. A large part of the activity has consisted of the development of suitable strategies for the controlled growth of MWCNTs.

This thesis is structured as follows.

In Chapter 1, the state of the art of the research on solar energy conversion materials and devices are presented. In Paragraph 1.2, the principles of the most

common solar to electricity energy conversion devices, the photovoltaic cells and the photo-electrochemical cells, are described. The recent developments are as well presented. Then, in Paragraph 1.3, the recent results in employing CNTs as building blocks for new solar energy conversion devices are shown.

In Chapter 2, the structure and properties of CNTs are reported. After a brief historical excursus in Paragraph 2.1, the geometrical structure is described in Paragraph 2.2. In Paragraph 2.3, a large dissemination about theoretical predictions and experimental tools, useful to investigate the electronic nature of carbon nanotubes, is performed starting from the electronic structure of a single layer of graphene. In Paragraph 2.4 the theoretical predictions and experiments on MWCNTs electronic are shown. Despite the close similarity of MWCNTs to graphite, their density of states (DOS) show singularities similarly to the SWNTs DOS.

The experimental growth and characterization of MWCNTs is presented in Chapter 3. First, the most common techniques of deposition are described besides the growth model for nanotubes synthesised by Chemical Vapour Deposition (CVD). In Paragraph 3.3 the experimental set-up and synthesis process are described with techniques able to examine the morphology and the structure of MWCNTs product. It is shown also how, by these characterization techniques, it is possible to set the growth parameters in order to have a controlled growth of MWCNTs. Finally, in Paragraphs 3.4 and 3.5, the results on metal nanoparticles decoration of nanotubes and selective growth on patterned substrate are shown.

In the last Chapter 4, the different experiments on photocurrent generation from MWCNTs based devices are described and the relative results demonstrated. In Paragraph 4.2, photoelectrochemical MWCNT properties are studied. The interpretation of the basic mechanism for the e-h pair production is given, related to the presence of singularities in their DOS and obtained by analysing their electron energy loss spectrum (EELS). The influence of metal nanoparticles decoration is shown as well as the comparison of the photocurrent yield as a function of the radiation incident wavelength. A general model for the steady-state current generation from bare and functionalised MWCNTs is proposed. In Paragraph 4.3, solid-state experiments and their results are presented. Also in this kind of experiments, our

MWCNTs samples are able to produce current under illumination. An interpretation is given on the basis of theoretical calculations of DOS for a specific four-wall carbon nanotube (4WCNT). From these calculations, also the absorbance of our device is simulated. The theoretical calculations and simulations are in agreement with the experimental results (EELS spectrum and the incident photon to generated charges ratio spectrum). Also in this case a general model for the steady-state photocurrent generation is proposed. Finally, the first attempt to realize a PV cell with our MWCNTs is shown in Paragraph 4.4, comparing its performance with those of an actual silicon cell.

This work has been performed in close collaboration with the group DiaC^3 directed by Dr. E. Cappelli of CNR ISC (Institute of Complex Systems). It has been partially supported financially from the Italian Foreign Affairs Ministry through Promotion and Cultural Cooperation Management, from Health Ministry and ISPESL through the strategic project entitled: "*Innovative Methodologies for Risk Evaluation Derived from Job Exposition to Nano-materials*", and from the PRIN 2005 project "*Carbon nanotubes based electronic and optoelectronic devices*", funded by the Ministry of Education, University and Research.

Chapter 1

Solar Energy Conversion Materials: State of the Art

In this Chapter the reasons supporting the research on energy sources alternative to fossil fuels are shortly described. The attention is focused on the renewable energy and in particular on the solar energy converted into electricity. The principles of photovoltaic (PV) effect and a description of the first generation photovoltaic cell based on Si technology are summarized. The most promising development and realization of conversion devices alternative to the silicon PV cell, such as semiconductor multi-junction cells or quantum dot materials, to enhance the cost-effective conversion efficiency are reported.

Then the operative principles of photo-electrochemical cells are introduced as well as a description of the promising dye synthesized solar cells.

Finally the state of the art in the use of carbon nanotubes (CNTs) as building blocks to assembly new solar energy conversion device are described. The parallel development of photo-electrochemical cells based on single wall nanotubes (SWNTs) and the study of the properties suitable to realize solid-state conversion device are presented.

1.1 The reasons for the research on energy sources alternative to fossil fuels

Abundant availability of clean energy is one of the greatest challenges facing the world in the 21st century. The dependence on oil and electricity has made energy a vital factor of our everyday needs. In the 20th century, the population quadrupled and our energy demand went up 16 times. The exponential energy demand is exhausting the available fossil fuel supply [1]. About 13 TeraWatts (TW) of energy is currently needed to 6.5 billion people worldwide.

Emergence of more than a billion new consumers from developing countries with a newly acquired spending capacity is increasing global CO_2 emission at an alarming rate [2]. The consumer growth in the emerging countries undermines the demand for additional energy resources and the overall impact on the environment. According to Hubbert [3], the exponential growth experienced in the last century is a *transient phenomenon*, and the fossil fuel production will follow the trend of a bell shaped curve Fig. 1 (successively modified by Campbell [4, 5] and Deffeyes [6], Fig.2).

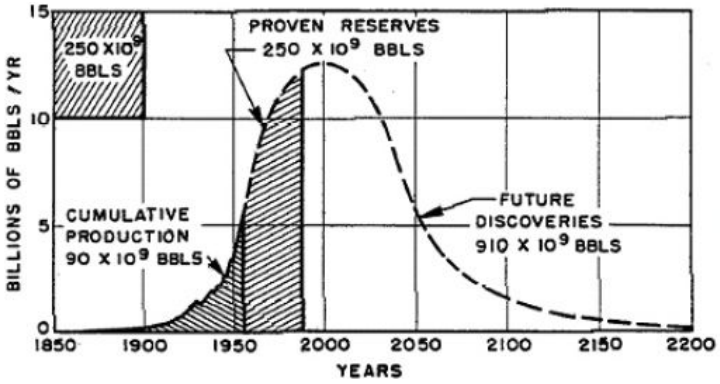

Fig. 1. Diagram of oil production proposed by Hubbert in 1956.

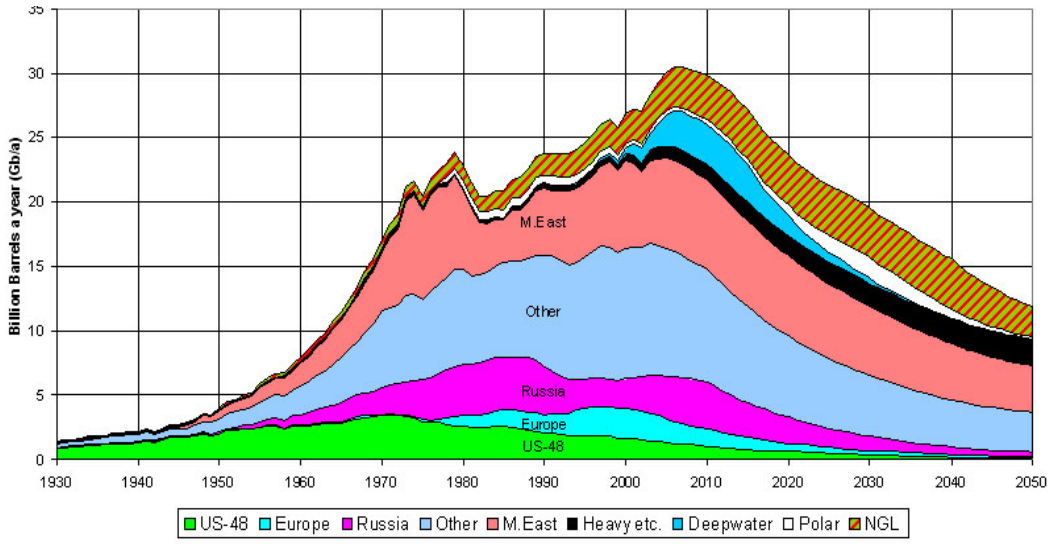

Fig. 2. Oil and gas liquids 2004 scenario from 1930 to present day and forecast (ASPO, 2004). In the legend *Heavy, Deepwater, Polar* and *NGL* are unconventional petroleum (http://www.peakoil.net).

According to this prediction, the peak production will be attained within the next decade. Coal and natural gases are likely to supplement the energy needs but this fossil fuel production will follow the Hubbert's peak before the end of this century. Diversification of energy supply as well as political and social compromise for conservation will become inevitable if we need to maintain a healthy global economic growth [1, 7-8].

Another important drawback in increasing the energy production system based on fossil fuels is its impact on the environment. Global warming from the fossil fuel greenhouse gases, which contribute to the climate changes, is becoming a major concern [9]. The United Nations Framework Convention on Climate Change calls for "*stabilization of greenhouse-gas concentrations in the atmosphere at a level that would prevent dangerous anthropogenic interference with the climate system 10 TW of carbon-emission-free power needs to be produced by the year 2050, almost equivalent to the power provided by all of today's energy sources combined*" [10].

In order to meet the increasing energy demand in the near future, humankind will be forced to seek environment-compatible clean alternative energy resources [8, 10]. Three major options are actually available: carbon neutral energy (fossil fuel in conjunction with carbon sequestration), nuclear power, and renewable energy. If we have to produce 10 TW energy using fossil fuels without affecting the environment, we need to find secure storage for 25 billion metric tons of CO_2 produced annually. If choosing the nuclear power as alternative energy source, we will require construction

of a new 1 GW-electric nuclear fission plant everyday for the next 50 years somewhere on the planet. Renewable energy can be tapped from the available resources: hydroelectric resource (0.5 TW), from tides & ocean currents (2 TW), geothermal integrated over all of the land area (12 TW), globally extractable wind power (2-4 TW), and solar energy striking the Earth (120,000 TW). Among these options, solar energy stands out as the most viable choice to meet the needed energy demand.

Sunlight is today converted into electricity by exciting charge carriers in a solar cell. Solar photons can yield chemical fuel via natural photosynthesis in green plants or artificial photosynthesis in human-engineered systems. Concentrated or un-concentrated sunlight can produce heat for direct use, or further conversion to electricity (Fig. 3).

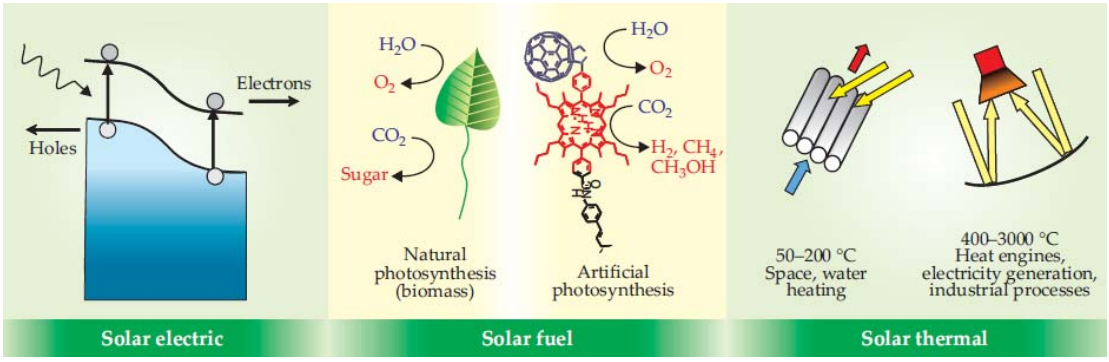

Fig. 3. Types of possible sunlight exploitations [11].

Despite this huge resource, the energy produced from solar radiation supplies a little fraction of the energy needs. For example solar electricity supply just 0.015% of the total electricity demand. This is due to cost (the solar electricity costs between 5 and 10 times the electricity from the fossil fuel) and conversion capacity, namely conversion efficiency. The cost and capacity limitations on solar energy exploitation are most effectively addressed by a single research objective: cost-effectively raising conversion efficiency. The best commercial solar cells based on single-crystal silicon are about 18% efficient. Laboratory solar cells based on cheap dye sensitization of oxide semiconductors are typically less than 10% efficient, and those based on even cheaper organic materials are 2-5% efficient [11].

Those efficiencies are far below their theoretical limits. The capacity to design nanostructured semiconductors, organic-inorganic hybrid assemblies, and molecular assemblies opens up innovative ways to create a new generation of solar energy

conversion devices that can deliver high efficiency devices at economically viable costs.

During the past decade, nanomaterials have emerged as the new building blocks to construct light energy harvesting assemblies. Organic and inorganic hybrid structures, that exhibit improved selectivity and efficiency toward catalytic processes, have been prepared. Size dependent properties such as size quantization effects in semiconductor nanoparticles and quantized charging effects in metal nanoparticles provide the basis for developing new and effective systems [12-15]. These nanostructures provide innovative strategies for designing next generation energy conversion devices [16-21]. Strategies to integrate ordered assemblies of semiconductor and metal nanoparticles, organic-inorganic hybrid systems, and carbon nanostructures in the energy conversion schemes are discussed in the following sections.

1.2 Principles of the most common solar to electricity energy conversion mechanism.

1.2.1. The solar spectrum.

Solar radiation is the electromagnetic energy emitted by fusion processes of the hydrogen contained into the sun into Helium atoms. Its spectrum is very close to that of a black-body at temperature of about 5900 K.

The sun irradiates through the space a light characterized by an electromagnetic spectrum ranging from 0,2 μm up to more than 5 μm, i.e. from Ultraviolet (UV) to Infrared (IR) radiation through the visible light. The solar radiation spectrum outside and inside the Earth's atmosphere, with the characteristic absorption bands of gas molecules composing it, is reported in Fig. 4.

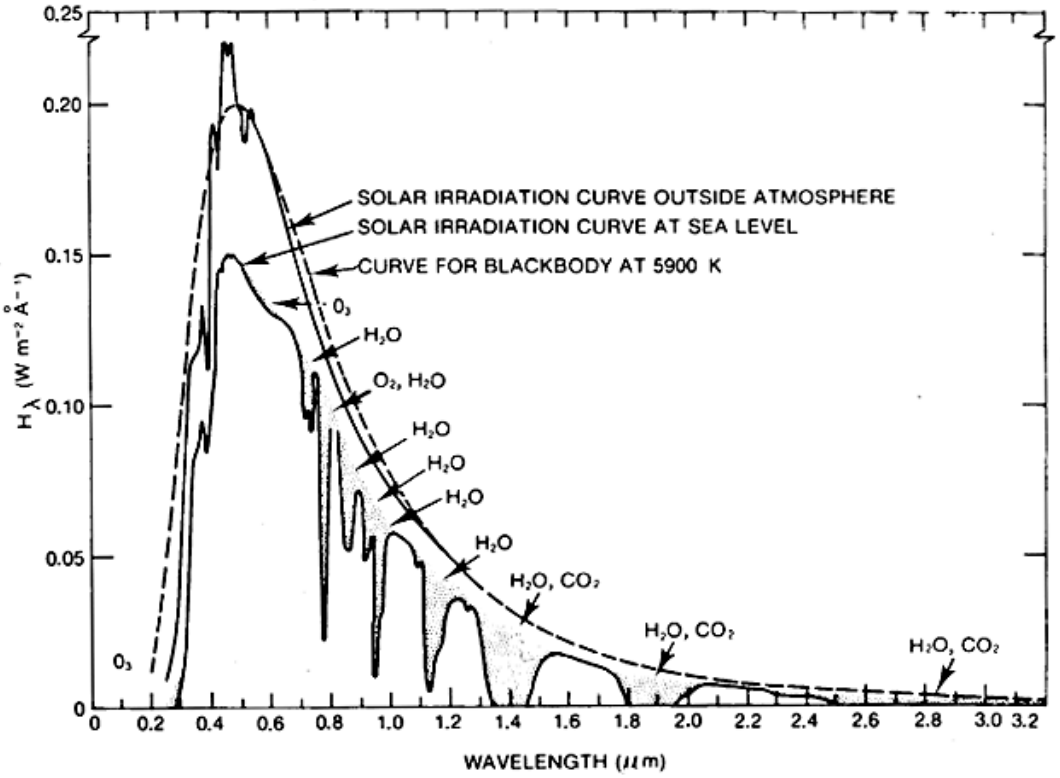

Fig. 4. Solar irradiation curves outside and inside the Earth's atmosphere. The absorption bands are labeled with the names of the molecules which cause radiation absorption.

1.2.2 PV solar cells: principles and state of the art.

The Photovoltaic effect is known since 1839 thanks to the work of the French physicist A.E. Becquerel (1820-1891), who presented to the Science Academy of Paris his "*Mémoire sur les effets électriques produits sous l'influence des rayons solaires*". The discovery accidentally occurred during experiments on an electrochemical cell in which two platinum electrodes were immersed. For a long time it remained a scientific phenomenon with few device applications. In 1870 the PV effect was studied by H. Hertz on solid-state selenium and, in 1876, by Smith, Adam, and Day which prepared such devices converting solar energy into electricity with an efficiency of 1-2%. The development of PV effect as an energy source was hindered by the low yield of the used materials. Only in 1954 Person, Fuller, and Chaplin [22] obtained the first silicon-based PV module at the Bell Laboratory. Owing to the introduction of silicon as the standard industrial semiconductor material in the late 1950s, silicon PV diodes became available.

A PV solar cell is basically a semiconductor p-n diode. The semiconductor material absorbs the incoming photons and converts them into electron-hole pairs.

The fundamental parameter is the semiconductor bandgap energy E_G (~1.1 eV for Si). In an ideal case, no photons with an energy hν < E_G will contribute to photogeneration, whereas all photons with an energy hν > E_G will each produce an electron-hole pair. The excess energy (hν - E_G) is very rapidly lost because of thermalization (Fig. 5). The maximum limit for the photogenerated electric current density J_{ph} is therefore given by the flux of photons with an energy hν > E_G. Thus J_{ph} decreases with an increasing of E_G. At the same time, the net energy transferred to each electron-hole pair increases, as it is equal to E_G. There exists an "optimum" value for E_G for which a maximum of energy can be transferred from the incident sunlight to the totality of photogenerated electron-hole pairs. At this bandgap, roughly half of the incident solar energy is transferred.

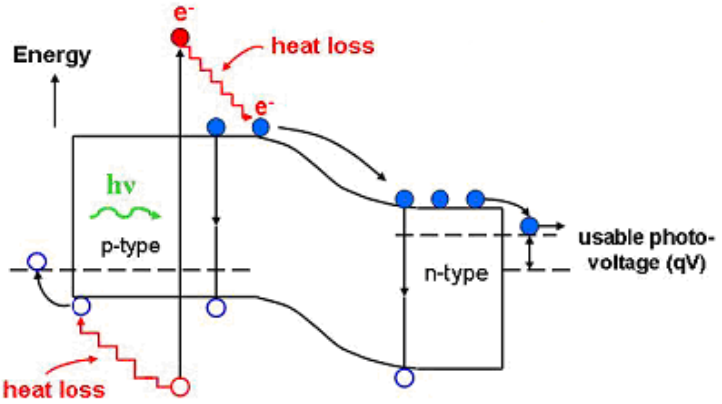

Fig. 5. Schematic picture showing the interaction of a p-n junction with photon of different energy. Photons with energy smaller than the semiconductor energy bandgap, hν < E_G, are not absorbed, while photons with energy exceeding E_G are absorbed producing a charge pair. The energy excess (hν - E_G) is lost by thermalization. The charge carriers are separated and collected by the photovoltage.

The second step of the energy conversion process, the photogenerated electron-hole pairs are separated, with electrons drifting to one electrode and holes drifting to the other electrode, because of the internal electric field created by the p-n junction structure of the solar cell. The dark (non illuminated) and the photogenerated characteristics of the photodiode can be linearly superimposed. The resulting solar cell equivalent circuit is shown in Fig. 6A and the relative I-V characteristics are shown in Fig. 6B. The characteristic parameters of solar cells are: short circuit I_{sc}, open circuit V_{oc}, and fill factor FF.

The fill factor is essentially a measure of quality of the solar cell. It is calculated by comparing the maximum power to the theoretical power that would be output at both the open circuit voltage and short circuit current together. The fill factor is a

parameter that takes into account the form of the I-V curve under irradiation, being the ratio between the maximum area of the inscribable rectangle, P_{max}, and the rectangle identified by I_{sc}, and V_{oc} :

$$FF = \frac{P_{\max}}{I_{sc} \cdot V_{oc}}, \tag{1}$$

the maximum limit for I_{sc} is given by the photogenerated current density I_{ph}.

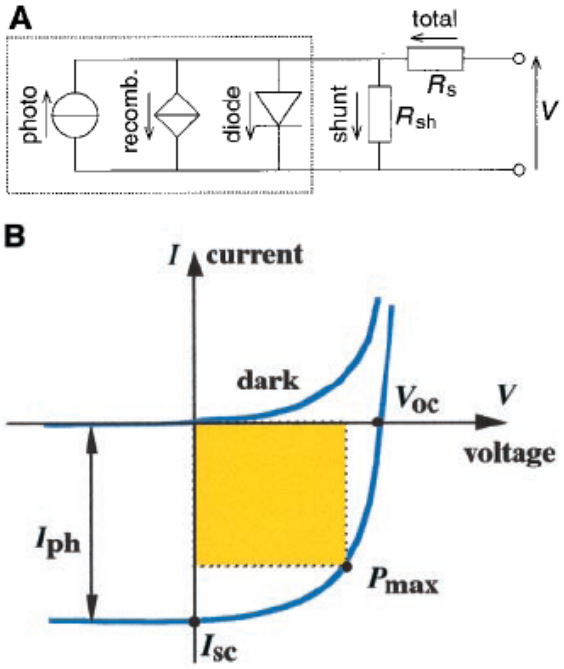

Fig. 6. Equivalent circuit (A) and the I-V characteristics (B) of a p-n PV solar cell.

To test the performance of the PV cell the efficiency η is evaluated. The efficiency is defined as:

$$\eta = \frac{P_{\max}}{E \times A_{cell}}, \tag{2}$$

where E is the irradiance of radiation (W/m^2) and A_{cell} is the illuminated area of the cell. It is worth to notice that η has to be distinguished from the quantum efficiency, QE at fixed photon energy ($h\nu$) (or equivalent the incident photon conversion efficiency, $IPCE$) that is defined as the ratio between the number of generated charges, $N_{e\text{-}h}$, and the number of incident photons N_{ph}:

$$QE(h\upsilon) = IPCE(h\upsilon) = \frac{N_{e-h}}{N_{ph}(h\upsilon)}. \tag{3}$$

QE takes into account the charge photogeneration capability of materials, independently from the electrical performance of the resulting device.

The loss of photon energy into heat is one of the reasons why the calculated maximum efficiency of conventional solar cells is limited to about 32%. Other reasons are represented by the reflection of photon onto the cell surface, the electron-hole pair recombination before to be collected by the electrodes, the presence of shunt resistances at the semiconductor/metal junctions.

The overall conversion efficiency depends on each of the described mechanisms. Monocrystalline Si cells reach an efficiency of 25% at a laboratory level, while for commercial modules the efficiency is about 15%.

Recently, different devices have been designed to increase the overall efficiency. Stacked cells composed by semiconductor of different bandgap allow to absorb a greater fraction of the solar spectrum enhancing the overall conversion efficiency. These are referred to as "multijunction" cells (also called "cascade" or "tandem" cells). Much of today's research in multijunction cells focuses on III-V semiconductors as cell components. Such cells have reached efficiencies of around 35% under concentrated sunlight, but their production costs are remarkably high.

The most dramatic and surprising potential increase in efficiency comes from nanotechnology application. For example, in quantum-dots, carrier multiplication [23, 24] allows the generation of multiple electron-hole pairs for a single incident photon. Theoretical efficiencies exceeding 60% would, in principle, be achievable. Then, absorbers having a highly quantized band structure, such as quantum wells and quantum dots, can theoretically produce the desired effects (Fig. 7).

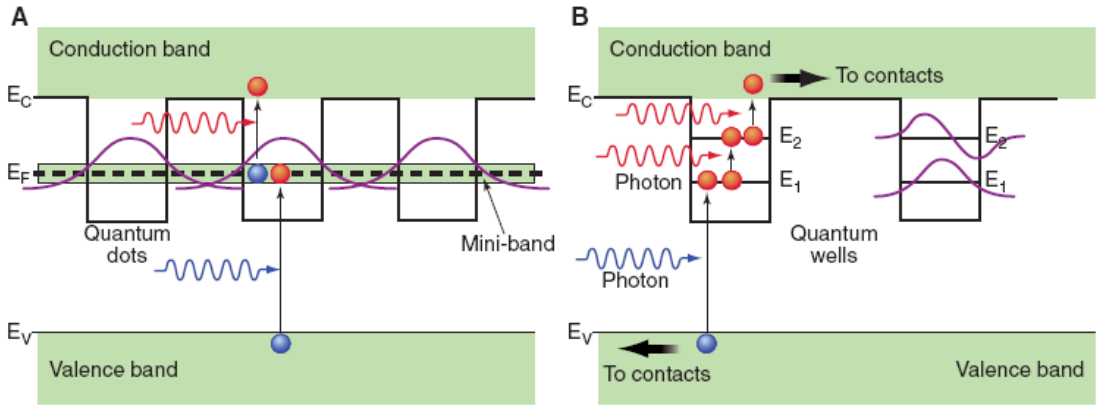

Fig. 7. Possible methods of circumventing the 31% efficiency limit for thermalized carriers in a single–band gap absorption threshold solar quantum conversion system. (A) Intermediate-band solar cell; (B) quantum-well solar cell [25].

In fact, recent observations on PbSe quantum dots have demonstrated the production, with high quantum yield, of multiple excitons from a single absorbed photon, thereby establishing an existence proof for the process of interest [23]. At present, however, there is no method for efficiently extracting the photogenerated carriers from the quantum dot structure to produce electricity in an external circuit. Materials with “mini-bands” or with “intermediate bands” also offer the possibility for ultrahigh energy conversion efficiency [23]. According to this approach, different incident photon energies would promote absorption from different isolated energy levels and therefore allow for the production of different voltages (Fig.7). The phenomenon has been described theoretically but has yet to be demonstrated in a practical implementation. In addition, these materials are currently extremely costly, and methods of retaining the high performance with scalable, inexpensive manufacturing methods should also be required.

1.2.3 Photo-electrochemical solar cells: principles and state of the art

Photo-electrochemical (PEC) systems represent the best-known wet chemical method to converting sunlight into electrical energy or chemical fuels. PEC cells developed during the mid-1970s and 1980s for capture and conversion of solar energy into electricity and fuels worked with a semiconductor electrode in contact with an electrolyte solution (Memming 2001; Bard et al. 2002; Nozik and Memming 1996; Nozik 1978; Grätzel 2001).

In a first configuration (called an electrochemical photovoltaic (EPV) cell), a semiconductor is in contact with an electrically conducting liquid, the electrolyte, that is able to provide a redox reaction that can readily transfer electrons to an electrode and can accept electrons from the other electrode (Fig. 8). The semiconductor forms a junction with the liquid by simple immersion and develops an electric field at its surface. The semiconductor can be n-type or p-type. Upon illumination of the semiconductor, the photogenerated electrons and holes can separate because of the surface electric field. For n-type semiconductors, the holes move to the surface and are captured by a redox couple; the electrons move to the back side of the semiconductor, where they leave the cell via an electrical contact, deliver electrical power to an external load, and then return to the cell by means of the second

electrode. Here, they are scavenged by the redox species that initially had captured the hole at the semiconductor surface; this process returns the redox species to their original chemical condition. Thus the redox couple accepts holes at one electrode and accepts electrons at the other electrode, resulting in charge neutralization and no net change in the redox species. The electrolyte and redox couple just serves to complete the electrical circuit and to produce the electric field required for charge separation.

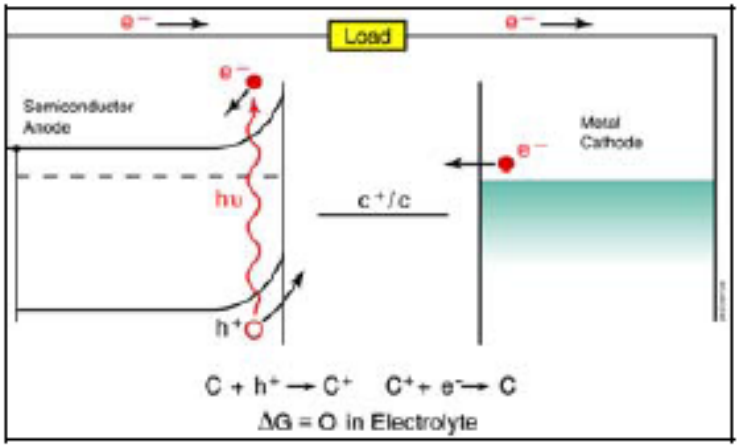

Fig. 8. Schematic picture of the basic mechanisms for photocurrent generation in electrochemical photovoltaic cells (EPV).

Hence, in a typical photochemical solar cell, a semiconducting film serves as a photoactive electrode that, under excitation of visible light, generates electron-hole pairs. As one of the charge carriers (e.g. the electron) is driven to the counter electrode, the other charge carrier (e.g. the hole) is scavenged by a redox reaction.

New architecture of inorganic nano-crystalline semiconductors and molecular structures [26] are being developed to enhance the performance of a photoelectric solar cell such as overall conversion efficiency and the lifetime of the active electrode besides a reduction of the costs.

Dye-sensitized solar cells (DSSC), invented by M. Graetzel and collaborators in 1991, introduce a new concept solar conversion device and represent a feasible alternative to p-n junction photovoltaic devices [27]. In contrast to the conventional semiconductor systems, where the expensive semiconductor assumes both the task of photon capture and charge transport, these two functions are separated in the DSSC. A hybrid system, formed by a chemical dye and the inexpensive wide-bandgap semiconductor TiO_2 nanoparticles, replaces the bulk semiconductor. Light is absorbed by the sensitizer, while the charge separation takes place at the interface via photo-induced electron injection from the dye into the conduction band of the solid. Charge

carriers are then transported from the conduction band of the semiconductor to the charge collector. The holes left in the dye molecule recombines with the electrons carried to it through an electrolyte from the counter electrode by an anion. The use of sensitizers, having a broad absorption band, in conjunction with optically–transparent electrically-conducting oxide films of nanocrystalline structure, permits to harvest a large fraction of sunlight. The conversion of incident photons into electric current is achieved over a large spectrum ranging from the UV to the near IR region. Overall solar radiation to electric current conversion efficiencies of 10.6% have been reached.

In Fig. 9 the operation principles and energy level scheme of dye-sensitized nanocrystalline solar cell are drawn [28]. Photoexcitation of the sensitizer (S) is followed by electron injection into the conduction band of a semiconductor oxide film. The dye molecule is regenerated by the redox system, which itself is regenerated at the counter electrode by electrons passing through the load. The open-circuit voltage of the solar cell corresponds to the difference between the redox potential of the mediator and the Fermi level of the nanocrystalline film indicated with a dashed line.

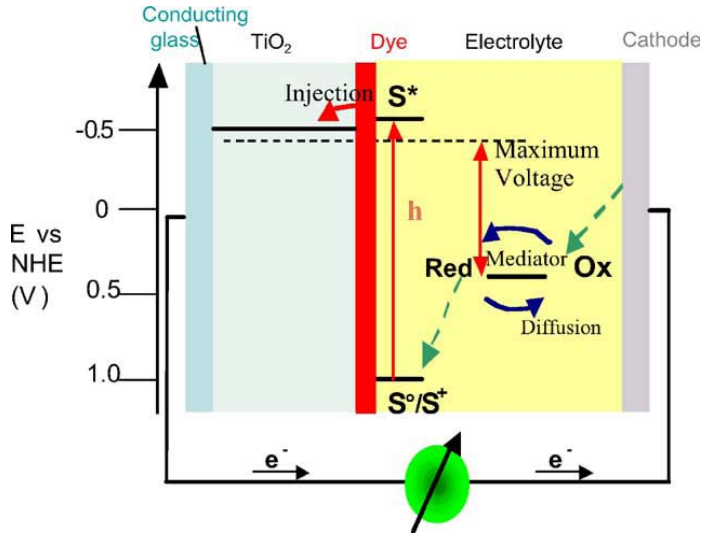

Fig. 9. Principle of operation and energy level scheme of the dye-sensitized nanocrystalline solar cell. Photoexcitation of the sensitizer (S) is followed by electron injection into the conduction band of an oxide semiconductor film. The dye molecule is regenerated by the redox system, which itself is regenerated at the counter-electrode by electrons passed through the load. Potentials are referred to the normal hydrogen electrode (NHE). The open circuit voltage of the solar cell corresponds to the difference between the redox potential of the mediator and the Fermi level of the nanocrystalline film indicated with a dashed line. The energy levels drawn for the sensitizer and the redox mediator match the redox potentials of the doubly deprotonated N_3 sensitizer ground state and the iodide/triiodide couple.

1.3 Carbon Nanotubes (CNTs) as building blocks for new solar energy conversion devices

The unique optical and electronic properties, high electrochemical stability, large surface area, and cylindrical morphology providing reactive edges to chemical functionalization and surface modification, have prompted many researchers to employ carbon nanostructures assemblies for energy conversion devices [29].

The simplest carbon nanotube is composed by a graphene, a single sheet of a honeycomb network of carbon atoms, rolled up seamlessly into a tubular shape [30]. The first discovered carbon nanotubes were composed of multi-tubes (multi-wall tubes, MWNT) nested in a concentric way [31]. Later, a single-wall carbon nanotube, SWNT, was discovered by Iijima himself [32]. Since the first reports, CNTs have been subject of intense interest for basic and applied research. Interest in carbon nanotubes is driven by their exceptional electronic, optical, thermal, and mechanical properties [30, 33]. In particular, depending on the way the sheet is rolled up (i.e. its chirality) the CNT may show metallic or semiconducting properties (while a graphene layer is a semi-metal). Semiconducting nanotubes are direct bandgap semiconductors with $E_G \approx 0.8/D$ (eV), where D is the nanotube diameter in nanometers. The work function of SWNT bundles is known to be about -4.8 eV [34].

Recently researchers have used SWNTs as building blocks for solar energy conversion devices in chemical cells. Two different approaches have to be considered for the use of carbon nanotubes in solar cells (Fig. 10): (i) direct bandgap excitation of semiconducting nanotubes; or (ii) the use of conducting tubes as low-impedance conduits to improve the transport of charge carriers from light-harvesting nanoassemblies.

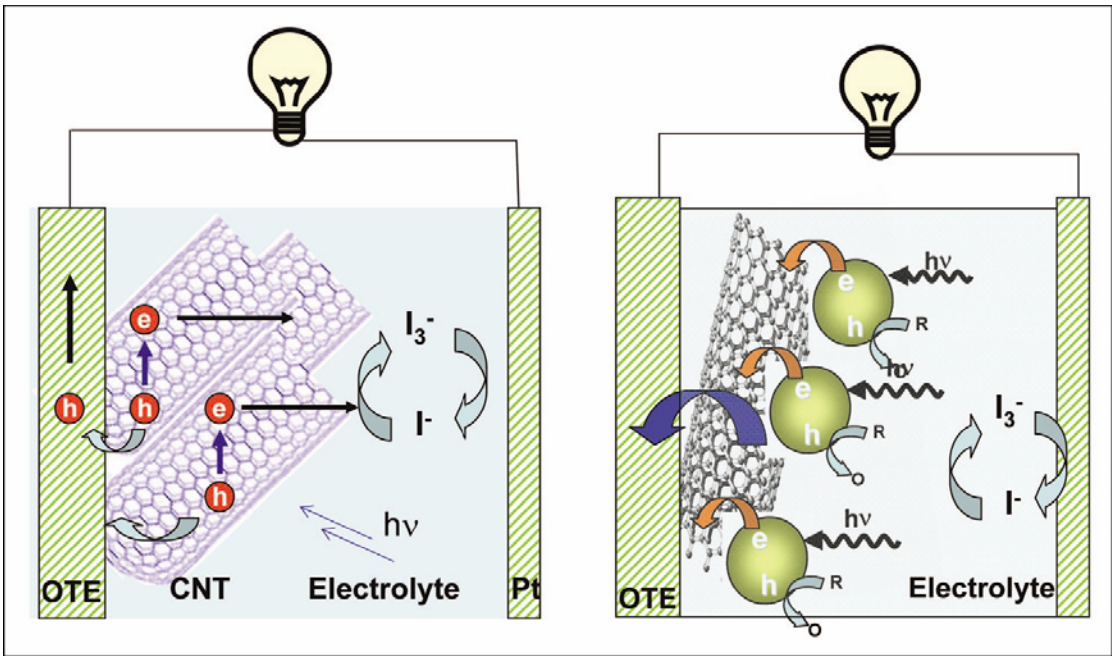

Fig. 10. Schematic picture of CNT based photoelectrochemical cells. The nanotubes can be used to produce the charges (picture on the left) and to collect and transport the charges in hybrid structures (picture on the right).

(i) Semiconducting SWNTs seem to be very promising optoelectronic materials. First semiconducting nanotubes have a direct gap. This is a desirable property for an optoelectronic material since it allows optical transitions to proceed without the intervention of phonons. Furthermore, the low dimensionality leads to a diverging density of states (Fig. 11) at the band edge, defined as van Hove singularities. That allows electronic transitions among singularity pairs, making several features emerge in the optical absorption spectrum in the visible and near IR range [35-37].

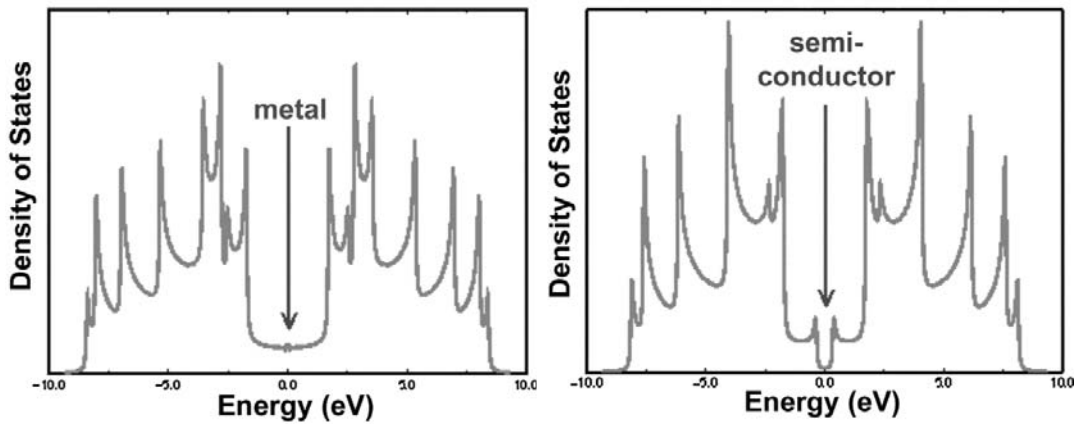

Fig. 11. DOS exhibiting the valence and the conduction band for a metallic tube, which shows electronic states at the Fermi level, and for a tube revealing semiconducting behavior due to the presence of an energy gap. The spikes shown in the DOS of the tubules are called van Hove singularities and are the result of the one-dimensional quantization, which is not present in an flat graphite single layer.

Finally, their one-dimensional confinement causes a strongly Coulombic coupling between the photogenerated electron-hole pairs, resulting in strongly bound excitons [38, 39]. The lifetime of such states is very long ($\tau \sim 10^{-9}$ sec) in CNTs in respect to the lifetime of excited states in solids ($\tau \sim 10^{-16}$ s to 10^{-14}). This allows the electrolyte to separate the charges: the electrons (holes) are driven away to the collecting electrode surface and the holes (electrons) are scavenged by the redox producing a steady current.

The first experiment on a similar solar cell was performed by Kamat et al. [40]. He measured the photoresponse of a SWNTs film in a PEC cell after excitation under visible light. This photoresponse extends up to the visible-red region, in agreement with the absorption spectrum. The maximum generated photocurrent was 8 $\mu mA/cm^2$ for a wavelength of 400 nm, while the maximum incident photon conversion efficiency was only 0.15%. This value was very low, but they showed for the first time the photovoltaic property that characterizes the p-type semiconducting nature of single-wall carbon nanotubes. Recently, the group directed by Prof. De Crescenzi at Tor Vergata University demonstrated that also MWCNTs are able to generate a significant photocurrent if exposed under a monochromatic radiation ranging from visible to UV radiation [41]. In this work MWCNTs show photon-to-current conversion efficiency at maximum up to 7% at 350nm, about 50 times higher than that of SWCNTs. This is very surprising owing to the fact that, for SWNT the current generation can be ascribed to the Van Hove singularities that were theoretically calculated and experimentally verified, while for MWNTs no ab-initio calculation has been yet achieved. On the contrary, current generation under light irradiation was unexpected due to the close similarity of a MWNT to the graphite structure (number of walls > 9 in [41]).

(ii) A lot of work has been made to prepare photochemical solar cells based on new hybrid architectures that exploit carbon nanotubes, in particular single-wall, to improve the capture of photogenerated charges and their transport to the electrode surface.

SWNTs are ideal candidates as conduits for collecting and transporting charges across light-harvesting assemblies (e.g. semiconductor particles). A CdS-SWNT composite has shown unusually high efficiency, generating a photocurrent from visible light [42,43], while using SWNT as conducting scaffolds in a TiO_2-based

photoelectrochemical cell can increase the conversion efficiency by a factor of 2 [44] (Fig.12).

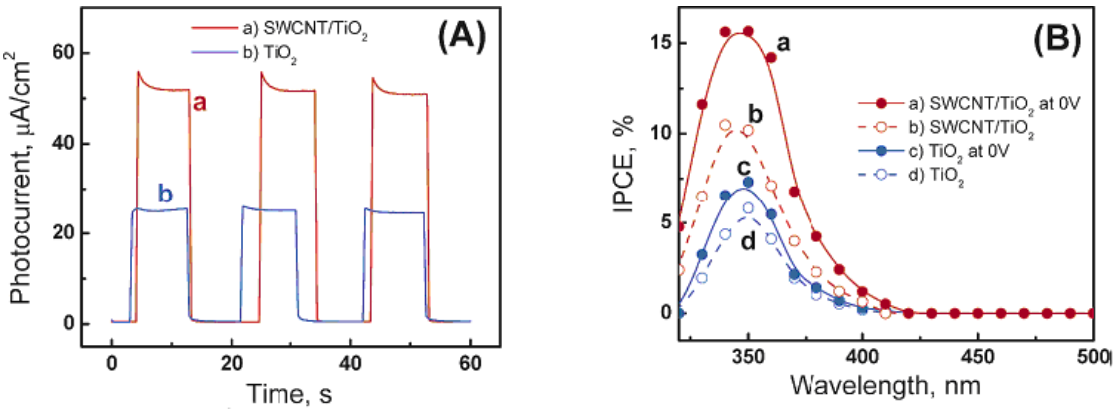

Fig. 12. (A) Photocurrent response vs time of SWCNT/TiO2 (a) and TiO2 (b) electrodes at 0 V vs SCE, with a light intensity of 50 mW/cm^2 ($h\nu$ > 300 nm). (B) *IPCE* spectra of SWCNT/TiO2 (a, b) and TiO2 (c, d). The electrodes are at a floating applied bias (b, d) and at 0 V (a, c). Electrolyte was a N_2-saturated 1M KOH solution [44].

Another successfully utilization of SWNT is represented by the realization of organic/inorganic solar cells. SWNTs have a characteristic curve-shaped surface that facilitates binding of larger organic molecules via non-covalent or hydrophobic interactions. Molecules as porphyrins have an affinity to bind non-covalently with SWNTs through π-π interactions. The interaction between porphyrins and SWNTs can be modulated to achieve a supramolecular assembly. Exploiting this property, ordered assembly of SWNT with porphyrin systems as photoactive electrode of a photoelectrical solar cell have been realized and their performance have been tested [45-47]. These systems give rise to promising solar-energy conversion efficiencies (up to 8.5% internal photoconversion efficiencies (*IPCE*) [46]).

Besides the research on photo-electrochemical cells, also the possibilities to exploit the nanotubes to realize solid-state devices generating current under illumination are undergoing intense research study. Initially the optoelectronic properties of nanotubes has been studied. Electrically induced polarized IR optical emission have been experimentally observed from SWNT field-effect transistor (FET) [48] giving rise to the possibility to fabricate nanotube-based optical emitters in the infrared range. At the same time photoconductivity of SWNTs [49-51] has been

observed, outlining the possibility to fabricate nanotube optical detectors over a wide IR and visible range. Freitag [49] measured the infrared laser-excited photoconductivity from a single carbon nanotube constituting the channel of a field-effect transistor (FET). In his experiment the e-h couples generated within the nanotube have been separated by an electric field applied between the metallic contacts. He ascribed the photocurrent generation to the resonant excitation of the semiconducting nanotube second exciton state with an estimated quantum efficiency of about 10%. A further step is the experiment of Mohite on the photoconductivity of a SWNTs film. In this experiment, a film of semiconducting and a film of metallic SWNTs are deposited on a glass slide which are then anchored to a copper block. Contact to the SWNTs is performed by attaching a gold wire to the film surface using silver paint. The sample is illuminated by a pulsed light tunable from 0.4 to 4.0 eV; a scheme of the device and measurement is reported in Fig. 13.

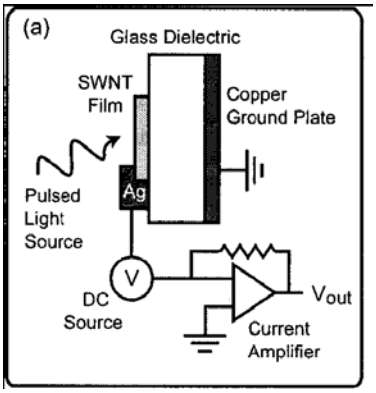

Fig. 13. Sketch illustrating the displacement photocurrent measurement technique [51].

The generated photocurrent shows resonances whose energies are in agreement with the energies of exciton states of both semiconducting and metallic nanotubes (van Hove transitions, Fig. 14). Moreover the constant value of the photocurrent sign suggest the existence of a built-in potential that aids the electron transfer from the SWNT/glass interface towards the silver contact.

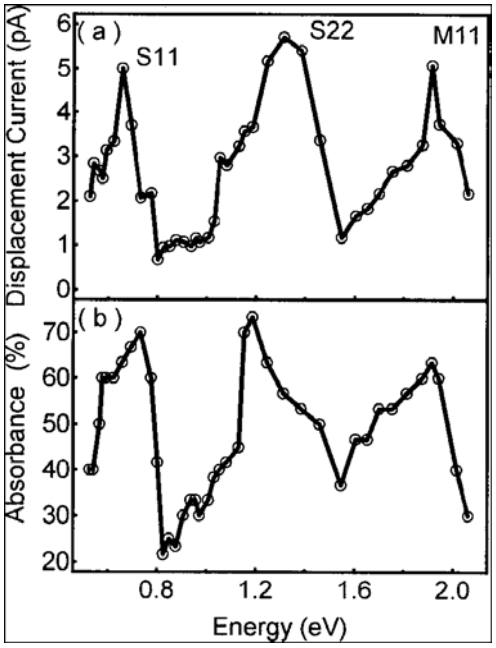

Fig. 14. (a) Peaks in the photocurrent are observed at the two lowest energy semiconductor transitions (S11 and S22) and at the lowest energy metallic transition (M11). (b) The absorbance measured for the same SWNT film under the same conditions. The generated photocurrent is directly related to the semiconducting and metallic transitions in the nanotube absorbance spectrum.

The optoelectronic properties of CNTs are often related to the presence of p-n junctions arising from an applied bias [49], a modulated chemical doping, a crossed-wire geometry [52], or the presence of non-equivalent Schottky barriers at the junctions CNTs/electrodes [49,51]. Photocurrent has been calculated in nanotube p-n junctions [53] showing multiple sharp peaks, ranging from the IR to the UV, through the visible owing to the fact all the bands in the SWNT have a direct band gap, which leads to a response over a wide energy spectrum. Lee [54] tested the PV effect of individual SWNTs forming ideal p-n junction diodes realized by using electrostatic doping [55]. The scheme of such device is shown in Fig. 15.

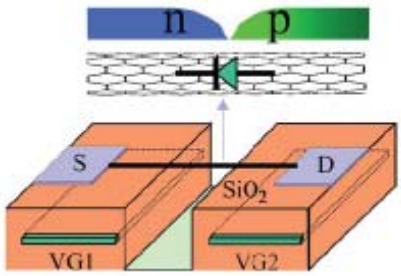

Fig. 15. Split gate device where V_{G1} and V_{G2} are biased with opposite polarities VG1=−VG2= +10 V to form an ideal p-n junction diode along the SWNT [54].

The I-V characteristics in dark conditions and under illumination of a 1.5 μm continuous laser are reported in Fig.16 as a function of the illuminated power, showing the PV behavior of the nanotube. The total efficiency η of this PV cell is estimated to be around 5% (considering the actual absorbed power).

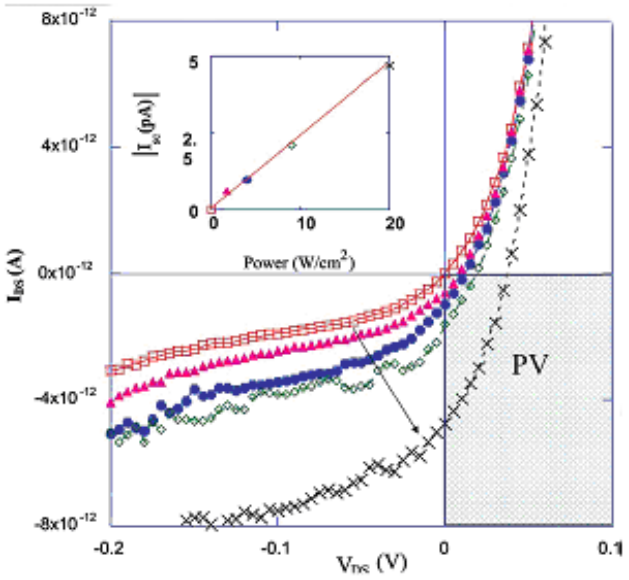

Fig. 16. I-V characteristics under increased light intensity showing a progressive shift into the fourth quadrant (PV) where the diode generates power. The inset shows the expected linear increase in the current measured at V_{DS}=0 (Isc) with illuminated power [54].

A further and recent step is the realization of a double-walled nanotube (DWNT) solar cell [56]. These solar cells consist of a semitransparent thin film of CNTs on a n-type crystalline silicon substrate to create high-density p-n hetero-junctions between nanotubes and n-Si and thus favour charge separation as well as electrons (through n-Si) and holes (through nanotubes) extraction (Fig.17). Initial tests have shown a power conversion efficiency of $> 1\%$.

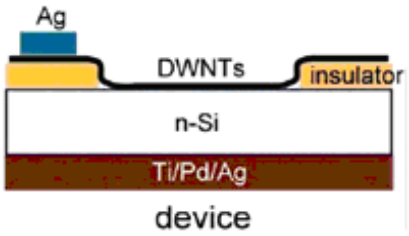

Fig. 17. Picture of the DWNT/n-Si solar cell device fabricated by Wei [56].

A question is if also MWCNTs, which have a close similarity with graphite (metallic), show photocurrent generation properties under illumination and if they can

be eventually used like materials for photovoltaic solar cell. First results have been obtained by Passacantando and coworkers on MWCNTs sheets grown on a sapphire substrate [57]. They have shown the capability of MWCNTs to generate photocurrent upon illumination with white light and monochromatic radiation in the UV–visible–near IR region.

Nonetheless many issues remain open, more in general a deep comprehension of the inner mechanisms of a steady - state current generation by MWCNTs, in photochemical cell or solid-state devices, under irradiation has to be yet carried on. This is the main aim of this thesis.

References

[1] P. B. Weisz, *Phys. Today*, July 2004, 47.

[2] N. Myers, J. Kent, *Proc. Natl. Acad. Sci. U.S.A.* **100**, 4963 (2003).

[3] M. K. Hubbert, *Am. J. Phys.* **49**, 1007 (1981).

[4] C. J Campbell, *Popul. En*V*iron.* **24**, 193 (2002).

[5] C. J. Campbell, J. H. Laherrere, *Sci. Am.* **278**, 60 (1998).

[6] K. S. Deffeyes, '*Hubbert's Peak: The Impending World Oil Shortage'*, Princeton University Press: Princeton, NJ, 2001.

[7] M. S. Dresselhaus, I. L. Thomas, *Nature* **414**, 332 (2001).

[8] A. J. Ragauskas, et al.; *Science* **311**, 484 (2006).

[9] M. E. Mann, R. S. Bradley, M. K. Hughes, *Nature* **392**, 779 (1998).

[10] M. I. Hoffert, et al, *Science* **298**, 298 (2002).

[11] G.W. Crabtree, N.S. Lewis, *Physics Today*, March 2007, 37.

[12] M. L. Steigerwald, L. E. Brus, *Acc. Chem. Res.* **23**, 183 (1990).

[13] L. E. Brus, *J. Phys. Chem.* **90**, 2555 (1986).

[14] H. Weller, *Adv. Mater.* **5**, 88 (1993).

[15] L. Banyai, S. W. Koch, '*Semiconductor quantum Dots'*, World Scientific Publishing Co.: River Edge, NJ, 1993.

[16] P. V. Kamat, *J. Phys. Chem. B* **106**, 7729 (2002).

[17] D. Adams, et al.; *J. Phys. Chem. B* **107**, 6668 (2003).

[18] K. George Thomas, P. V. Kamat, *Acc. Chem. Res.* **36**, 888 (2003).

[19] A. N. Shipway, E. Katz, I. Willner, *Chem. Phys. Chem.* **1**, 18 (2000).

[20] I. Willner, E. Kaganer, E. Joselevich, H. Durr, E. David, M. J. Gunter, M. R. Johnston, *Coord. Chem. Rev.* **171**, 261 (1998).

[21] M. D. Ward, *Chem. Soc. Rev.* **26**, 365-375 (1999).

[22] D. Chapin, C. Fuller, and G. Pearson, *J. Appl. Phys*. **25**, 676 (1954).

[23] R.D. Schaller, M.A. Petruska, V.I. Klimov, *Appl. Phys. Lett.* **87**, 253102 (2005).

[24] A.J. Nozik, *Physica E* **14**, 115 (2002).

[25] Adapted from "*Basic Research Needs for Solar Energy Utilization*", U.S. Department of Energy, Washington, DC, 2005, available on the web at http://www.sc.doe.gov/bes/reports/files/SEU_rpt.pdf.

[26] M. Graetzel, *Nature* **414**, 338 (2001).

[27] B. O'Regan, M. Graetzel, *Nature* **353**, 737 (1991).

[28] M. Graetzel, *Inorg. Chem* **44**, 6841 (2005).

[29] P.V. Kamat, *Nanotoday* **1**, 20 (2006).

[30] R. Saito, G. Dresselhaus, and M. Dresselhaus, *Physical Properties of Carbon Nanotubes*, Imperial College Press, 1998.

[31] S. Iijima, *Nature* **354**, 56 (1991).

[32] S. Iijima and T. Ichihasi, *Nature* **363**, 603 (1993).

[33] P.L. McEuen, M. S. Fuhrer, and Park Hongkun, *IEEE Trans. on Nanotechnology* **1**, 78 (2002).

[34] S. Suzuki, et al., *Appl. Phys. Lett.* **76**, 4007 (2000).

[35] J. Chen, M. A. Hamn, H. Hu, Y. Chen, A. M. Rao, P. C. Eklund, and R. C. Haddon, *Science* **282**, 95 (1998).

[36] H. Kataura, Y. Kumazawa, Y. Maniwa, I. Umezu, S. Suzuki, Y. Ohtsuka, and Y. Achiba, *Synth. Met.* **103**, 2555 (1999).

[37] Z. M. Li, Z. K. Tang, H. J. Liu, N. Wang, C. T. Chan, R. Saito, S. Okada, G. D. Li, J. S. Chen, N. Nagasawa, and S. Tsuda, *Phys. Rev. Lett.* **87**, 127401 (2001).

[38] C. L. Kane, E. J. Mele, *Phys. Rev. Lett.* **90**, 207401 (2003).

[39] T. G. Pedersen, *Phys. Rev. B* **67**, 073401 (2003).

[40] S. Barazzouk, S. Hotchandani, K. Vinodgopal, and P. V. Kamat, *J. Phys. Chem. B* **108**, 17015 (2004).

[41] P. Castrucci, F. Tombolini, M. Scarselli, E. Speiser, S. Del Gobbo, W. Richter, M. De Crescenzi, M. Diociaiuti, E. Gatto, M. Venanzi, *Appl. Phys Lett.* **89**, 253107 (2006).

[42] L. Sheeney-Haj-Ichia, et al., *Angew. Chem. Int. Ed.* **44**, 78 (2004).

[43] I. Robel, et al., *Adv. Mater*. **17**, 2458 (2005).

[44] A. Kongkanand, R. Martinez Dominguez, and P.V. Kamat, *Nanoletters* **7**, 676 (2007).

[45] T. Hasobe, et al., *J. Am. Chem. Soc.* **127**, 11884 (2005).

[46] D. M. Guldi, G. M. A. Rahman, M. Prato, N. Jux, S. Qin, and W. Ford, *Angew. Chem. Int. Ed.* **44**, 2015 (2005).

[47] T. Hasobe, et al., *J. Am. Chem. Soc.* **125**, 14962 (2003).

[48] A. Misewich, R. Martel, Ph. Avouris, J. C. Tsang, S. Heinze, and J. Tersoff, *Science* **300**, 783 (2003).

[49] M. Freitag, Y. Martin, J. A. Misewich, R. Martel, P.H. Avouris, *Nanoletters* **3**, 1067 (2003).

[50] K. Balasubramanian, Y. Fan, M. Burghard, K. Kern, M. Friedrich, U.Wannek, and A. Mews, *Appl. Phys. Lett.* **84**, 2400 (2004).

[51] A. Mohite, S. Chakraborty, P. Gopinath, G. U. Sumanasekera, and B. W. Alphenaara, *App. Phys. Lett.* **86**, 061114 (2005).

[52] M.S. Fuhrer et al., *Science* **288**, 494 (2000).

[53] D. A. Stewart, F. Leonard, *Phys. Rev. Lett.* **93**, 107401 (2004).

[54] J.U. Lee, *Appl. Phys. Lett.* **87**, 073101 (2005).

[55] J. U. Lee, P. P. Gipp, and C. M. Heller, *Appl. Phys. Lett.* **85**, 145 (2004).

[56] J. Wei,Y. Jia, Q. Shu, Z. Gu, K. Wang, D. Zhuang, G. Zhang, Z. Wang, J. Luo, A. Cao, and D. Wu, *Nanoletters* **7**, 2317 (2007).

[57] M. Passacantando, F. Bussolotti, V. Grossi, S. Santucci, A. Ambrosio, M. Ambrosio, G. Ambrosone, V. Carillo, U. Coscia, P. Maddalena, E. Perillo, and A. Raulo, *Appl. Phys Let.* **93**, 051911 (2008).

Chapter 2

Carbon Nanotubes: Structure and Properties

Carbon nanotubes (CNTs) are quasi-one dimensional crystals with the shape of hollow cylinders made of one or more graphite sheets; their size is typically μm in length and 1 to tens of nm in diameter. Because of many interesting properties that carbon nanotubes exhibit and their possible applications, CNTs have emerged to be one of the most intensively investigated nanostructure materials since their discovery. In this Chapter a brief historical review of carbon nanotube research is presented. Then a more detailed description of the geometrical structure and the physical properties of nanotubes are described. In particular the electronic and optical properties are focused in consideration of the main aim of this thesis, i.e. to verify and understand the mechanisms of measured photocurrent generation in multiwall carbon nanotubes both used in photoelectrochemical cells and in solid-state device.

2.1 Historical excursus

Carbon appears in several crystalline modifications, as a result of its flexible electron configuration. The carbon atom has six electrons; the 2s orbital and the 2p orbitals can form an sp^2 or sp^3 hybrid, respectively. The sp^3 configuration gives rise to the tetrahedrally bonded structure of diamond. The sp^2 orbitals lead to strong in-plane bonds of the hexagonal structure of graphite and the remaining p-like orbital to weak bonds between the planes. In 1985 Kroto et al discovered a modifications of crystalline carbon the so-called buckyballs [1]. This discovery was very important because not just a single new molecule was found but an infinite class of new molecules: the fullerenes. Each fullerene – C_{60}, C_{70}, C_{84}, etc. – possessed the essential characteristic of being a pure carbon cage, each atom bonded to three others as in graphite. Unlike graphite, every fullerene has exactly 12 pentagonal faces with a varying number of hexagonal faces. Some fullerenes, like C_{60}, were spheroidal in shape, and others, like C_{70}, were oblong like a rugby ball. The most famous one of the buckyballs is probably C_{60}, a spherical molecule formed by 20 hexagons. Dr. R. Smalley recognized in 1990 that, in principle, a single wall carbon nanotube, SWNT, might be a limiting case of a fullerene molecule: a tubular fullerene capped at each end, for example, by the two hemispheres of C_{60}, connected by a straight segment of tube, with only hexagonal units in its structure. M. Dresselhaus, upon hearing of this concept, dubbed these imagined objects “buckytubes.”

Actually carbon nanotubes had been discovered 30 years earlier, but had not been fully appreciated at that time. In the late 1950s, Roger Bacon at Union Carbide, found a strange new carbon fibre while studying carbon under conditions near its triple point. He observed straight, hollow tubes of carbon that appeared to consist in graphitic layers of carbon separated by the same spacing as the planar layers of graphite. In the 1970s and 1980s, Morinobu Endo observed these tubes again, produced through the synthesis of vapor grown carbon fibers by the decomposition of hydrocarbons at high temperatures in the presence of transition metal catalyst particles of < 10 nm diameter. Indeed, he even observed some tubes consisting in only a single layer of rolled-up graphite. [2-4].

But the discovery of nanotubes is ascribed to Sumio Iijima of the NEC Laboratory in Tsukuba (Japan) who observed multiwall nanotubes, MWNT, formed in a carbon arc discharge in 1991 [5]. Multiwall carbon nanotubes (see Fig.1) contain several

coaxial cylinders, each cylinder being a single-wall carbon nanotube, nested as Russian dolls.

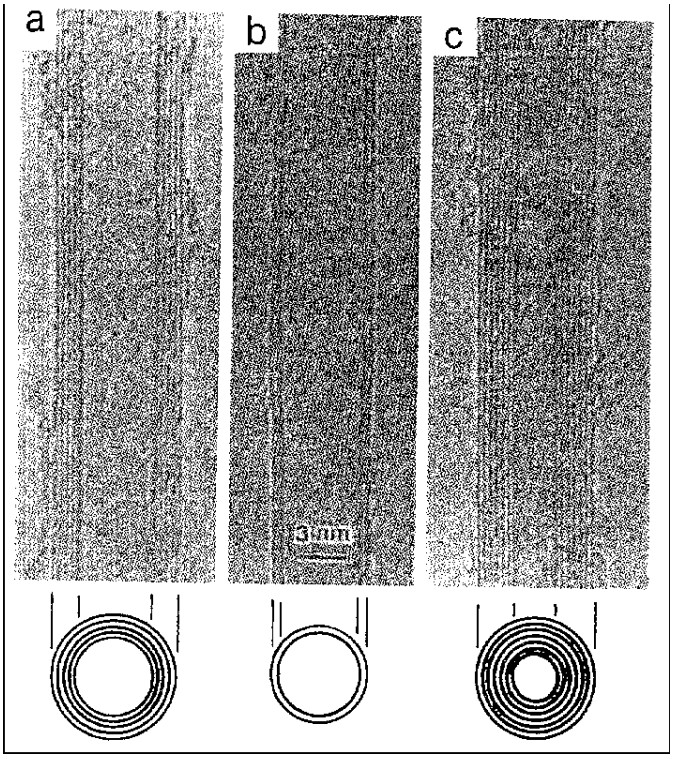

Fig. 1. The observation by TEM of multi-wall coaxial nanotubes with various inner and outer diameters, d_i and d_o, and numbers of cylindrical shells N reported by Iijima in 1991: (a) N = 5, d_o = 67 Å, (b) N = 2, d_o = 55 Å and (c) N = 7, d_i = 23 Å, d_o = 65 Å [5]

Two years later Sumio Iijima and Donald Bethune and coworkers at the IBM Almaden Laboratory independently observed SWNTs [6,7]. This has allowed a great number of theoretical studies and predictions that preceded the experimental observation of single wall carbon nanotubes. On the contrary, until now very few ab-initio calculations have been performed to predict the properties of MWNT due to the very large numer of carbon atom to take in account. The most fundamental of the theoretical developments on SWNTs was the prediction that carbon nanotubes could be either semiconducting or metallic depending on their diameter and orientation of their hexagons with respect to the nanotube axis (chiral angle) [8-10]. These predictions were experimentally confirmed in 1998 [11,12].

Moreover carbon nanotubes are intriguing from a fundamental physics point of view. In contrast to many quasi-one-dimensional systems in semiconductor physics, where carriers are artificially restricted to a one-dimensional phase space by sophisticated fabrication like cleaved-edge overgrowth [13,14] or experiments in the

quantum-Hall regime [15], carbon nanotubes are natural quasi-one-dimensional systems with ideal periodic boundary conditions along the circumference. Their one-dimensional character has been manifested in many experiments like scanning-tunneling spectroscopy, where the singularities in the density of states typical for one dimension have been measured [12, 16-17]. Then, for example, they appear an ideal system for the study of Luttinger liquid behaviour [18,19]; ballistic transport at room temperature up to several μm was reported [20] and, if defects or electrical contacts act as boundaries, zero-dimensional effects such as Coulomb blockade are observed [21,22].

Of course it has been taken into account that actual CNTs have finite length, contain defects, and interact with other nanotubes or with the substrate and these factors often complicate their behaviour in respect to the theoretical predictions.

The remarkable physical properties exhibited by carbon nanotubes paved the way to many possible applications of carbon nanotubes both on the nanometer scale and in the macroscopic range that attracted great attention and expectations. In nanoelectronics, it has been demonstrated that is possible to connect nanotubes with different chiralities creating nanotube heterojunctions to be used as nanoelectronics devices [23,24] such as nanoscale p-n junctions [25], field effect transistor [26-28] and single-electron transistor [29,30]. Recently CNTs have been used for many and different applications of great technological importance: conductive wires [31-33], new optoelectronic devices [34], photosensitive transistors [35], innovative solar cells [36,37], or chemical sensors [38,39]. Prototype devices using the superior field emission properties of nanotubes [40] have been also demonstrated. These devices include x-ray tubes [41], scanning x-ray sources [42], flat panel displays [43], and lamps [44].

Single and multi-wall nanotubes have also very good elasto-mechanical properties because the two dimensional arrangement of carbon atoms in a graphene sheet allows large out-of-plane distortions, while the strength of carbon-carbon in-plane bonds keeps the graphene sheet exceptionally strong against any in-plane distortion or fracture. These structural and materials characteristics of nanotubes point towards their possible use in making next generation of extremely lightweight but highly elastic and very strong composite materials (torsional springs [45,46] or as single vibrating strings for ultrasmall force sensing).

A major difficulty for the applications is the variety of nanotube structures that are produced simultaneously; in particular a growth method which determines whether the tubes will be metallic or semiconducting is still not available. Instead, the production methods yield tube ensembles where presumably all nanotube structures are equally distributed, and the tubes are typically found in bundles. Applications like nanotube field emitters or reinforcing materials by adding carbon nanotubes, do not require specific isolated tubes and are thus easier to realize.

2.2 The geometrical structure

A tube made of a single graphite layer, named graphene, rolled up into a hollow cylinder is called a single-walled nanotube; a tube comprising several, concentrically arranged, cylinders is referred to as a multi-walled tube. SWNTs have typical diameters of 1 - 2 nm while MWNTs have a typical diameter of 10 - 40 nm with an interlayer spacing of 3.4Å. The lengths of the two types of tubes can be up to hundreds of microns or even centimeters. There are many possible CNT geometries, depending on how graphene (Fig.2) is rolled into a cylinder. Geometric variables, such as the alignment between the cylinder axis and the graphene crystal axes, strongly influence the electrical properties of a CNT [47].

Because the microscopic structure of a CNT is derived from that of graphene, the tubes are usually labeled in terms of the graphene lattice vectors. Fig.2 shows the graphene honeycomb lattice. The unit cell is spanned by the two vectors $\mathbf{a_1}$ and $\mathbf{a_2}$, forming an angle of 60º, of length

1 $$|\mathbf{a_1}|=|\mathbf{a_2}|=a_0=2.461\text{Å} \qquad a_0=\sqrt{3}a_{c-c}$$

where a_0 is the lattice parameter and a_{c-c} is the length of the covalent bond between carbon atoms. In carbon nanotubes, the graphene sheet is rolled up in such a way that a graphene lattice vector

2 $$\mathbf{C} = n_1\mathbf{a_1} + n_2\mathbf{a_2}$$

becomes the circumference of the tube by joining the parallel lines which are defined by the starting (O) and ending (A) point of the vector. This circumferential vector **C**, which is usually denoted by the pair of integers (n_1, n_2), is called the chiral vector (**C**) and uniquely defines a particular tube.

In terms of the integers (n_1, n_2) the tubule diameter d is given by

1 $$d = \frac{|C|}{\pi} = \frac{a_0}{\pi}\sqrt{n_1^2 + n_1 n_2 + n_2^2} = \frac{a_0}{\pi}\sqrt{N}$$

with $N = n_1^2 + n_1 n_2 + n_2^2$. The direction of the chiral vector **C** is measured by the chiral angle θ, which is defined as the angle between $\mathbf{a_1}$ and **C**.

The chiral angle θ can be calculated from:

2 $$\cos(\theta) = \frac{\mathbf{a_1} \cdot \mathbf{C}}{|\mathbf{a_1}| \cdot |\mathbf{C}|} = \frac{n_1 + n_2/2}{\sqrt{n_1^2 + n_1 n_2 + n_2^2}}$$

For each tube with θ between 0º and 30º an equivalent tube with θ between 30º and 60º exists, but the helix of graphene lattice points around the tube changes from right-handed to left-handed.

There are three distinct geometries of SWNTs (Fig.2 a-c):

1. The nanotubes of type (n, n) are commonly called armchair nanotubes. because of the _/‾_/ shape, perpendicular to the tube axis. Chiral angle 30º.

2. The nanotubes of type (n_1, 0) is known as zigzag nanotubes because of the /\/\/ shape perpendicular to the axis. Chiral angle 0º.

3. All the remaining nanotubes are known as chiral or helical nanotubes.

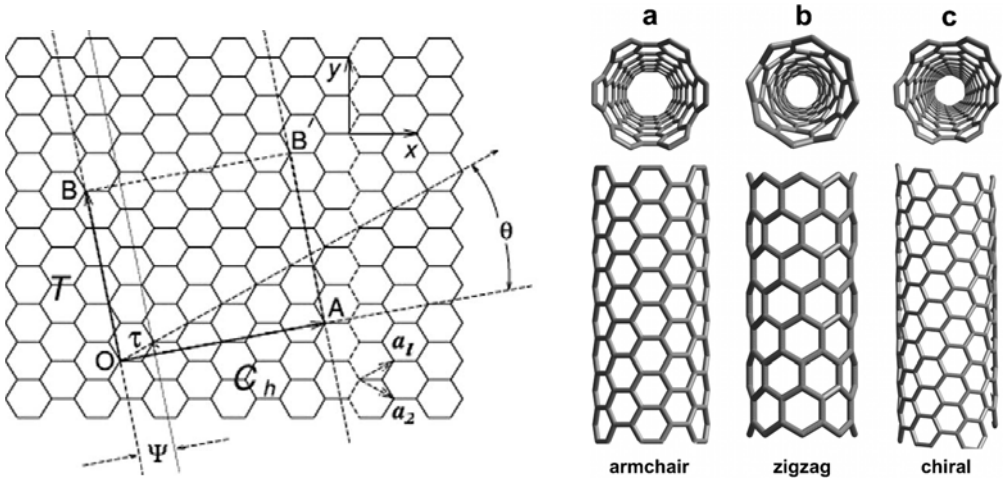

Fig. 2. On the left, a graphene sheet can be wrapped onto itself to form a nanotube. vector C in an infinite graphene sheet describes how to "roll up" the graphene sheet to make the nanotube. T denotes the tube axis, and a_1 and a_2 are the unit vectors of graphene in real space. On the right, classification of nanotubesis: (a) armchair, (b) zig-zag and (c) chiral.

The geometry of the graphene lattice and the chiral vector of the tube determine its structural parameters like diameter, unit cell, and its number of carbon atoms, as well as size and shape of the Brillouin zone.

The smallest graphene lattice vector **a** perpendicular to **C** defines the translational period **a** along the tube axis [17]. In general, the translational period **a** is determined from the chiral indices (n_1, n_2) by:

3 $$\mathbf{a} = -\frac{2n_2 + n_1}{n_R}\mathbf{a_1} + \frac{2n_1 + n_2}{n_R}\mathbf{a_2}$$

and

4 $$a = |\mathbf{a}| = \frac{\sqrt{3(n_1^2 + n_1 n_2 + n_2^2)}}{n_R} a_0 = \frac{\sqrt{3}C}{n_R}$$

where the length of **C** is given by Eq. 3 and n_R is the highest common divisor of (n_1, n_2):

Thus, the nanotube unit cell is formed by a cylindrical surface with height *a* and diameter *d*.

Tubes with the same chiral angle θ, i.e., with the same ratio n_1/n2, possess the same lattice vector **a**. In Fig.3 the structures of (17,0), (10,10), and (12,8) tubes are shown, where the unit cell is highlighted and the translational period a is indicated. Note that a varies strongly with the chirality of the tube; chiral tubes often have very long unit cells.

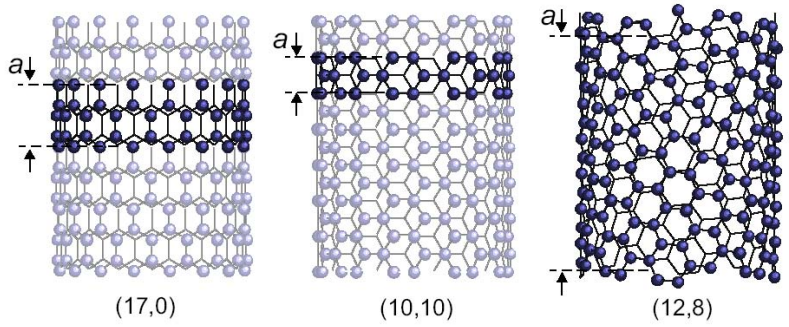

Fig. 3. Structure of the (17,0), the (10,10) and the (12,8). The unit cells of the tubes are highlighted; the translational period a is indicated.

Experimentally, the atomic structure of carbon nanotubes can be investigated either by direct imaging techniques, such as transmission electron microscopy [48]

and scanning probe microscopy [49], or by electron diffraction [50,51], i.e., imaging in reciprocal space.

Scannig tunneling microscopy (STM) offers measurements with atomic resolution, see Fig.4. From both, STM and electron diffraction, the chiral angle and tube diameter can be determined, and hence the chiral in principle, can be found experimentally.

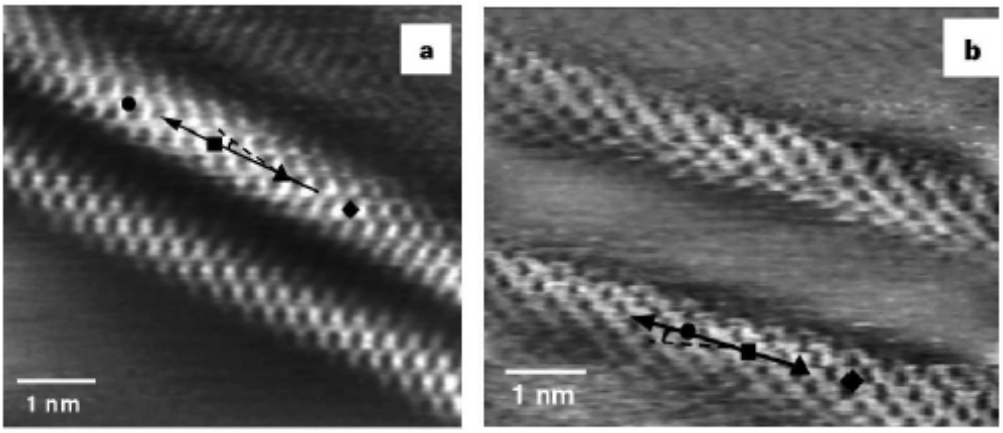

Fig 4. Scanning tunneling microscopy images of an isolated semiconducting (a) and metallic (b) singlewalled carbon nanotube on a gold substrate. The solid arrows are in the direction of the tube axis; the dashed line indicates the zig-zag direction. Based on the diameter and chiral angle determined from the STM image, the tube in (a) was assigned to a (14,3) tube and in (b) to a (12,3) tube. The semiconducting and metallic behavior of the tubes, respectively, was confirmed by tunneling spectroscopy at specific sites. From Ref. [29].

2.3 Physical properties of CNTs

The attention in this paragraph is focused on the electronic and optical properties of SWNT and MWNT.

2.3.1 Electronic properties

2.3.1.1 Correlation between structure and electronic properties: the bidimensional graphene

To study the electronic properties of nanotubes let's begin from the analysis of the graphene properties. The reference of the analysis is pictured in Fig.5 where the direct lattice vectors $\mathbf{a_i}$ and the corresponding reciprocal lattice vectors $\mathbf{k_i}$ are defined.

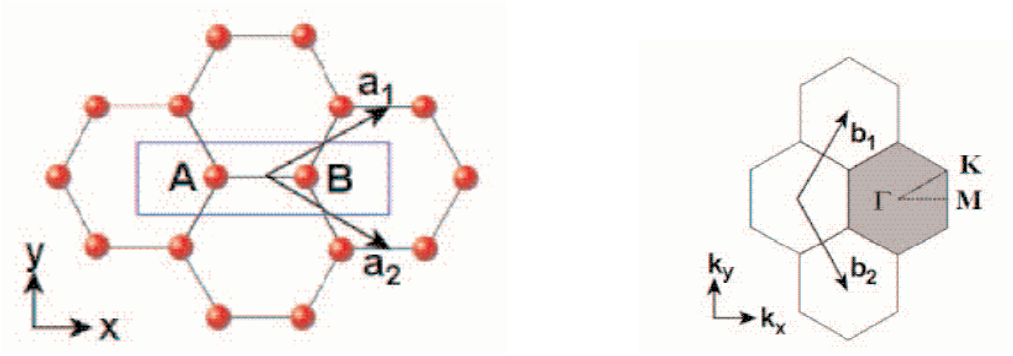

Fig. 5. The unit vectors of graphene of the direct lattice (a_i on the left) and of the reciprocal lattice (k_i on the right).

$$\mathbf{a_1} = \left(\frac{\sqrt{3}}{2}a_0, \frac{a_0}{2}\right), \mathbf{a_2} = \left(\frac{\sqrt{3}}{2}a_0, -\frac{a_0}{2}\right) \qquad \mathbf{b_1} = \left(\frac{2\pi}{a_0\sqrt{3}}, \frac{2\pi}{a_0}\right), \mathbf{b_2} = \left(\frac{2\pi}{a_0\sqrt{3}}, \frac{-2\pi}{a_0}\right)$$

We observe that the fundamental cell of the reciprocal lattice is the first Brillouin zone for the graphite layer due to the fact that we have chosen the Wigner-Seitz hexagonal cell as cell for the direct lattice.

To determine the Brillouin zone associated to the unit bidimensional cell of nanotube, defined from **C** and **T** (see Fig.2) the corresponding vectors of the reciprocal lattice are defined $\mathbf{G_C}$ and $\mathbf{G_T}$**:**

7
$$\boldsymbol{G_C} \parallel \boldsymbol{C} \qquad \boldsymbol{G_C} = \frac{2\pi}{\boldsymbol{C}}$$
$$\boldsymbol{G_T} \parallel \boldsymbol{T} \qquad \boldsymbol{G_T} = \frac{2\pi}{\boldsymbol{T}}$$

In a nanotube the electron is constraint to move under a periodic potential of period equal to $|\mathbf{C}|$ so a discretization of energetic level along the circumference **C** corresponding to a discrete ensemble of wave vectors along the reciprocal lattice vector $\mathbf{G_C}$. This gives rise to lines of quantization corresponding to the allowed value for the couple (k_X, k_y). Due to the stationary condition related to the electron wave, it is

8
$$\mathbf{k} \cdot \mathbf{C} = 2\pi q$$

where q is an integer and **k** the electron wave vector.

So the electrons are free to move along the length, while in the reciprocal lattice space quantization lines are observed and they are spaced of

9 $$\Delta k = 2\pi / |\mathbf{C}| = 2/d$$

where *d* is the diameter of the tube.

Each line will correspond to a unidimensional channel of conduction along the same nanotube. In Fig.6 allowed wave vectors are showed for different nanotube type: armchair, zig-zag, and chiral.

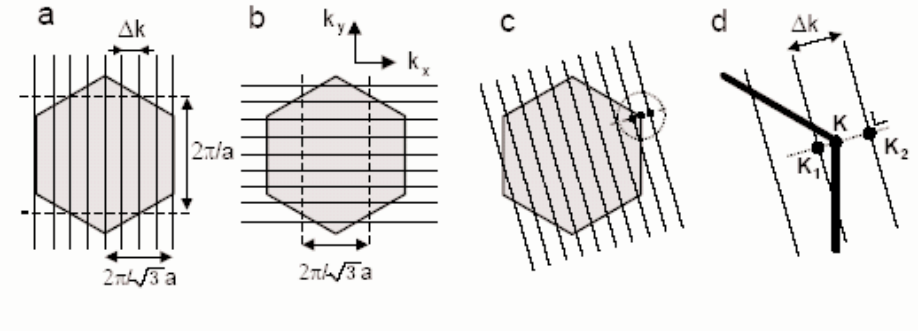

Fig. 6. Allowed wave vectors on the base of the constraint condition for: (a) armchair, (b) zig-zag, and (c) chiral nanotube.

2.3.1.2 Correlation between structure and electronic properties: the dispersion equation

The band structure of the 'rolled-up' SWNTs can be studied starting from the band structure of a single graphene sheet. The two-dimensional (2D) dispersion relation is obtained by using the tight binding approximation [52].

10 $$E_{g2D}^{\pm}(k) = \pm\gamma_0 \left\{ 1 + 4\cos\left(\frac{\sqrt{3}}{2}k_y a_0\right)\cos\left(\frac{\sqrt{3}}{2}k_x a_0\right) + 4\cos^2\left(\frac{k_x a_0}{2}\right) \right\}^{1/2}$$

where γ_0 is the nearest-neighbor C-C overlap integral and a_0 is given in Eq. 1.

Although for the nanotube geometry there is some mixing of the $\pi(2p_z)$ and $\sigma(2s$ and $2p_{x,y})$ carbon orbitals due to the fiber curvature, it is small and can be neglected near the Fermi level. In this way is it correct to take the Eq. 10 of graphene for nanotubes dispersion relation considering only π orbitals [53]. The dispersion relation described by Eq. 10 is plotted in Fig.7 to show the high energy ($E_k > E_0$) and low energy ($E_k < E_0$) states that make up the conduction and valence bands of graphene.

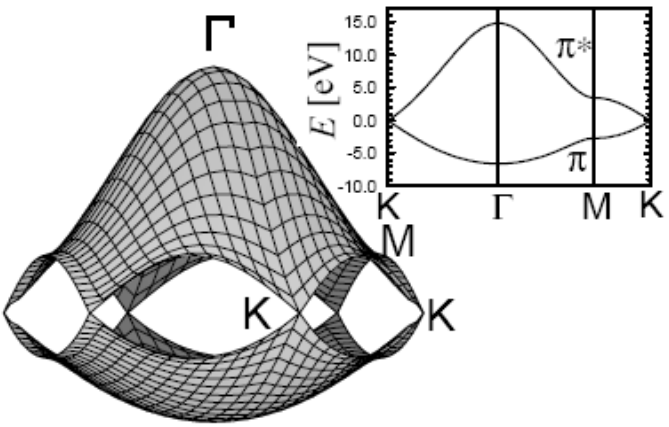

Fig. 7. Energy dispersion relations for 2D graphite throughout the whole region of the Brillouin zone (γ_0 = 3.013 eV ,in Eq. (10)). The inset shows the energy dispersion along the high symmetry lines between the Γ, M, and K points. The valence π band (lower part) and the conduction π* band (upper part) are degenerate at the K points in the hexagonal Brillouin zone which corresponds to the Fermi energy [54]

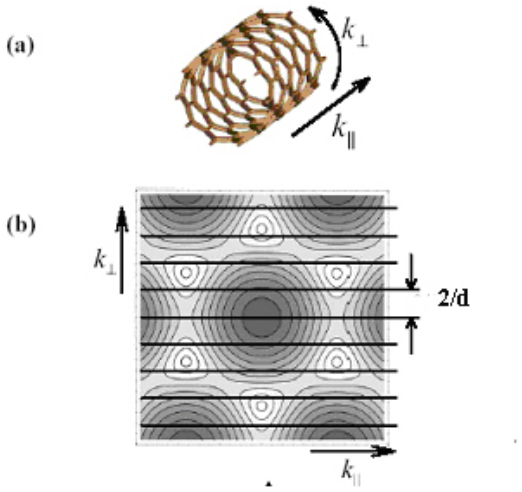

Fig. 8. Quantization of wave states around a graphene cylinder. a) The parallel and perpendicular axes of a CNT. b) Contour plot of graphene valence states for a CNT with the chiral angle θ = 0˚. The parallel lines spaced 2/d indicate the k vectors that are allowed by the cylindrical boundary condition. Each line is a 1-D subband. Lower energies are darker. The circular contours around six K points are coloured white. The hexagonal formed by the six K points defines the graphene unit cell in k-space.

Eliminating k_x or k_y by using the periodic condition boundary of Eq. 8, we get 1D energy bands can be obtained by *slicing* the 2D energy dispersion relations of Eq. 10 in the directions expressed by Eq. 8. In the direction parallel to the CNT axis, however, electrons are free to move over much larger distances and the electron wavenumber in the parallel direction, $k_{||}$, is effectively continuous. The parallel lines in Fig.8 represent the allowed k states in a CNT. The continuum of k|| states in each k wrapping mode are called one-dimensional (1-D) subbands. These subbands are

called Van-Hove singularities (vHSs) and are shown in Fig.9 for a (9,0) and (10,0) SWNTs [53]

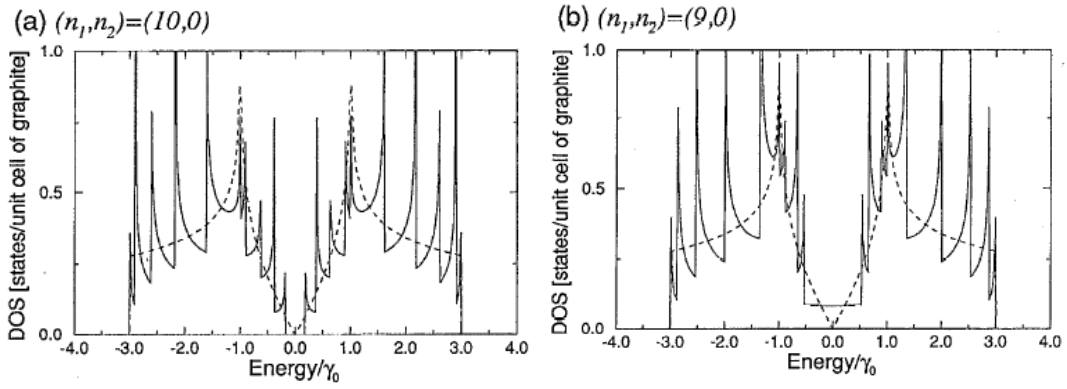

Fig. 9. Electronic density of states for two (10,0) (a) and (b) zigzag nanotubes. Dotted lines correspond to the density of states of a 2D graphene sheet. The density of states near the Fermi level located at E = 0 is zero for the semiconducting (10, 0) nanotube and is non-zero for the metallic (9, 0) nanotube. From ref. [53]

This approach is called **zone folding** and is commonly used in nanotube and nanostructure research (Fig.10). The zone folding procedure neglects any effect of the cylinder geometry and curvature of the tube walls. The zone folding approach to calculate the electronic band structure of CNT falls down for small nanotube diameter (d < 1nm) because in small diameter CNTs the mixing and the rehybridization of the p and s orbital in the curved graphite sheet can significantly change the electronic band structure [55]. For example, the (5,0) tube is metallic in contrast to what is expected from zone folding [56].

The exact alignment between allowed k values and the K points of graphene is critical in determining the electrical properties of a CNT. If, for a particular (n, m) nanotube, the cutting line passes through a K point of the 2D Brillouin zone (Fig.6 a), where the π and π^* energy bands of two-dimensional graphite are degenerate (Fig.7) by symmetry, then the one-dimensional energy bands have a zero energy gap. Since the degenerate point corresponds to the Fermi energy, and the density of states are finite as shown below, SWNTs with a zero band gap are metallic. When the K point is located between two cutting lines, the K point is always located in a position one-third of the distance between two adjacent K1 lines (Fig.6 c-d) [57] and thus a semiconducting nanotube with a finite energy gap appears. Therefore the tube is metallic, if the allowed states of nanotubes contains the graphite K points, otherwise is semiconducting. The rule for being either a metallic or a semiconducting carbon

nanotube is, respectively, that $n_1 - n_2 = 3q$ or $n_1 - n_2 \neq 3q$, where q is an integer. For example, in all armchair tubes the band with $n_1 = n_2$ includes the K points (Fig.6 d), they are always metallic. More deeply because of the degeneracy point between the conduction and valence bands, all the armchair tubes will exhibit metallic conduction at finite temperature, because only infinitesimal excitations are needed to excite carriers into the conduction band. The armchair tubes are thus a zero-gap semiconductor, just like a 2D graphene sheet.

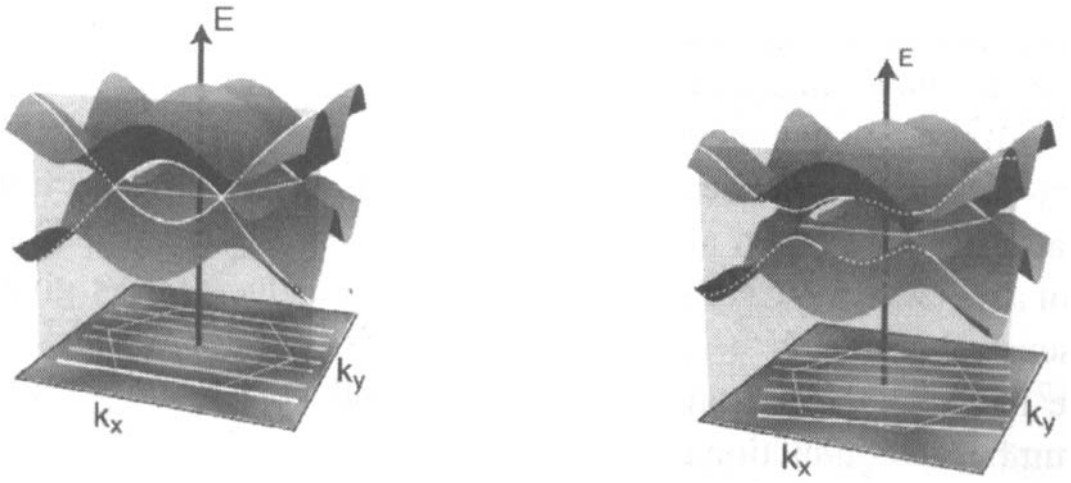

Fig. 10. Schematization of the zone folding approach to illustrate the electronic band structure of SWNT (3,3) left and (4,2). The two dimensional band structure of graphene has cutted with j lines of length $2\pi/a$ (first Brillouin zone) and distance $2/d$ parallel to the direction of the tube axis.

Thus, we can have both semiconducting (Fig.9a) and metallic (Fig.9 b) nanotubes by merely changing the nanotubes diameter. The energy gap for the semiconducting fibers decreases with increasing fiber diameter d and in the limit of $d \rightarrow \infty$, we obtain the 2D case of a zero-gap semiconductor.[1] Density of states measurements by scanning tunnelling spectroscopy (STS) confirm that some nanotubes (about 1/3) are conducting, yet most (about 2/3) are semiconducting [55,58]. Measurements confirm that the band gap is proportional to 1/d.

[1] Summarizing, the electronic properties of a nanbotube changes in correspondence with the axis of symmetry along which it is rolled, armchair are metallic while zigzag and chiral can be either metallic or a semiconductor.

2.3.2 Optical properties

The phonon dispersion relation of a 2D graphene is similar to that of a has a 3D graphite, due to the week interplanar coupling in graphite [59]. Graphite has 6 normal phonon modes and the irreducible representation is given by [60]:

$$\Gamma = 2E_{2g} + E_u + A_{2u} + 2B_{2g} \tag{11}$$

The phonon dispersion of a SWNT can be calculated by folding the phonon dispersion curves of a two-dimensional graphene layer analogous as for the case of the 2D electronic states[54].

For the nanotube there are now four acoustic modes: an LA mode, corresponding to motion of the atoms along the tube axis, two degenerate TA modes, corresponding to atomic displacements perpendicular to the nanotube axis, and a 'twist' mode, corresponding to a torsion of the tube around its axis. The LA mode is exactly analogous to the LA mode in graphene. The TA modes in a SWNT, on the other hand, are a combination of the in-plane and out-of-plane TA modes in graphene, while the twist mode is directly analogous to the in plane TA mode. These modes all show linear dispersion (there is no nanotube analogue to the ZA mode) and high phonon velocities: v_{LA} = 24 km/s, v_{TA} = 9 km/s, and v_{twist} = 15 km/s for a (10,10) tube (Fig.11) [54]. The inset of Fig.11 shows the low-energy phonon density of states of a (10,10) nanotube (solid line), with DOS of graphene (dot-dashed line) and graphite (dashed line) shown for comparison. In contrast to 2-D graphene and 3-D graphite, which show a smoothly-varying DOS, the 1-D nanotube has a step-like DOS, which has 1-D singularities at the subband edges. The markedly different phonon density of states in carbon nanotubes results in measurably different thermal properties at low temperature.

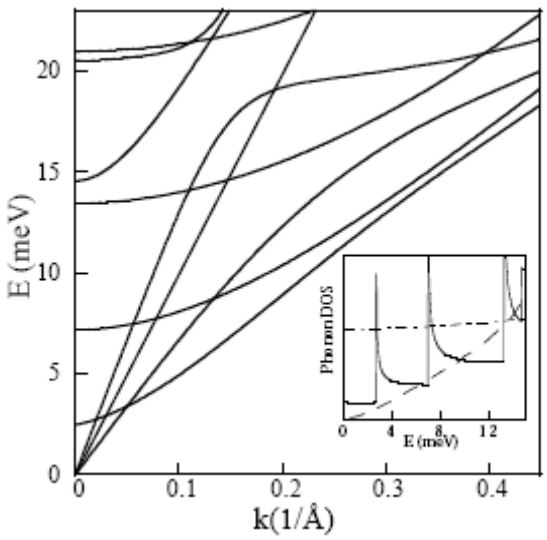

Fig. 11. Low-energy phonon dispersion relations for a (10,10) nanotube. There are four acoustic modes: two degenerate TA modes (v = 9 km/s), a 'twist' mode (v = 15 km/s), and one TA mode (v = 24 km/s) [54]. The inset shows the lowenergy phonon density of states of the nanotube (solid line) and that of graphite (dashed line) and grapheme (dot-dashed line). The nanotube phonon DOS is constant below 2.5 meV, then increases stepwise as higher subbands enter; there is a 1-D singularity at each subband edge.

Information on the properties of the phonons can be obtained from Raman spectroscopy. The *Raman scattering* is a process in which a light quantum hits a molecule and is inelastically scattered. Whether a vibration is Raman active or not is determined by the symmetry of the crystal described in group theory. When the frequency of the incident radiation approaches an electronic transition frequency the intensity of the Raman bands is strongly enhanced. Raman spectra obtained with exciting frequencies close to absorption bands are called resonance Raman spectra. For this reason, from resonant Raman it is possible to obtain information both on optical and electronic properties.

2.3.3 Relevant Experimental Results

One-dimensional van Hove singularities (vHs) in the DOS, which are known to be proportional to $\left(E^2 - E_0^2\right)^{-1/2}$ at both the energy minima and maxima ($\pm E_0$) of the dispersion relations for carbon nanotubes, are important for determining many solid state properties of carbon nanotubes.

The experimental evidence of these singularities come out from different types of experiments such as scanning tunneling spectroscopy (STS) [11-12,61-62], optical absorption [62,65], and resonant Raman spectroscopy [66,67].

Scanning tunneling microscopy and spectroscopy (STS) offer the potential to probe the theoretical predictions about the electronic properties of carbon nanotubes since these techniques are capable of resolving simultaneously the atomic structure and electronic density of states of a material. Atomically resolved image of isolated SWNTs on a Au (111) substrate is shown in Figs. 12a. Analysis of the image shows that the upper tube has a chiral angle of $11.2 \pm 0.5°$ and a diameter of 0.95 ± 0.05 nm. The I–V data recorded with this atomic-resolution image (Fig.12b) is consistent with a semiconductor tube. In Fig.12c the energy gaps (E_g) obtained from these measurements for tubes with diameters, d, between 0.6 and 1.1nm are shown. It is evident the $1/d$ diameter dependence, and can be fitted to $E_g = 2\gamma_0 a_{C-C}/d$, where $\gamma_0 = 2.45\,\text{eV}$.

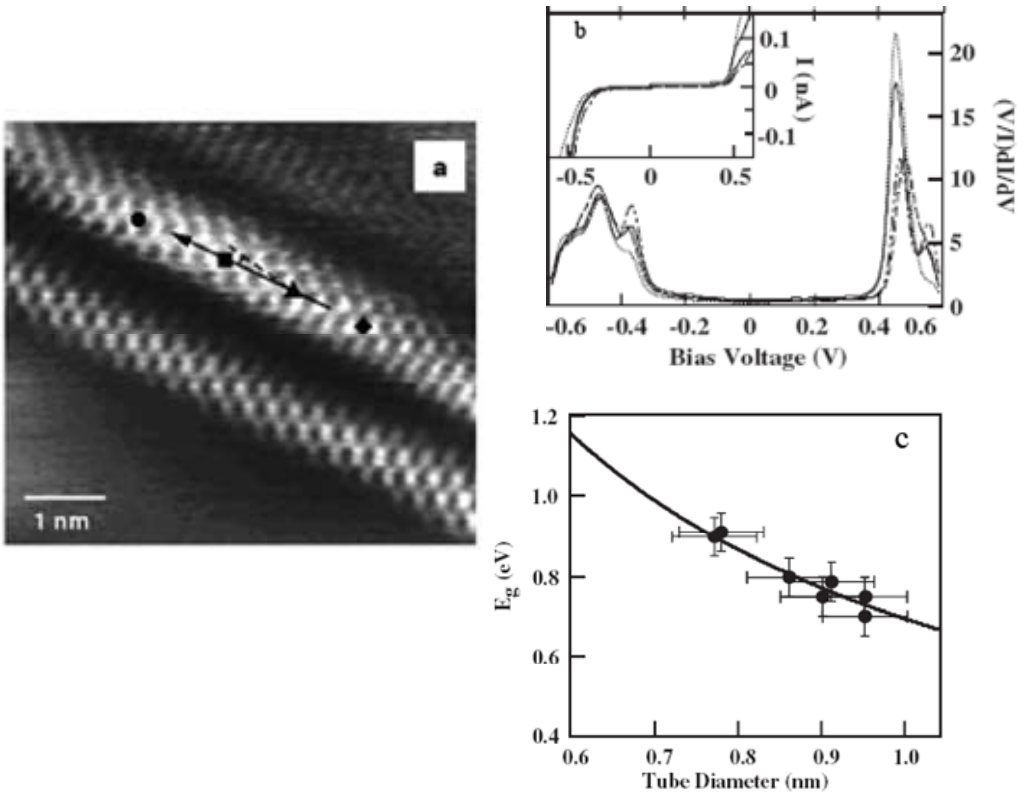

Fig. 12. Structure and spectroscopy of semiconducting SWNTs. (a) Constant current image of isolated SWNTs on a Au(111) surface recorded with a bias voltage of 300mV and a tunnelling current of 150 pA. The solid, black arrow highlights the tube axis, and the dashed line indicates the zigzag direction. (b) Calculated normalized conductance and measured I–V (inset) data from the positions indicated by the symbols in (a). (c) Summary of energy gap (Eg) versus tube diameter data obtained in these studies [12].

The optical experiments are good probes due to the fact that according to the Fermi's Golden Rule, any optical transition that are resonant with these Van Hove singularities are expected to be greatly enhanced. The optical response of the SWCNT is dominated by transitions $E_{ii'}$ from the i-th valence band to the i'-th conduction band of the density of states (DOS), with momentum conservation only allowing transitions pairs of singularities which are symmetrically placed with respect to the Fermi level.

The efficiency of ultraviolet-visible-infrared (UV-VIS-IR) optical absorption spectroscopy for SWNT diagnostics has been demonstrated in the first time by Kataura et al. [65]. The absorption spectra show features corresponding to E_{11}, E_{22}, E_{33},… optical transitions. Later Smalley and coworkers [68] showed optical spectroscopy can be used to determine detailed composition of bulk SWNT samples, providing distribution in both tube diameter and chiral angle. In fact, the energetic separation of the pairs of van Hove singularities is inversely proportional to the tube diameter, thus the optical transitions in SWCNT are also inversely proportional to the nanotube diameter. He assigned each optical transition to a specific (n,m) nanotube structure, combining spectrofluorimetric measurements with resonance Raman spectra.

A very interesting point is that experimentally, it has been demonstrated that electron energy-loss spectroscopy (EELS) in transmission and optical absorption spectroscopy are comparably powerful tools in the study of the mean electronic properties of bulk samples of SWCNTs. EELS in transmission measured using low momentum transfers probes the optical limit, is a direct probe of the collective excitations caused by the optically allowed transitions [69,62]. Analogous results for the low energy interband transitions were obtained from optical absorption spectroscopy [65,70], From both the EELS analysis and the optical absorption data, several distinct spectral features are observed for energies below 3 eV [71]. These features have been related to interband transitions between the van Hove singularities in the electronic DOS of the semiconducting and metallic SWCNT's (Fig.9). Typical EELS and optical results for SWCNT with 1.3 nm mean diameter are depicted in Fig.13.

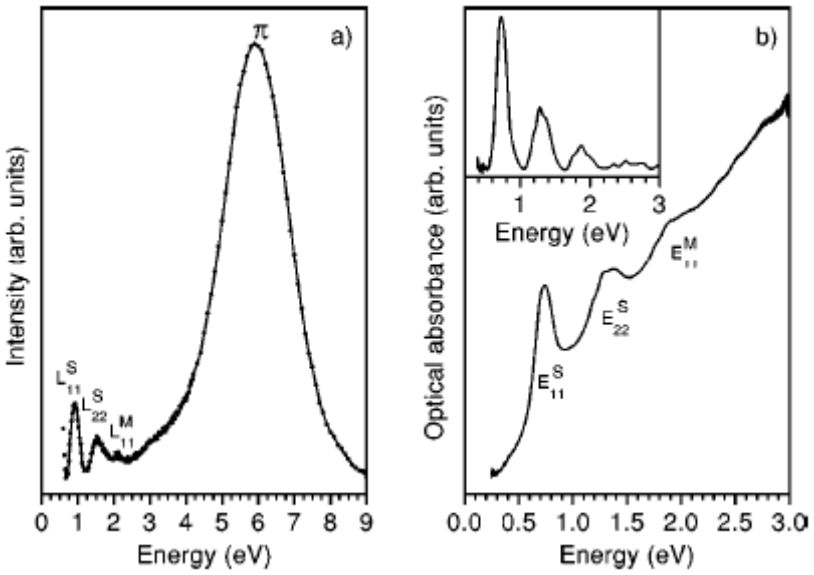

Fig. 13. (a) Loss function of SWCNT's with 1.3 nm mean diameter (sample D) recorded at q = 0.1 Å between 0 and 9 eV. L_{11}^{S}, L_{22}^{S}, and L_{11}^{M} are interband transition in loss function from EELS measurement. (b) Optical absorption spectra of the same SWCNT between 0 and 3 eV. The inset shows the absorbance in the range of E_{11}^{S}, E_{22}^{S}, and E_{11}^{M} interband transitions after subtraction of the contributions from the high energy interband transitions.

The left panel shows the loss function at a momentum transfer q = 0.1 Å between 0 and 9 eV which covers the excitations related solely to the SWCNT π electron system. The strong peak at around 6 eV is the so-called π plasmon, which is the collective excitation of the SWCNT p electrons. The first three loss peaks below 3.0 eV ~ i.e., L_{11}^{S} , L_{22}^{S}, and L_{11}^{M}) are ascribed to interband transition from EELS measurement. In the right panel a typical optical absorption spectrum of the same nanotubes is depicted. The inset shows the absorbance after subtracting the contributions from the high energy interband transitions.

Note that due to the fact that EELS technique probes collective excitations (proportional to Im(1/ε), where ε is the dielectric constant), the peak positions are slightly upshifted as compared to optical absorption which is proportional to the imaginary part of e , i.e., the peak position of L_{11}^{S} is always higher than that of E_{11}^{S}. In principle, one could use a Kramers-Kronig analysis to derive the absorption data from the loss function data [71].

2.4 What about MWNT properties

Multiwall nanotubes (MWNTs) consist of multiple layers of graphite rolled in on themselves to form a tube shape. In the Russian Doll model, sheets of graphite are arranged in concentric cylinders, eg a (0,8) SWNT within a larger (0,10) SWNT (Fig.14). The number of nanotubes in a multiwall carbon nanotube can vary from N = 2 to ~ 100 [73-76] The smallest inner radius is r ~ 5 Å and the largest outer radius is r ~ 300Å.

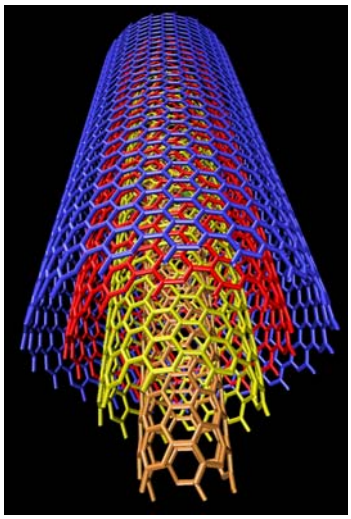

Fig. 14. Picture of a Russian Doll MWCNT.

Because multi-wall nanotubes (MWNTs) consist of several coaxially arranged SWNTs, one may expect that MWNTs do not qualify as 1-D conductors. Assuming that neighboring shells do not interact, the electronic properties of MWNTs would be similar to a set of independent SWNTs with radii in the range of a few nanometers to ~ 10 nm. Though the coupling strength between adjacent shells might be low, it possibly cannot be neglected altogether. For this reason, a much richer band structure might be expected. Graphite is, in fact, an excellent example for demonstrating the importance of the weak inter-plane coupling for ground-state properties. Graphite is a semimetal, and the finite density-of-states (DOS) at the Fermi energy can be traced back to the three-dimensional crystal structure with finite interplanar coupling which leads to a small band overlap of 40meV. MWNTs are mesoscopic, in-between the single-wall nanotube molecules and planar graphite. The question is if the electronic properties of MWNTs are closer to graphite or MWNTs rather behave as a set of independent SWNTs.

Since MWNTs consist of tubes with larger diameters (d_t), we need to understand how the van Hove singularities develop if the tube diameter d_t approaches values comparable to the mean-free path of electron l_e. The picture sketched above is valid if $l_e << d_t$ (1-D-ballistic transport). In contrast, if $l_e >> d_t$ transport is 2- D-diffusive and the density-of-states should closely resemble that for graphene without any singularities. If, on the other hand, le is of the same order as d_t, transport is neither fully 2-D-diffusive, nor 1-D-ballistic. In this regime, the characteristic subband features in the DOS are still present, also if considerably broadened. Important for MWNTs is the question of how the band structure might change due to inter-tube coupling. This question has previously been addressed [77,78]

Until now, no calculations of electronic DOS or phonon dispersion for MWCNT are reported due to their complex structure. Coupling between the layers of a MWNT should cause roughly graphite-like behavior. However, due to the lack of strict registry between the layers in a MWNT, the interlayer coupling could conceivably be much weaker than in graphite. So it is allowed to speculate on the existence of singularities in the density of states and in the phonon dispersion also for MWNT.

Really there are few theoretical predictions of their electronic properties and experiments that sustains this hypothesis.

Among experiments also, as like for SWNT, tunneling spectroscopy allowed to obtain information on the MWNT density of electronic states. In Fig.15 a differential current-voltage characteristic (dI/dV) measured on a single MWNT of diameter d_t = 17 nm is reported.

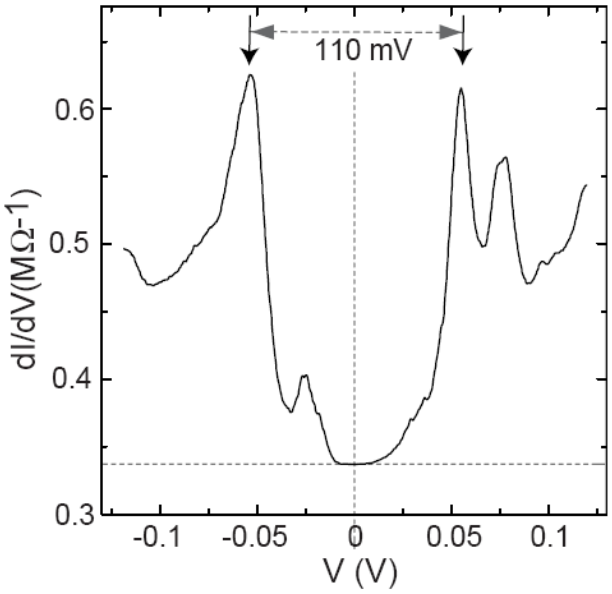

Fig. 15. Differential (tunneling) conductance dI/dV measured on a single MWNT using a high-ohmic contact (300 kΩ) at T = 4.2K [79]. This spectrum qualitatively confirms the DOS expected for a metallic nanotube in which the wave vector is quantized around the tube circumference leading to 1D-subbands. Positive (negative) voltages correspond to empty (occupied) nanotube states.

The measured spectrum identifies the metallic character of the multiwall nanotube. In fact there is a substantial DOS at the Fermi energy, i.e., at V = 0, so that the NT is metallic. Most important the almost symmetric peak structure, appearng as a pseudo-gap, is caused by the additional 1D-subbands in the valence band ($V < 0$) and conduction band ($V > 0$) with threshold energies of order ~ 50meV. The observed spectrum in Fig.15 demonstrates that the unusual band structure effects of NTs are also found for MWNTs. The observed peaks are associated with broadened van Hove singularities due to the 1-D-band structure. In most cases, however, the measured spectral features are not as sharp.

In regard to the loss spectra of MWNT, Shyu and cooworkers [80] have compared calculated results with experimental measurements of loss spectra for multiwall carbon nanotubes, single-wall carbon nanotube bundles, and graphite layers. The loss functions of the MWCNTs exhibit the most prominent π-plasmon peak as well as several interband plasmon peaks constituting a shoulder in the spectra at increasing number of walls (Fig 16). The latter do not exist in graphite layers, mainly owing to the absence of 1D sub-bands.

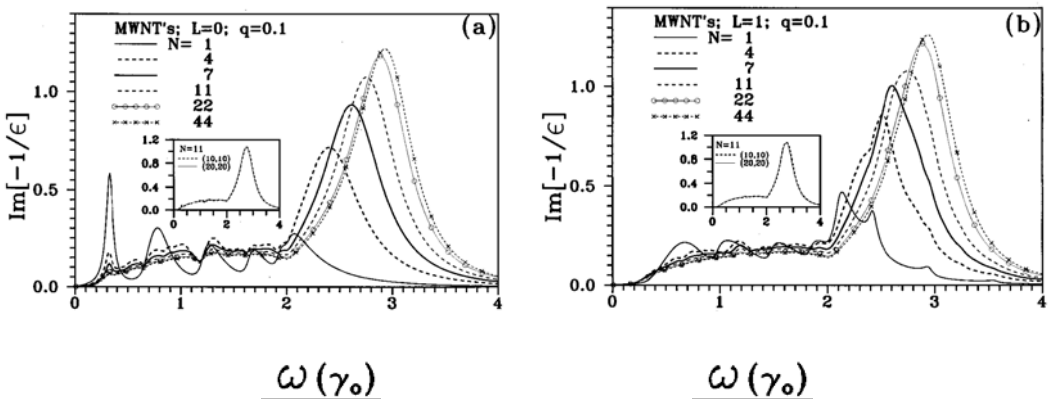

Fig. 16. (a) The loss spectra are shown for multiwall carbon nanotubes with different number of walls, N, at L=0 and q=0.1 (L is the transferred angular momentum and q, in Å^{-1}, is the transferred momentum). The (10,10) nanotube is the innermost nanotube of the multiwall nanotubes. The frequency is in units of the overlap integral γ_0 , which for these calculations had taken equal to 2.5 eV. (b) Same plot as (a), but shown at L=1. The (20,20) nanotube is also chosen as the innermost nanotube. The calculated results are shown in the insets for comparison.

This large dissemination, about theoretical predictions and experimental tools useful to investigate the nature of carbon nanotube, has been carried on with a clear purpose: focusing the role and influence of DOS singularities on the optoelectronic transitions. Consequently, it has been fundamental to show that also MWNTs could have singularities in their DOS as well as to determine proper experimental tools to study their physical properties. This has represented the starting point to perform photocurrent measurements, understand the results and correlate them to the inner mechanisms of photocurrent generation.

References

[1] H. W. Kroto, J. R. Heath, S. C. O'Brien, R. F. Curl, and R. E. Smalley, Nature 318, 162 (1985).

[2] M. Endo. *Mecanisme de croissance en phase vapeur de fibres de carbone (The growth mechanism of vapor-grown carbon fibers)*. PhD thesis, University of Orleans, Orleans, France, 1975. (in French).

[3] A. Oberlin, M. Endo, and T. Koyama, *Carbon* **14**, 133 (1976).

[4] A. Oberlin, M. Endo, and T. Koyama, *J. Cryst. Growth* **32**, 335 (1976).

[5] S. Iijima, *Nature* **354**, 56 (1991).

[6] S. Iijima and T. Ichihashi, *Nature* **363**, 603 (1993).

[7] D. S. Bethune, C. H. Kiang, M. S. de Vries, G. Gorman, R. Savoy, J. Vazquez, and R. Beyers, *Nature* **363**, 605 (1993).

[8] M. S. Dresselhaus, G. Dresselhaus, and R. Saito, *Phys. Rev. B* **45**, 6234 (1992).

[9] J. W. Mintmire, B. I. Dunlap, and C. T. White, *Phys. Rev. Lett.* **68**, 631 (1992).

[10] N. Hamada, S. Sawada, and A. Oshiyama, *Phys. Rev. Lett.* **68**, 1579 (1992).

[11] J. W. G. Wildöer, L. C. Venema, A. G. Rinzler, R. E. Smalley, and C. Dekker, *Nature* **391**, 59 (1998).

[12] T. W. Odom, J. L. Huang, P. Kim, and C. M. Lieber, *Nature* **391**, 62 (1998).

[13] A. R. Goni, L. N. Pfeiffer, K. W. West, A. Pinczuk, H. U. Baranger, and H. L. Stormer, *Appl. Phys. Lett.* **61**, 1956 (1992).

[14] [O. M. Auslaender, A. Yacoby, R. de Picciotto, K. W. Baldwin, L. N. Pfeiffer, and K.W.West, *Science* **295**, 825 (2002).

[15] A. M. Chang, R*ev. Mod. Phys.* **75**, 1449 (2003).

[16] P. Kim, T. W. Odom, J.-L. Huang, and C. M. Lieber, *Phys. Rev. Lett*. **82**, 1225 (1999).

[17] L. C. Venema, J. W. Janssen, M. R. Buitelaar, J. W. G. Wildöer, S. G. Lemay, L. P.Kouwenhoven, and C. Dekker, *Phys. Rev. B* **62**, 5238 (2000).

[18] M. Bockrath, D. H. Cobden, J. Lu, A. G. Rinzler, R. E. Smalley, L. Balents, and P. L.McEuen, *Nature* **397**, 598 (1999).

[19] R. Egger, A. Bachtold, M. Fuhrer, M. Bockrath, D. Cobden, and P. McEuen, '*Interacting Electrons in Nanostructures'*, edited by R. Haug and H. Schoeller (Springer, Berlin, 2001), vol. 579.

[20] S. Frank, P. Poncharal, Z. L. Wang, and W. A. de Heer, *Science* 280, 1744 (1998).

[21] J. Nygard, D. Cobden, M. Bockrath, P. McEuen, and P. Lindelof, *Appl. Phys. A Mater. Sci. & Process. A* **69**, 297 (1999).

[22] Z. Yao, C. Dekker, and P. Avouris, 'Electrical transport through single-wall carbon nanotubes', in '*Carbon Nanotubes'*, edited by M. S. Dresselhaus, G.

Dresselhaus, and P. Avouris (Springer, Berlin, 2001), vol. 80 of Topics in Applied Physics, p. 146.

[23] P. Avouris, *Acc. Chem. Res.* **35**, 1026 (2002).

[24] A. Bachtold, P. Hadley, T. Nakanishi, and C. Dekker, *Science* **294**, 1317 (2001).

[25] C. Zhou, J. Kong, E. Yenilmez, and H. Dai, *Science* **290**, 1552 (2000).

[26] S. J. Tans, A. R. M. Verschueren, and C. Dekker, *Nature* **393**, 49 (1998).

[27] R. Martel, T. Schmidt, H. R. Shea, T. Hertel, and P. Avouris, *Appl. Phys. Lett.* **73**, 2447 (1998).

[28] C. Zhou, J. Kong, and H. Dai, *Appl. Phys. Lett.* **76**, 1597 (2000).

[29] S. J. Tans, M. H. Devoret, H. J. Dai, A. Thess, R. E. Smalley, L. J. Geerligs, and C. Dekker, *Nature* **386**, 474 (1997).

[30] M. Bockrath, D. H. Cobden, and P. L. McEuen, *Science* **275**, 1922(1997).

[31] N.D. Lang and Ph. Avouris, *Phys. Rev. B* **62**, 7325 (2000)

[32] H.J. Li, W.G. Lu, J.J. Li, X.D. Bai, and C.Z. Gu, *Phys. Rev. Lett.* **95**, 086601 (2005)

[33] F. Bussolotti, L. D'Ortenzi, V. Grossi, L. Lozzi, S. Santucci, and M. Passacantando, *Phys. Rev. B* **76**, 125415 (2007)

[34] J. Wei, J. Sun, J. Zhu, K. Wang, Z. Wang, J. Luo, D. Wu, and A. Cao, *Small* **2**, 988 (2006)

[35] J.A. Misewich, R. Martel, Ph. Avouris, J.C. Tsang, S. Heinze, and J. Tersoff, *Science* **300**, 783 (2003)

[36] J.U. Lee, *Appl. Phys. Lett.* **87**, 073101 (2005)

[37] P.V. Kamat, *Nanotoday* **1**, 20 (2006)

[38] J. Kong, N.R. Franklin, C. Zhou, M.G. Chapline, S. Peng, K. Cho, and H. Dai, *Science* **287**, 622 (2000)

[39] L. Valentini, C. Cantalini, I. Armentano, J. M. Kenny, L. Lozzi, and S. Santucci, *Diamond Relat. Mater.* **13**, 1301 (2004)

[40] J.-M. Bonard, K.A. Dean, B.F. Coll, and C. Klinke, *Phys. Rev. Lett.* **89**, 197602 (2002)

[41] H. Sugie, M. Tanemura, V. Filip, K. Iwat, K. Takahashi, and F. Okuyama, *Appl. Phys. Lett.* **78**, 2578 (2001)

[42] J. Zhang, G. Yang, Y. Cheng, B. Gao, Q. Qiu, Y.Z. Lee, J.P. Lu, and O. Zhou, *Appl. Phys. Lett.* **86**, 184104 (2005)

[43] W.B. Choi et al, *Appl. Phys. Lett.* **75**, 3129 (1999)

[44] M. Croci, I. Arfaoui, T. Stöckli, A. Chatelain, and J.-M. Bonard, *Microelectron. J.* **35**, 329 (2004)

[45] P. A. Williams, S. J. Papadakis, A. M. Patel, M. R. Falvo, S. Washburn, and R. Superfine, *Appl. Phys. Lett.* **82**, 805 (2003).

[46] A. M. Fennimore, T. D. Yuzvinsky, W.-Q. Han, M. S. Fuhrer, J. Cumings, and A. Zettl, *Nature* **424**, 408 (2003).

[47] M.S. Dresselhaus, G. Dresselhaus & P. Eklund, ‘‘*The science of fullerenes and carbon nanotubes*’’, Academic (1996).

[48] C. Qin and L.-M. Peng, *Phys. Rev. B* **65**, 155 431 (2002).

[49] T. W. Odom, J. H. Hafner, and C. M. Lieber, ‘Scanning probe microscopy studies of carbon nanotubes’, in ‘*Carbon Nanotubes’*, edited by M. S. Dresselhaus, G. Dresselhaus and P. Avouris (Springer, Berlin, 2001), vol. 80 of Topics in Applied Physics, p. 173.

[50] X. B. Zhang, X. F. Zhang, S. Amelinckx, G. Van Tendeloo, and J. Van Landuyt, *Ultramicroscopy* **54**, 237 (1994).

[51] M. Gao, J. M. Zuo, R. D. Twesten, I. Petrov, L. A. Nagahara, and R. Zhang, *Appl. Phys. Lett.* **82**, 2703 (2003).

[52] P.R.Wallace, *Phys. Rev.* **71**, 622 (1947).

[53] R. Saito, M. Fujita, G. Dresselhaus, M.S. Dresselhaus, *Appl. Phys. Lett.* **60**, 2204 (1992).

[54] R. Saito, G. Dresselhaus, and M. S. Dresselhaus, ‘*Physical Properties of Carbon Nanotubes’* (Imperial College Press, London, 1998).

[55] X. Blase, L. X. Benedict, E. L. Shirley, and S. G. Louie, *Phys. Rev. Lett.* **72**, 1878 (1994).

[56] M. Machon, S. Reich, C. Thomsen, D. Sanchez-Portal, and P. Ordejon, *Phys. Rev. B* **66**, 155410 (2002).

[57] R.A. Jishi, M. S. Dresselhaus, and G. Dresselhaus. *Phys. Rev.* B, 47, 16671 (1993).

[58] C.H. Olk, J.P. Heremans, *J. Mater. Res.* **9**, 259 (1994).

[59] P.C. Eklund, J.M. Holden, R.A. Jishi, *Carbon* **33**, 959 (1995).

[60] T.W. Ebbesen, *Carbon Nanotubes*, Edited by T.W. Ebbesen, CRC Press(Boca Raton, New York, London, Tokyo) 1997, Chapter I.

[61] T. W. Odom, J. L. Huang, P. Kim, M. Ouyang, and C. M. Lieber, *J. Mater. Res.* **13**, 2380 (1998).

[62] P. Kim, T. Odom, J.-L. Huang, and C. M. Lieber, *Phys. Rev. Lett.* **82**, 1225 (1999).

[63] H. Ajiki and T. Ando, *Physica B, Condensed Matter* **201**, 349 (1994).

[64] S. Kazaoui, N. Minami, R. Jacquemin, H. Kataura, and Y. Achiba, *Phys. Rev. B* **60**, 13339 (1999).

[65] H. Kataura, Y. Kumazawa, Y. Maniwa et al., *Synth. Met.* **103**, 2555 (1999)

[66] A. Kasuya, Y. Sasaki, Y. Saito, K. Tohji, and Y. Nishina, *Phys. Rev. Lett.* **78**, 4434 (1997).

[67] M. A. Pimenta, A. Marucci, S. Empedocles, M. Bawendi, E. B. Hanlon, A. M. Rao, P. C. Eklund, R. E. Smalley, G. Dresselhaus, and M. S. Dresselhaus, *Phys. Rev. B* **58**, R16016 (1998).

[68] S. M. Bachilo, M. S. Strano, C. Kittrell, R. H. Hauge, R. E. Smalley, R. B. Weisman, *Science* **298**, 2361 (2002)

[69] T. Pichler, M. Knupfer, M. S. Golden, and J. Fink, A. Rinzler and R. E. Smalley, *Phys. Rev. Lett.* **80**, 4729 (1998)

[70] O. Jost, A. A. Gorbunov, W. Pompe, T. Pichler, R. Friedlein, M. Knupfer, M. Reibold, H.-D. Bauer, L. Dunsch, M. S. Golden, and J. Fink, *App. Phys Lett.* **75** 2217 (1999)

[71] X. Liu, T. Pichler, M. Knupfer, M. S. Golden, J. Fink1, H. Kataura, and Y. Achiba, *Phys. Rev. B* **66**, 045411 (2002)

[72] M. De Crescenzi, M. N. Piancastelli, '*Electron Scattering and Related Spectroscopy*', Ed. World Scientific Publishing Co. Ptc. Ltd. 1996 Par. 4

[73] R. Kuzno, M. Terauchi, M. Tanaka, and Y. Saito, *Jpn. J. Appl. Phys.*, Part 2 **33**, L1316 (1994)

[74] L. A. Bursill, P. A. Stadelmann, J. L. Peng, and S. Prawer, *Phys. Rev. B* **49**, 2882 (1994).

[75] Z. F. Ren et al., *Appl. Phys. Lett.* **75**, 1086 ~1999!.

[76] T. Iwasaki, T. Motoi, and T. Den, *Appl. Phys. Lett.* **75**, 2044 (1999).

[77] Y.-K. Kwon and D. Tománek, *Phys. Rev.* B **58**, R16001 (1998).

[78] C.-H. Kiang, M. Endo, P. M. Ajayan, G. Dresselhaus and M. S. Dresselhaus, *Phys. Rev. Lett.* **81**, 1869 (1998).

[79] C. Schönenberger, A. Bachtold, C. Strunk, J.-P. Salvetat, and L. Forro, *Appl. Phys. A* **69** 283 (1999).

[80] F. L. Shyu and M. F. Lin, *Phys. Rev. B* **62**, 8508 (2000)

Chapter 3

Synthesis of Carbon Nanotubes

Several growth methods for carbon nanotubes have been developed and are divided into three general techniques: arc discharge, laser ablation, and chemical vapour deposition (CVD). The specific choice depends on the application that nanotubes have to be grown for. Potential applications may require either large quantities of bulk materials or device integration in a scale-up way. Another important factor is the purity of the produced nanotubes. The first two methods require post-growth purification to separate the CNTs from other carbonaceous products such us fullerenes, graphitic polyhedrons with enclosed metal particles, and amorphous carbon in the form of particles or overcoating on the nanotube sidewalls. CVD methods promise to produce higher quality nanotube materials at large scales. Moreover, controlled CVD growth strategies on catalytically patterned substrates yield ordered nanotube architectures and integrated devices.

A large part of this work has been devoted to the MWNTs synthesis by CVD technique. In this Chapter, first a brief description of all the synthesis techniques as well as some of the nanotubes growth models will be illustrated. Then, a description of the experimental CVD set-up and the different kind of MWNTs samples obtained by varying the experimental conditions will be described. The morphology and structure will be characterized by electron microscopy techniques. Finally the results of nanotubes decoration by metal nanoparticles, as well as the selective deposition on patterned substrates, will be presented.

3.1 Synthesis methods.

The techniques to obtain carbon nanotubes are mostly divided in three categories: *arc-discharge*, *laser ablation*, and *CVD*.

The first two methods involve the condensation of carbon atoms generated from evaporation of solid carbon sources. The temperatures achieved by these methods are locally close to the melting temperature of graphite (that is about 3650°C). These synthesis methods have both the advantage to produce high-quality nanotubes. A disadvantage of the vaporisation methods is just the high temperature locally required for solid carbon feedstock, that limits the scale-up of the processes. Furthermore, the various by-products (e.g. amorphous carbon and several nanoparticles such as fullerenes) have to be removed by subsequent purification.

CVD growth process involves the dissociation of hydrocarbon molecules catalyzed by the transition metal, dissolution and consequent saturation of carbon atoms onto the metal nanoparticle. The CVD method has the advantage to produce lower quantities of by-products. The graphitization degree of such nanotubes, compared to those produced by arc discharge or laser ablation, is lower owing to lower synthesis temperatures.

3.1.1 Arc-discharge.

In arc-discharge, carbon atoms are evaporated by a plasma of helium gas ignited by high currents passing through opposing carbon anode and cathode (Fig. 1).

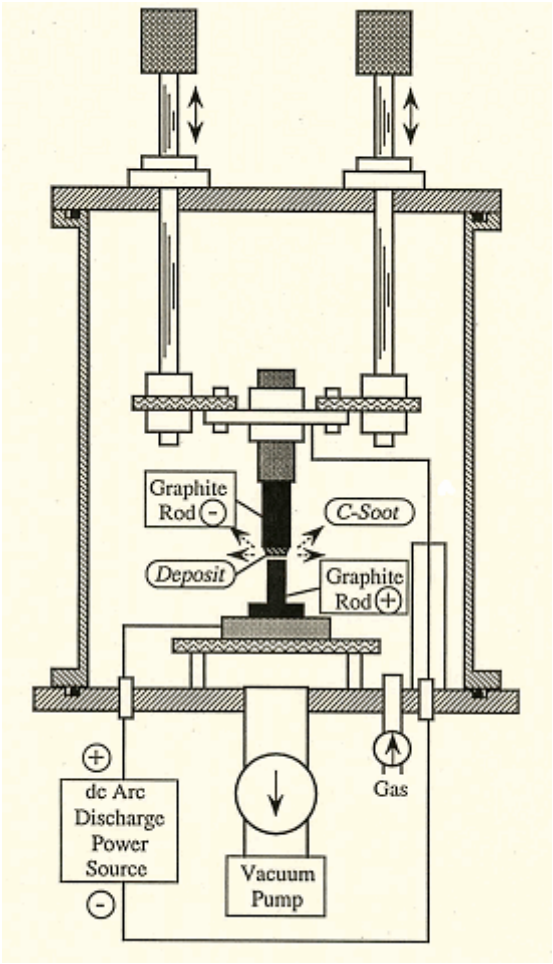

Fig. 1. Outline of experimental set-up for arc discharge synthesis of CNTs.

This process produces a hard grey shell which is commonly defined "*soot*", at a rate of 1 mm/min on the negative electrode (cathode), whereas the positive electrode (anode) is continuously consumed. The soot inner core contains carbon nanotubes and nested polyhedral graphite particles. Carbon nanotubes contained in the cathodic deposit normally have multi-walled structures [1]. The quantity and quality of the obtained nanotubes depend on various deposition parameters such as inert gas pressure, kind of gas, current and system geometry. Also the anode - cathode distance is a relevant parameter, it is adjusted in order to obtain strong visible vortices around the cathode, enhancing anode vaporisation and favouring nanotubes formation.

Arc-discharge is the technique by which CNTs were observed for the first time by Iijima [2]. He found that the central core of the cathodic deposit contained a variety of graphitic structures of a type which had never previously been observed. Among them, he discovered graphitic nanoparticles and nanotubes. A short time later, Thomas Ebbesen and Pulickel Ajayan, from Iijima's lab, showed how nanotubes could be produced in bulk quantities by varying the arc-evaporation conditions [3].

The nanotubes typically have diameters around 5-30 nm and lengths around 10 μm. The nanotubes are bound together by strong van der Waals interactions and form tight bundles. MWNTs produced by arc discharge are very straight, that is indicative of their high crystallinity. As grown materials present few defects such as pentagons or heptagons existing on the sidewalls of the nanotubes. The by-product of the arc-discharge growth process are multi-layered graphitic particles in polyhedron shapes.

A major event in the development of carbon nanotubes was the synthesis in 1993 of single-layer nanotubes. For the growth of single-walled tubes, a metal catalyst is needed in the arc-discharge system. Iijima's group [4], as well as Bethune and colleagues [5], found that addition of metals as cobalt to the graphite electrodes resulted in extremely fine tube with single-layer walls. However, the yield of carbon nanotubes was low, and there were large amounts of metal carbide clusters and amorphous carbon attached to the nanotubes (Fig. 2).

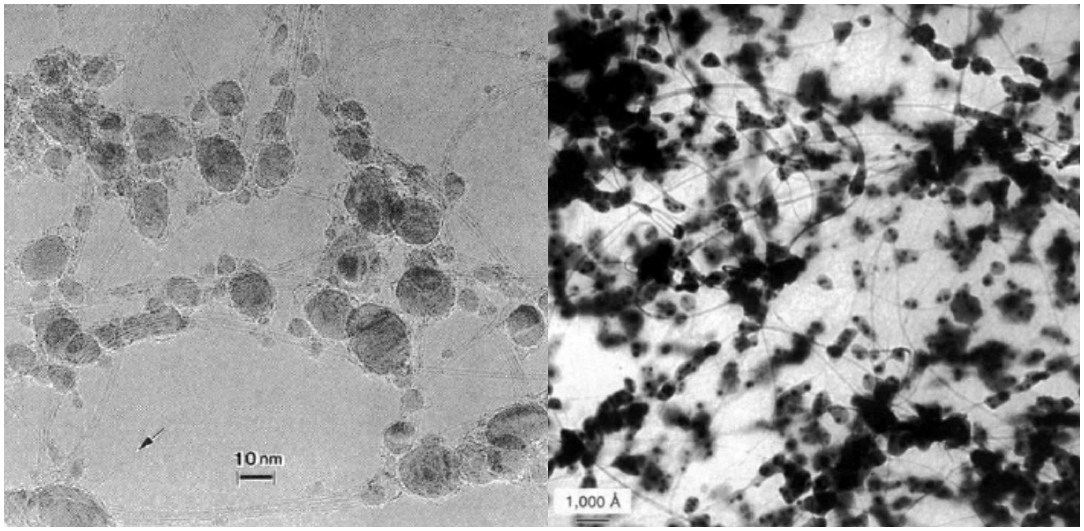

Fig. 2. Transmission electron micrographs showing bundles of single wall carbon nanotubes. Dark blobs are iron carbide particles (left, [4]) and cobalt clusters (right, [5]) which assist SWNTs growth.

3.1.2 Laser Ablation.

A graphite target is vaporised by laser irradiation in an inert gas atmosphere. To describe how this technique works, in Fig. 3 the apparatus used by Smalley's group, which obtained high quality SWNT by laser ablation in 1995 for the first time, is pictured [6].

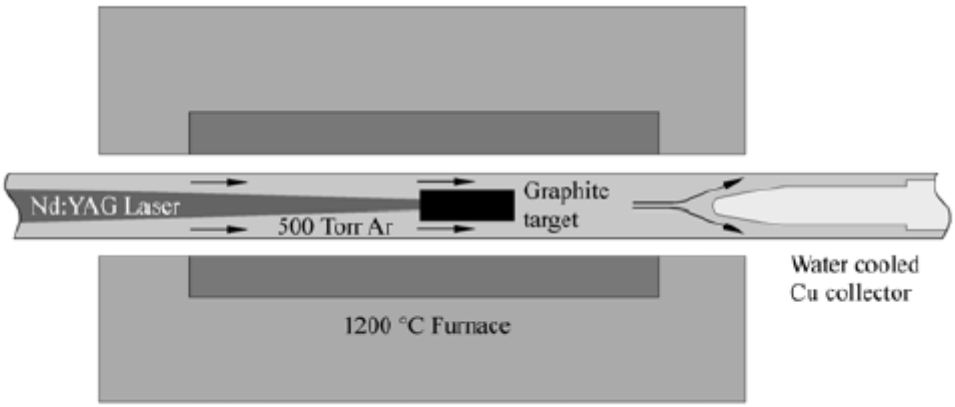

Fig. 3. Set up of laser ablation apparatus.

They utilized intense laser pulses to ablate a carbon target containing 0.5 atomic percent of nickel and cobalt. The target was placed in a tube-furnace heated to 1200 °C. During laser ablation, a flow of inert gas passed through the growth chamber to carry the grown nanotubes downstream to be finally collected on a cold finger. The produced SWNTs are mostly in the form of ropes. Each rope is composed by tens of individual nanotubes, showing uniform diameters, close-packed into hexagonal crystals via Van der Waals interactions (Fig. 4).

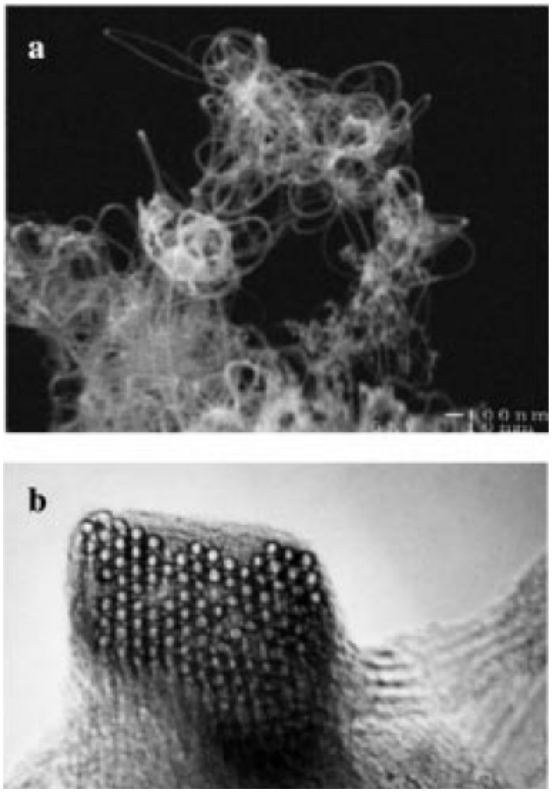

Fig. 4. SEM (a) and TEM (b) micrographs of SWNT in the form of ropes (from Smalley and co-workers).

In CNT growth by arc-discharge and laser ablation, typical by-products are fullerenes, graphitic polyhedrons with enclosed metal particles, and amorphous carbon in the form of particles or overcoating on the nanotube sidewalls. A purification process for SWNT-based materials has been developed by Smalley himself and collaborators [7] and is at present widely used by many researchers. The method involves the refluxing of as-grown SWNTs in a nitric acid solution for an extended period of time. Such process induces an oxidation and removal away of amorphous carbon species and some of the metal catalyst ones.

3.1.3 CVD

Chemical vapour deposition (CVD) synthesis is achieved by fluxing a hydrocarbon gas in a reaction chamber, which hosts substrates decorated by catalyst particles. An activation source, such as a plasma or a resistively thermal heated coil, transfers energy to the gaseous carbon molecule (Fig. 5).

Hydrocarbon works as a feedstock while catalyst particles work as seeds for nanotube growth. Commonly used gaseous carbon sources include methane, carbon monoxide and acetylene. The energy source is used to "crack" the molecule into reactive atomic carbon. Successively, the reactive carbon diffuses towards the substrate, which is heated and coated by a catalyst (usually 3d transition metal such as Ni, Fe or Co), where carbon can react forming strong chemical bonds. Carbon nanotubes will be grown if the proper deposition parameters are maintained. Excellent alignment [8-9] and ordered nanotube structures [10-11], as well as positional control at a nanometer scale [12], can be achieved by using CVD techniques. Control over the diameter, as well as the growth rate of the nanotubes has also to be guaranteed. The appropriate metal catalyst can preferentially allow the growth of single rather than multi-walled nanotubes [13]. CVD carbon nanotube synthesis is essentially a two-step process consisting of a catalyst preparation step followed by the actual synthesis of the nanotube. The catalyst is generally prepared by sputtering of a transition metal onto a substrate. Then, the catalyst is treated performing chemical etching and/or thermal annealing. Chemical etching is useful to provide a specific patterning for selective deposition of nanotubes. Thermal annealing results in cluster formation on the substrate, from which the nanotubes will grow. The temperatures for the synthesis of nanotubes by CVD are generally within the 600-900 °C range [8,12], [14-15].

The major pitfall for CVD grown MWNTs is the high defect density in their structures. The defective nature of CVD-grown MWNTs remains to be thoroughly understood, but is most likely due to the relatively low growth temperature, which is not sufficient to provide adequate thermal energy to anneal nanotubes into perfectly crystalline structures.

Different techniques for carbon nanotubes synthesis by CVD have been developed, such as plasma-enhanced (PE) CVD, thermal CVD, alcohol catalytic CVD, vapour phase growth, aero gel-supported CVD and laser assisted CVD.

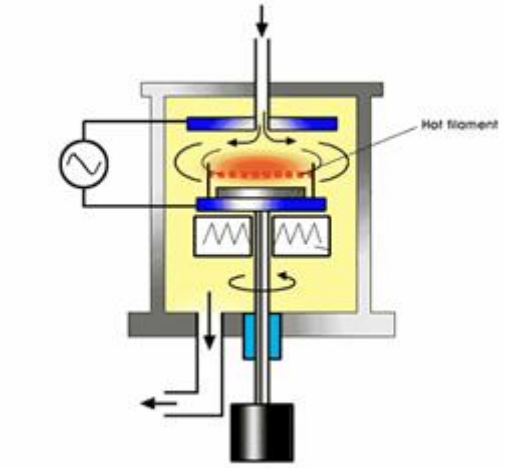

Fig. 5. Plasma-enhanced CVD method generates a glow discharge in a chamber or a reaction furnace by a high frequency voltage applied to both electrodes

3.2 Growth of MWNT by CVD

The general nanotube growth mechanism in a CVD process involves the dissociation of hydrocarbon molecules catalyzed by the transition metal, and dissolution and saturation of carbon atoms in the metal nanoparticle. The precipitation of carbon from the saturated metal particle leads to the formation of tubular carbon solids in sp^2 structure. Tubule formation is favoured over other forms of carbon such as graphitic sheets with open edges. This is because a tube contains no dangling bonds and therefore satisfied conditions of minimum free-energy. Growth terminates when the catalyst particle gets poisoned by impurities or after the formation of a stable metal carbide. This mechanism is based on in-situ TEM observations [16].

For nanotube growth, most of the CVD methods employ ethylene or acetylene as carbon feedstock. The growth temperature is typically in the range of 600-900 °C. Iron, nichel or cobalt nanoparticles are often used as catalyst. At high temperatures, carbon has finite solubility in these metals, that is related to the formation of metal-carbon solutions and therefore the consequent growth mechanism. Depending on the size of the catalyst particles, SWNT or MWNT are grown with different diameters.

One general theory [13] postulates that metal catalyst particles are floating or are supported on graphite or another substrate. It presumes that the catalyst particles are spherical or pear-shaped. In that case the deposition will take place on only one half of the catalyst surface (this is the lower curvature side for the pear shaped particles). The carbon diffuses along the concentration gradient and precipitates on the opposite half, around and below the bisecting diameter. However, it does not precipitate from the apex of the hemisphere, which accounts for the inner channel that is characteristic of these tubules. For supported metals, CNTs can be formed either by extrusion, *base growth*, in which the nanotube grows upwards from the metal particles that remain attached to the substrate, or the particles detach and move at the head of the growing nanotube, *tip-growth* (Fig. 6).

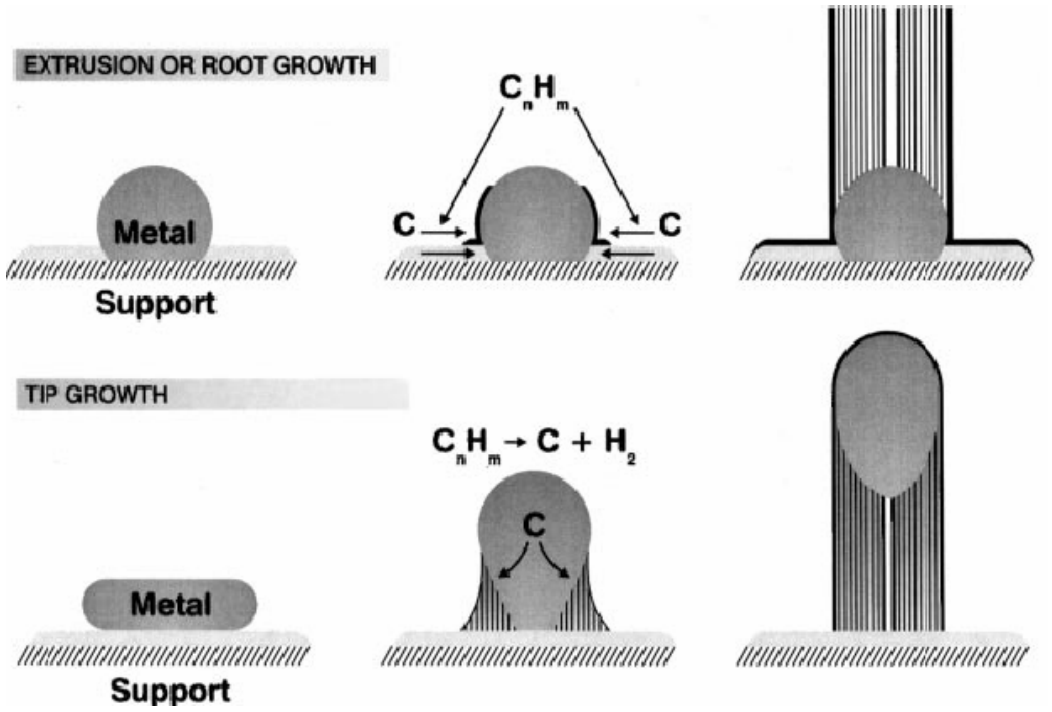

Fig. 6. Two general growth modes of nanotube in chemical vapour deposition. Left diagram: base growth mode. Right diagram: tip growth mode

In the tip growth model the tube remains closed during the deposition, the longitudinal growth of the tube occurs by the continuous incorporation of small carbon clusters (C_2 dimers). This C_2 absorption process is assisted by the presence of pentagonal defects at the tube end, allowing bond-switching in order to reconstruct the cap topology [17-18].

In the base growth model, the nanotubes are open during the growth process and carbon atoms are added at their open ends [19-20]. If the nanotube has a random chirality, the adsorption of a C_2 dimer at the active dangling bond edge site will add one hexagon to the open end. Closure of the layer is caused by the nucleation of pentagonal rings due to local perturbations in growth conditions or due to the competition between different stable structures. Thickening of the tubes occurs by layer growth on already grown inner-layer templates. The large growth anisotropy results from the significantly different rates of growth at the high-energy open ends in comparison the non-reactive basal planes (Fig. 7).

Fig. 7. Picture for the open-end growth of the nanotube. Tube ends are open while growing by accumulating carbon atoms at the tube peripheries. Once the tube is closed, there will be no more growth on that tube but new tube shells start to grow on the sidewalls.

Quantum molecular dynamics simulations have been performed to understand the nucleation and growth process both of SWNTs and MWCNTs, as well as different growth models have been proposed, but a detailed description is beyond the aim of this thesis. Instead, a brief description of the recent results on the in-situ study of CNT formation is reported in the following, taking advantage of recent technological improvements in microscopy. Hofmann et al. experimentally observed the catalyst dynamics during surface-bound CNT nucleation combining atomic-scale environmental transmission electron microscope (ETEM) and in-situ time resolved X-ray photoelectron spectroscopy (XPS) [21]. CNTs nucleated by exposing isolated Ni nanoparticles to acetylene. The ETEM videos showed that the formation of graphitic carbon had leaded to the dynamic reshaping of the catalyst particle. Such reshaping mechanism is responsible of the graphitic layer(s) morphology of the carbon nanotube during further growth (Fig. 8). SWNTs nucleate by the lift-off of a carbon cap. The carbon cap appears to initially replicate the shape of the apex of a triangular/pyramidal metal particle. The carbon network expands by lifting off from the catalyst particle, which itself is thereby restructured. The growing nanotube forces its shape onto the Ni cluster. The nanotube constrains the Ni particle to a more cylindrical shape. Growth terminates when the tangential graphitic lattice encapsulates the catalyst particle down to its support interface.

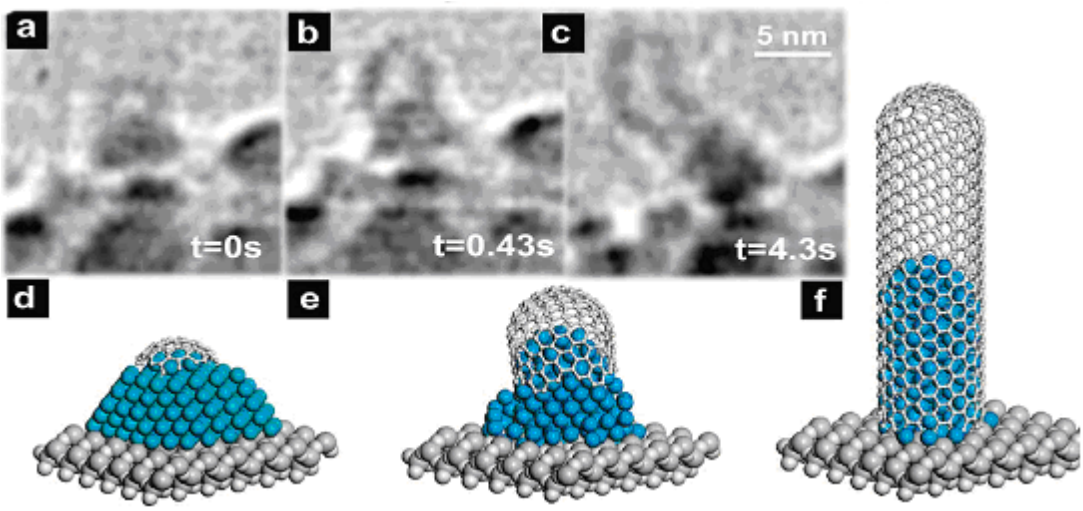

Fig. 8. (a-c) ETEM image sequence of Ni-catalyzed CNT root growth. The time of the respective stills is indicated. (d-f) Schematic ball-and-stick model of different SWNT growth stages. [21]

TEM investigations, including in situ heating experiments, enabled to directly observe the surface segregation of graphite at the expense of the encapsulated catalyst material. The observations suggest that the structural growth process is determined by the dissolution of carbon in the quasi-liquid catalyst particle, its diffusion through the particle, and its segregation in the form of graphene layers in supersaturation conditions. These processes have been proved to occur via the formation of an intermediate iron carbide phase. The results also demonstrated the gradual displacement of the fluid catalyst during nanotube growth.

3.3 Experimental Set-up & Synthesis

The CNTs in the laboratory of the Department of Physics at Tor Vergata University are synthesized in a CVD reactor (Fig.9) on a solid substrate, typically SiO_2 or Si, covered by metal catalyst, Fe. The substrate is placed on a Macor holder and is heated to supply the energy necessary to dissociate the hydrocarbon molecules into active carbon atoms during the growth process (minimum temperature to crack acetylene molecules in atomic carbon is about 500˚C). A 3 conductors electrical feedthrough is used to inject current to the substrate as well as to mechanically sustain the sample (Fig.9).

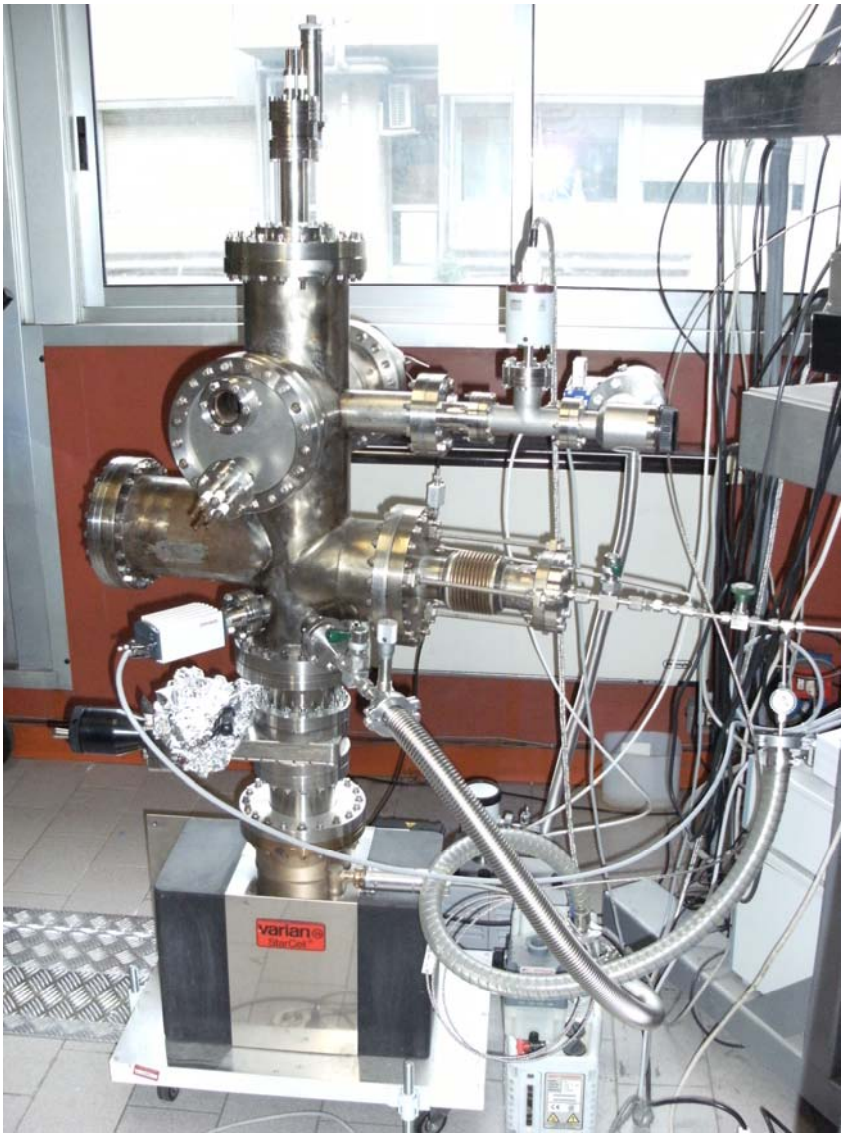

Fig. 9. Picture of the CVD chamber at the Dept. of Physics, University of Rome "Tor Vergata"

The synthesis process can be divided into two step:

1) deposition of metal catalyst;

2) CNT growth process.

In the first phase, the chamber is evacuated by a ionic pump in series to a turbo molecular and a rotary pump, from the atmospheric pressure down to 10^{-8} Torr. Fe catalyst is physically evaporated from a tungsten crucible injecting current by means of a high-power current generator. The deposit thickness is controlled by a quartz microbalance. Fig. 43

In the second phase, accurate control of inert gas and acetylene gas fluxes supplied by a gas line represents the crucial procedure. The process pressure is adjusted by a rotary pump and is usually set at about 10 Torr. The substrate is heated by Joule effect injecting current and its temperature is measured by a pyrometer through a chamber window.

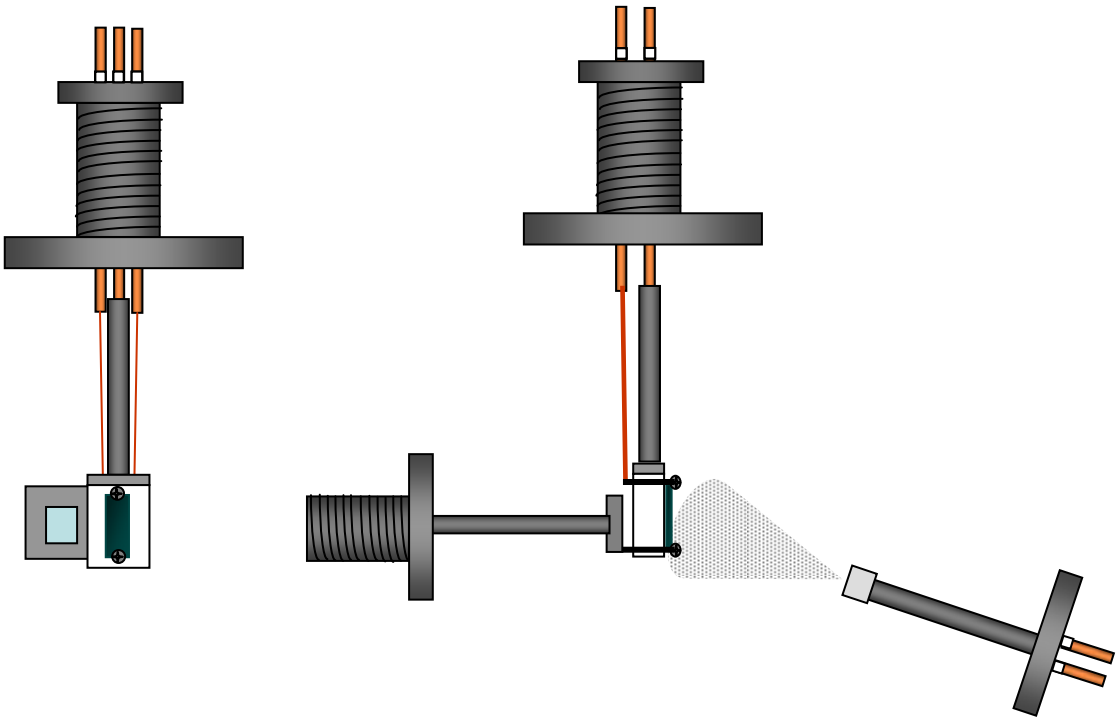

Fig. 10. Scheme of the head of the chamber supporting the substrate. The substrate is heated by Joule effect. The current is injected by two electrodes in contact with the screws fixing the substrate to the holder of macor. Behind and close to substrate a quartz microbalance to control the thickness of the catalyst layer evaporated by a tungsten crucible.

3.3.1 Deposition of catalyst

Preliminarily the SiO_2(Si) substrate (sized 4 × 21 mm^2) is chemically cleaned by cyclic ultrasonic baths in trichloroethylene, ethylene alcohol and distilled water (20 min). Then it is mounted on the sample holder shown in Fig. 10 and it is introduced into the chamber. A ionic pump in series to a turbo molecular and a rotary pump is used to evacuate the chamber down to 10^{-8} Torr. The pressure is monitored by a full range gauge, IONIVAC ITR 90 (Leybold Vakum) that works using a hot-cathode ionization measurement system (for $P < 2\times10^{-2}$ Torr), and a Pirani gauge (for $P > 5\cdot10^{-3}$ Torr). The iron (purity 99.99+) catalyst is deposited on the substrate, held at room temperature, by thermal evaporation from a tungsten basket (purity 99.9+). The control of the Fe deposition rate and nominal thickness is provided by a quartz microbalance. A linear transfer mechanism allows to set the value of the growth rate of catalyst before exposing the substrate. Moreover, exposing the substrate to the plume of evaporated catalyst atoms, it is possible to have a control feedback due to the close proximity of the microbalance to the substrate (see Fig.10). Submonolayer Fe coverage produces three-dimensional cluster formation Fig.11. The catalyst nanoparticles size and distribution is fundamental to control the size of the CNTs and their wall number [21-22]. The smaller the catalyst particles are, the smaller the diameter of CNTs is.

To make the catalyst deposition a valid tool to control the size of CNTs, a preliminary analysis has been performed by scanning tunnelling microscopy (STM) on the iron layer obtained on SiO_2 varying the Fe nominal thickness. STM images have been acquired by an OMICRON UHV STM-MFM equipment working at room temperature. The tips are made of tungsten, the maximum scan area is of 5 μm x 5 μm (for a detailed description of the STM technique see Appendix A). Different regions and resolution have been selected. In Fig.11 the images of a 0.2 nm nominal thickness Fe layer on SiO_2 are shown at different resolutions.

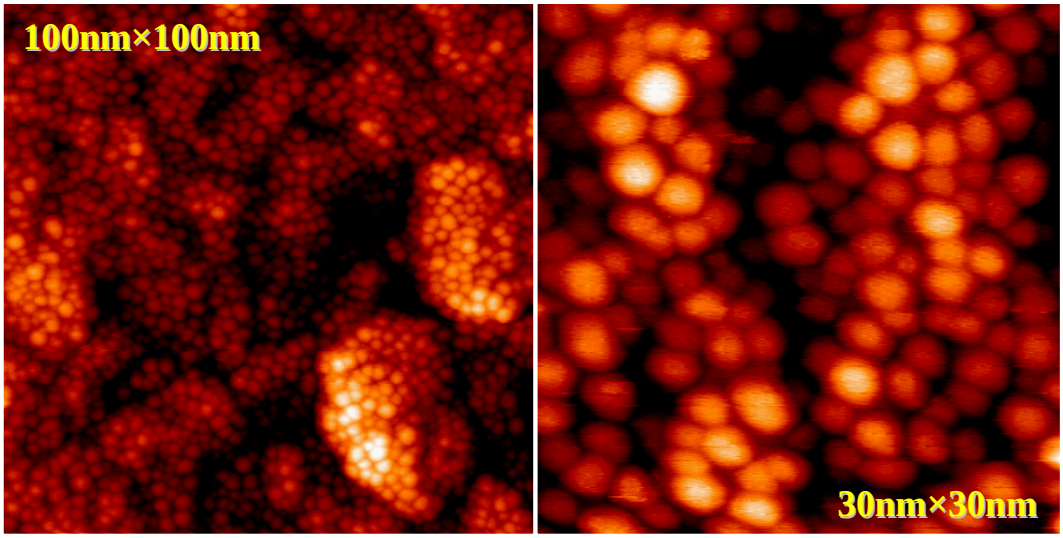

Fig. 11. STM images of Fe coverage layer deposited on a SiO_2 substrate. The nominal thickness of catalyst is 0.2 nm. To the left, a 100×100 nm area is acquired and to the right an area image acquired with more high resolution, 30×30 nm. It is evident the nanoparticle formation.

Three different nominal deposited thicknesses onto SiO_2 have been analysed by STM: 0.2 nm, 0.5 nm and 1.0 nm. The size distribution of Fe nanoparticles is obtained from a statistical analysis performed on several collected images of 30nm×30nm resolution (see Fig.12). The average diameter of such nanoparticles has been evaluated by means of an image elaboration software, averaging about 40 structures in each image for improving the statistical significance. The average size have been calculated by the superimposition of a multi-Gaussian (or Lorentzian) fit to the diameter's histogram and the results are reported in Table 1. For the 0.2 nm thick layer, a mean size of 1.9 nm is found; for the 0.5 nm thick layer, the mean size is of 2.5 nm; finally for 1 nm thick layer, a value of 4.2 nm is calculated. These results allow to relate the nominal thickness of the deposited layer of catalyst to the mean size of nanoparticles and to the resultant CNTs diameter. Specifically, the thinner the initial catalyst layer is the smaller the islands are.

Nominal Fe thickness (nm)	Mean nanoparticles size (nm)
0.2	1.9
0.5	2.5
1.0	4.2

Table 1. Mean diameter of iron nanoparticles in function of the nominal thickness of deposited catalyst. There is a trend of the mean size that result to be almost ten times the nominal thickness.

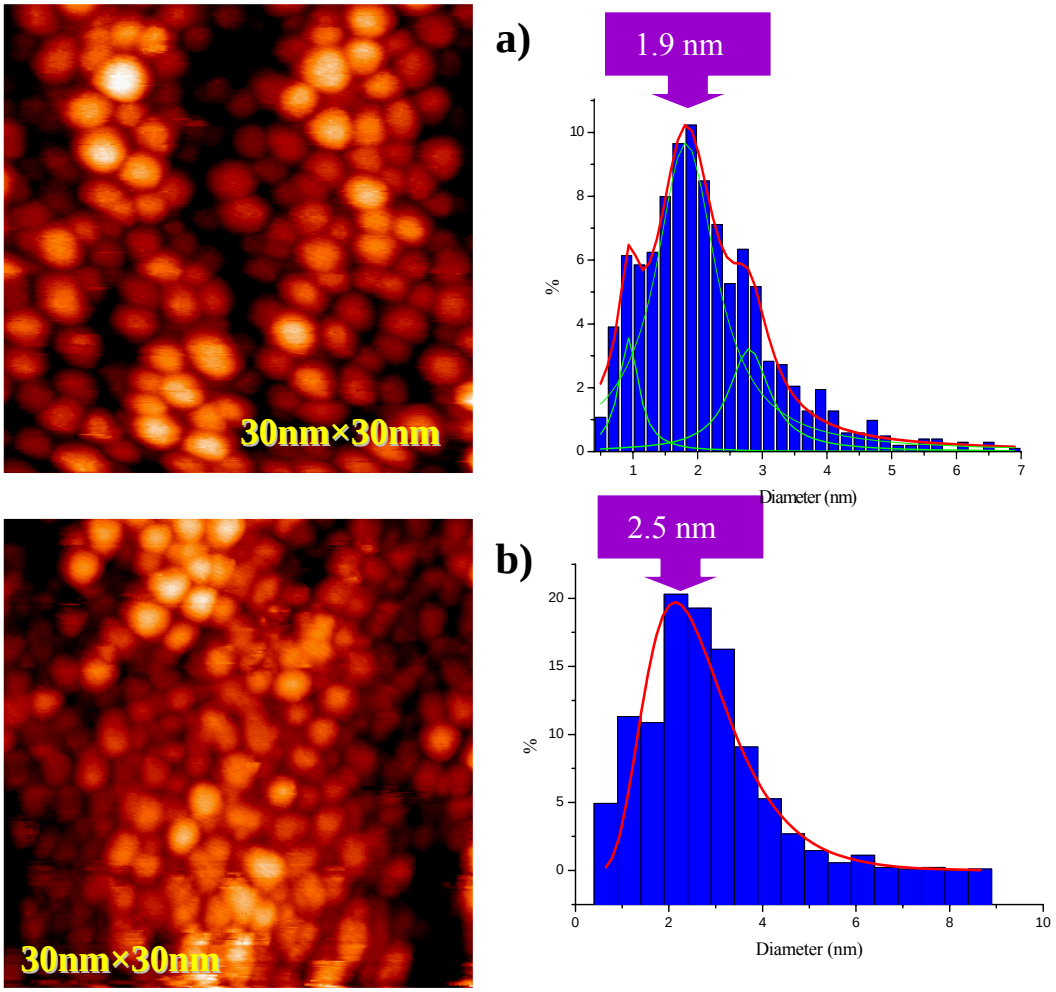

Fig. 12. Statistical analysis results of size distribution of Fe coverage nanoparticle on SiO_2 substrate varying the Fe nominal thickness. a) to the left the STM images of a 30 nm x 30 nm area of a 0.2 nm thick layer, to the right the relative histogram of nanoparticle size and the relative mean size of 1,9 nm. b) to the left the STM images of a 30 nm x 30 nm area of a 0.5 nm thick layer, to the right the relative histogram of nanoparticle size and the relative mean size of 2.5 nm.

3.3.2 CNTs growth process

After the catalyst deposition, the chamber is filled with inert gas, Ar (tens of Torr), and then the substrate is heated by Joule effect injecting current through the feedthrough by the electrodes connected to the two screws that fix the substrate to the sample holder (see Fig. 10). The high-power current generator is an ELIND 200KL 6/15. The Ar atmosphere is used to homogeneously heat the substrate and to avoid the substrate temperature abruptly changes when the chamber in vacuum is filled by the hydrocarbon gas. The temperature substrate ranges from 750°C to 900°C as a function

of the specific substrate (Si, SiO_2) and it is measured by a pyrometer trough a window (MINOLTA/LAND, Infra-red thermometer). The temperature provides the energy source able to dissociate the hydrocarbon into C atoms close to the substrate. Then acetylene is fluxed into the chamber, alone or in a mixture of hydrocarbon and inert gas (up to 200 sccm of C_2H_2). The flux rate and the content percentage of mixtures are controlled by means of two MKS mass flow-meters, mastered by a 4 channel mass flow controller, IONVAC. A process rotary pump allows to keep the chamber pressure constant during the growth process (typically chamber pressure tens of Torr). The process pressure is monitored by an absolute pressure transducer, independently from the type of gases in chamber (Baratron MKS, $1 \div 10^4$ Torr). After the deposition time (usually ten minutes), Ar is fluxed into the chamber to prevent the possible formation of carbonaceous (amorphous carbon) species before decreasing the substrate temperature. The pump is then stopped and the Ar (500 sccm) continue to flux until the pressure of chamber reaches the atmospheric pressure.

Varying the experimental parameters as pressure, gases flux rate, substrate temperature, deposition time as well as the thickness of catalyst layer, it is possible to obtain different MWNTs. It is possible to control their size distribution, wall number distribution, spatial organization and the amount of structural defects and carbonaceous species present as by-product.

Preliminary information about the results of the growth process, such as the presence of CNTs, their density and spatial organization, presence of defects and/or impurities, has been obtained by Scanning Electron Microscope, SEM (see Appendix B).

3.3.3 Morphology and structure: SEM characterization

SEM measurements have been performed at CNR - Institute of Complex Systems of Montelibretti (Rome). SEM images of MWCNTs grown on a substrate have been recorded using a Cambridge Stereo Scan 360 apparatus (LaB_6 filament). The SEM results furnish a first feedback on the influence of deposition parameters as substrate temperature, substrate type, gas fluxes, deposition time.

For example we have been able to determine an upper limit substrate temperature, T_{sub}, for deposition on a crystalline Silicon <111> substrate. In Fig.13 we compare the results of two different depositions where the only varying parameter is T_{sub}. SEM images clearly reveal that for $T_{sub} \geq 800$ °C, very few, sparse and short nanotubes can be obtained (Fig. 46 c) and b)). Consequently, it has been possible to fix an optimal value of T_{sub}, ranging from 700 to 750 °C, for crystalline Si substrate to obtain a very high and homogeneous density of CNTs, long at least some micrometers (Fig. 46 c) and d)).

An explanation is that temperatures around 800°C promote the formation of iron silicides that reduce the catalytic effect of Fe particles. Thus a relatively thick SiO_2 layers (hundreds of nm) was used as a diffusion barrier preventing reaction between Si and Fe. On the SiO_2 surface, Fe particles do not form silicide below 1000 °C as the synthesis results in Fig. 47-48 show [23, 24].

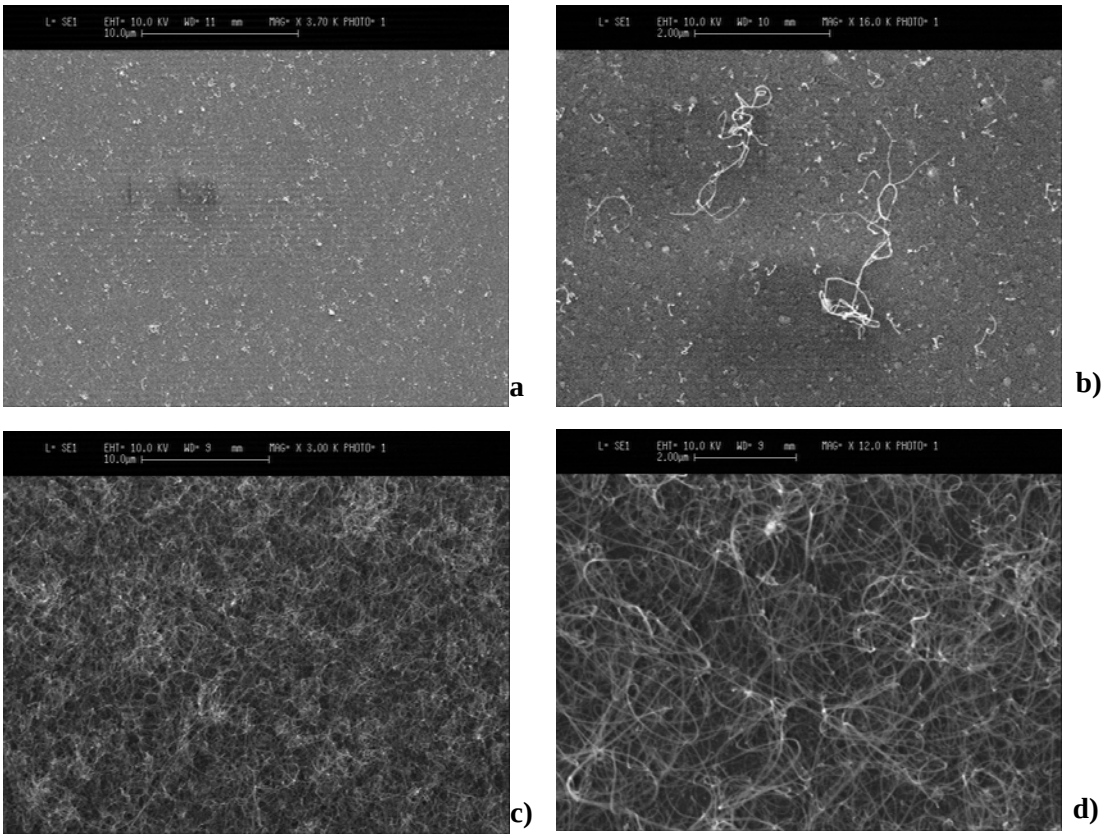

Fig. 13. SEM images of the results of two different CNTs synthesis process on Si <111> substrate. The only parameter varying is the temperature substrate. For T_{sub} = 800°C very few, sparse and short nanotubes are grown ((a) and (b)). For lower temperature 730 °C a very homogeneous high density of CNTs, long at least some micrometer, is obtained ((c) and (d))

A very important information delivered by scanning electron microscopy is the CNTs orientation and how the experimental growth parameters influence it.

In Fig.14 and Fig.15 two different samples of CNTs are shown. The nanotubes have been grown on a silicon dioxide SiO_2 substrate of 500 nm, thermally grown on Si<100>. The SEM images have been acquired tilting the sample stage at tilt angles of 60° and 90° respectively. The CNTs of the first sample have a very disordered three-dimensional orientation (Fig. 14), while the second ones are very well aligned perpendicularly to the substrate (Fig. 15). The experimental parameters were for the first sample T_{sub}, (800 ± 15) °C, C_2H_2 = 75 sccm, and P_{ch} = (12 ± 2) Torr, and for the second one T_{sub}, (800 ± 15) °C, C_2H_2 = 200 sccm, and P_{ch} = (50 ± 4) Torr. So in this case the substrate temperature is not the key parameter for the alignment, but the relative pressure and flux of hydrocarbon.

We assume that the mechanism of nanotube self-orientation is related to the base growth mode. During CVD growth, the outermost walls of nanotubes interact with their neighbours via Van der Waals forces to form a rigid bundle, which allow the nanotubes to grow perpendicular to the substrate. For the CNT synthesized by fluxing 200 sccm of C_2H_2 at 50 Torr, the density of active carbon molecules on the proximity of substrate is obviously higher then those of the CNT grown fluxing 75 sccm of gas at 12 Torr. The higher density increases the number of C / catalyst nuclei giving rise to CNTs. Due to the fact that the substrate is continuously covered by the catalyst nanoparticles, (Fig.11), in presence of large amount of carbon feedstock, multi-walled nanotubes can self-assemble into aligned structures as they grow, and the driving force for self-alignment is the Van der Waals interactions between nanotubes.

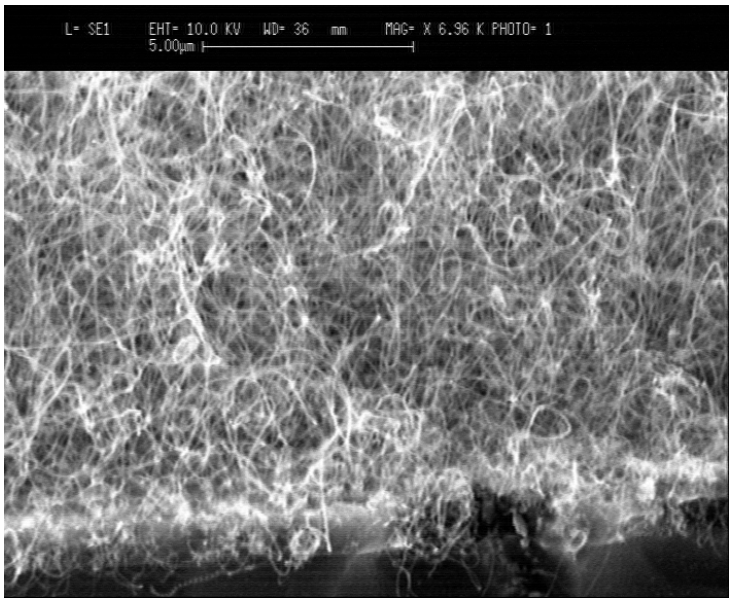

Fig. 14. SEM image of a randomly oriented CNTs sample grown on SiO_2 at about 800°C, C_2H_2 flux of 75 sccm, and P_{ch} ~ 12 Torr. The image have been obtained tilting the sample stage of 60°.

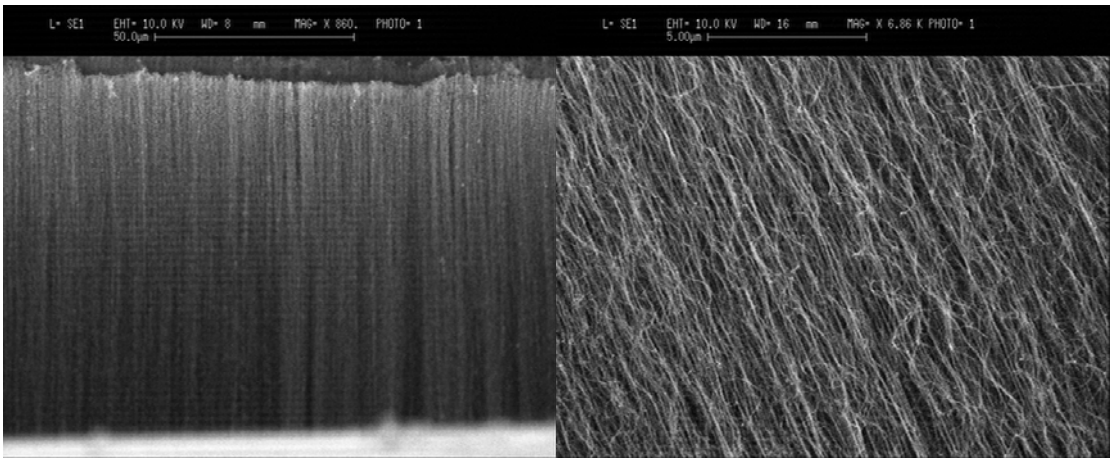

Fig. 15. SEM images of aligned CNTs sample grown on SiO_2 at about 800°C, C_2H_2 flux of 200 sccm, and P_{ch} ~ 50 Torr . The image have been obtained tilting the sample stage of 90°. The CNTs show to have a very high orientation tendency being mostly oriented perpendicularly to the substrate.

Cambridge StereoScan 360 apparatus is able to perform analysis down to a 30 nm resolution (in Fig. 16 a micrograph of ~ 53 K of magnification is shown). To characterize the structure of single CNTs (number of walls, defects, impurities, etc.) SEM investigations are not sufficient. It is necessary to perform Transmission Electron Microscopy (TEM) measurements in order to increase the resolution to almost 0.1 nm and achieve a complete morphological characterization.

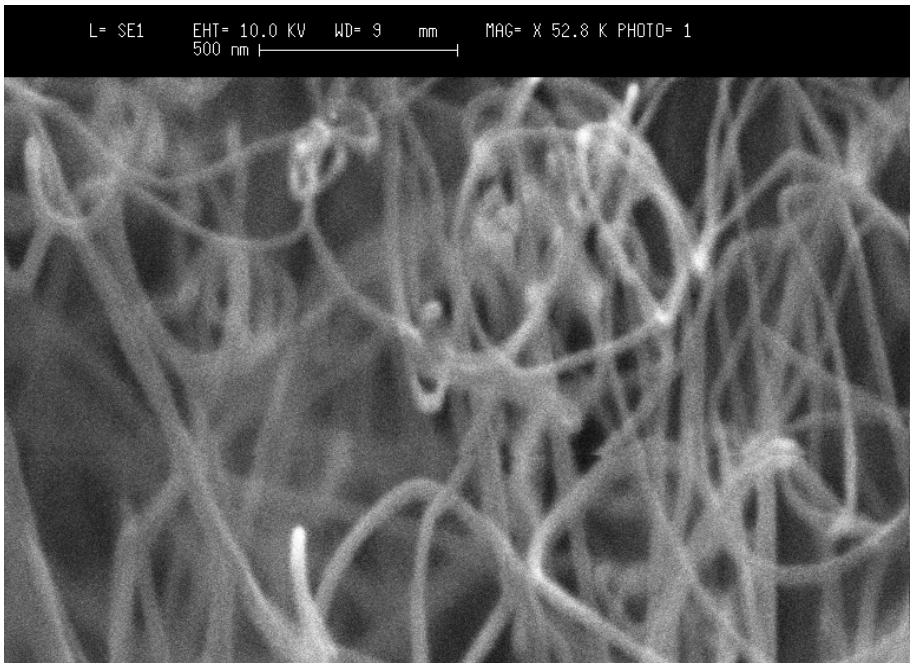

Fig. 16. Micrograph on a MWCNs sample recorded at about X 52k of magnification.

3.3.4 Morphology and structure: TEM characterization

TEM measurements have been performed at ISPESL (National Institute for Occupational Safety and Prevention) in a FEI TECNAI 12 (120 keV) apparatus equipped with an energy filter (GATAN GIF model) and a Peltier-cooled SSCD (slow scan charged-coupled device) multiscan camera (794IR model). A droplet of the raw synthesis diluted in isopropyl was used to disperse the nanotubes on a typical gold TEM grid (mesh 1000). In such a way, most of the synthesis products are located next to or bridged between two gold wires and the TEM system can detect the presence of free-standing bundles of nanotubes (Fig. 17)

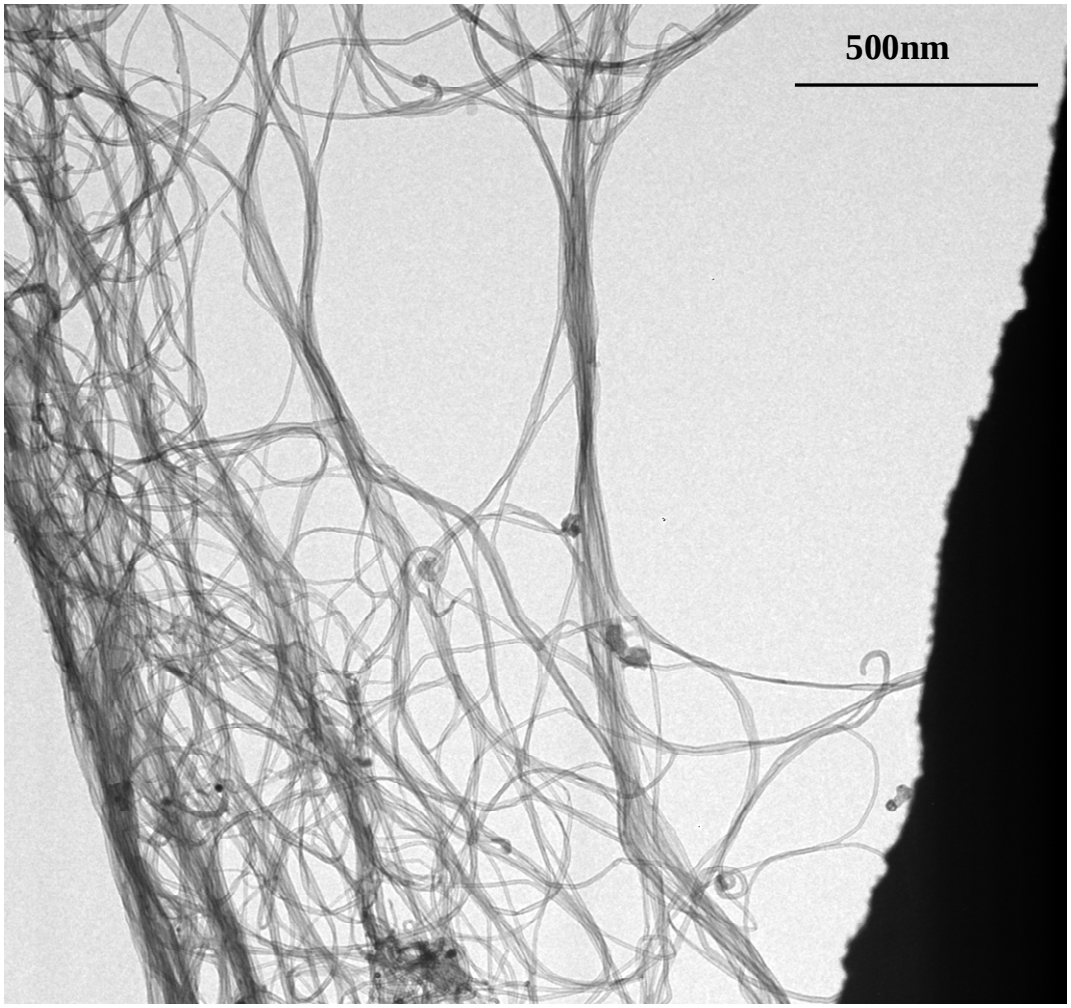

Fig. 17. TEM image of free-standing bundles of CNTs connecting two gold wires. Images taken in the ISPESL laboratory.

TEM images allow to experimentally verify if CNTs are SW or MW, identify the growth model (if Extrusion or Tip growth), detect the presence of impurities (i.e. other carbonaceous products, amorphous or crystalline on the external walls, or catalyst nanoparticles), detect the NT's defects (closing of inner channel, breaking off one or more walls, presence of bamboo-like NT, deviation from the cylindrical form, etc.), and finally to measure the number of walls and the diameter size (inner and outer). In Fig. 18 miscellaneous TEM images are shown.

The TEM analysys reveal that a large part of the synthesised CNTs show a good crystallinity, a good straight direction, and absence of carbonaceous synthesis product.

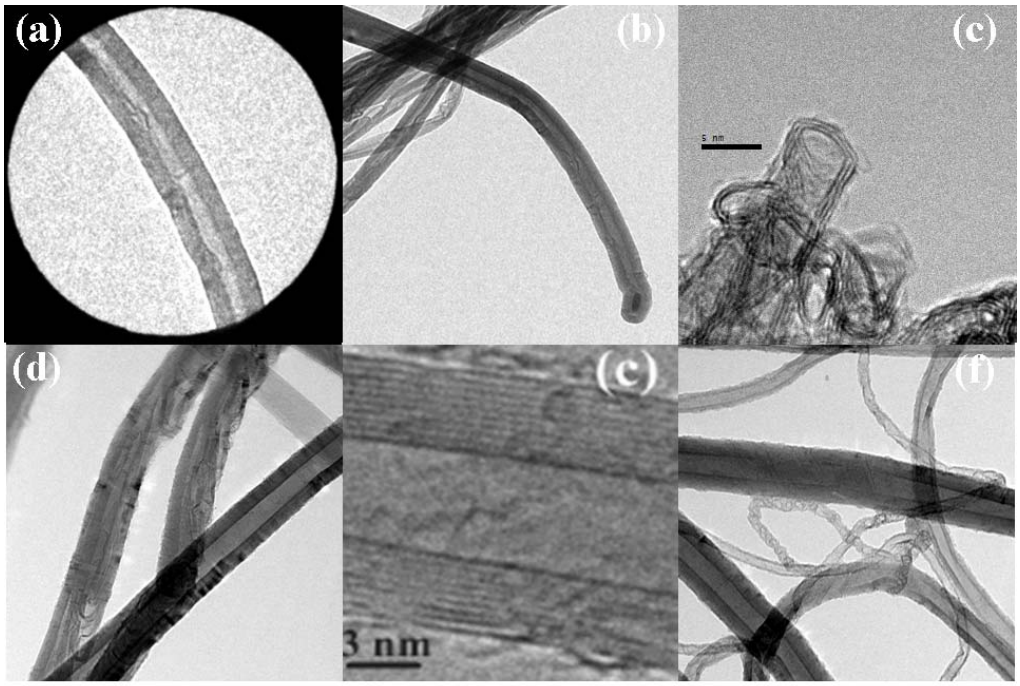

Fig. 18. Some TEM images particular of nanotubes. (a) identification of the kind of CNT, MWNT vs SWNT. Two images showing the kind of model growth: (b) the catalyst nanoparticle capped by nanotube, tip growth and (c) uncapped nanotube, extrusion growth. (d) NT's defects: presence of bamboo-like CNT. (e) MWNT particular: it is possible to distinguish the in-plane distance of the layers (f) presence of other carbonaceous product;

To obtain deeper information about the crystallinity of the deposited nanotubes, Electron Energy Loss Spectroscopy (EELS) measurements have been performed in the TEM apparatus. EELS concerns the analysis of energy spreading of initially almost monoenergetic electrons, after their interaction with the sample. The technique is frequently used in association with Transmission Electron Microscopy (TEM) and interaction takes place inside the specimen. Measuring the energy distribution of electrons that have passed through a thin specimen, it is possible to obtain information about its structure. The electrons impinging on the sample may lose energy by a variety of mechanisms. These losses can reveal the composition of the sample in TEM. At high energy loss, ionization edges occur due to inelastic excitation of inner-shell (*core*) electrons. The threshold energy of each edge is the binding energy of the corresponding atomic shell and is tabulated for all elements and electron shells (K, L, M, etc.). A more detailed description of the EELS Spectroscopy is reported in the Appendix C.

EELS spectra at high energy loss were collected using a primary electron beam of 80 keV [2]. Fig. 20 shows EELS spectra recorded at the Carbon K edge for: an amorphous carbon sample, a highly oriented pyrolitic graphite (HOPG) and a MWNT isolated among a free-standing bundle of nanotubes, as shown in Fig 19 and its inset. In the spectrum of graphite the sharp peak near 286 eV is due to a transition from the 1s core level to the π^* band, and the structures in the 293–340 eV range are due to transitions from the C1s core level towards unoccupied density of states (σ^* and π^*), in agreement with conduction band calculations [25] and experimental findings [26-29].

While the absorption spectrum of amorphous samples shows σ^* profiles broader and structureless located around ~300 eV, outlining that the film is poorly structured and predominantly amorphous [30-31].

On the contrary the MWNT absorption spectrum strictly resembles the graphite spectrum. This implies MWNT has a very high crystalline quality and the nature and local order of chemical bonds are similar to those of graphite.

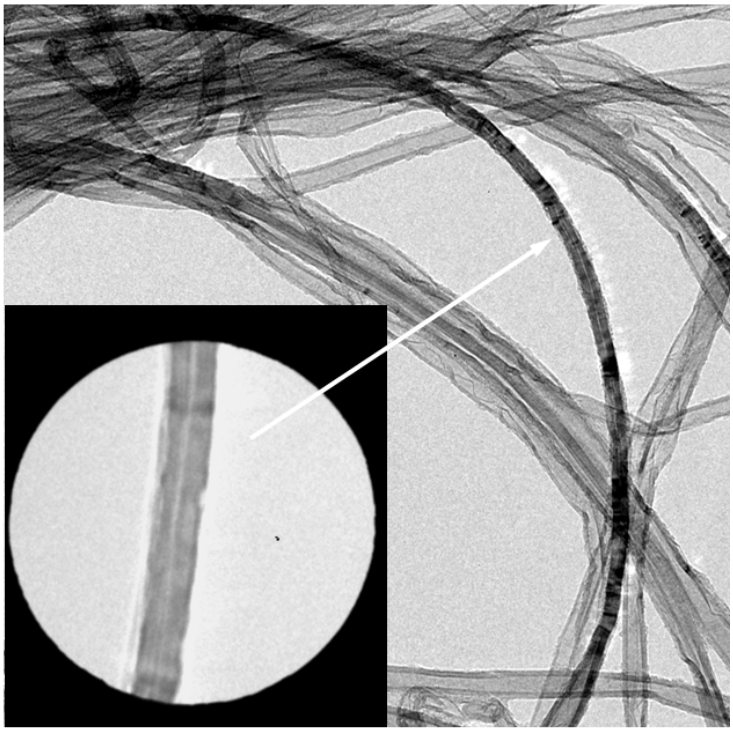

Fig. 19. Free-standing bundle of carbon nanotubes. The naotubes show very high quality. At this resolution, no presence of carbonaceous products, no evident structurally defect (bamboo-like structure for example), good straightness. In the inset the higher resolution image of an

[2] It is worth to underline that TEM images were acquired before and after each electron energy loss measurements to check if the studied free-standing nano-system had suffered morphological changes, had moved or broken as a consequence of its exposure to the high energetic electron beam.

isolated nanotube whose structure has been investigated by energy loss spectroscopy (see Fig. 20).

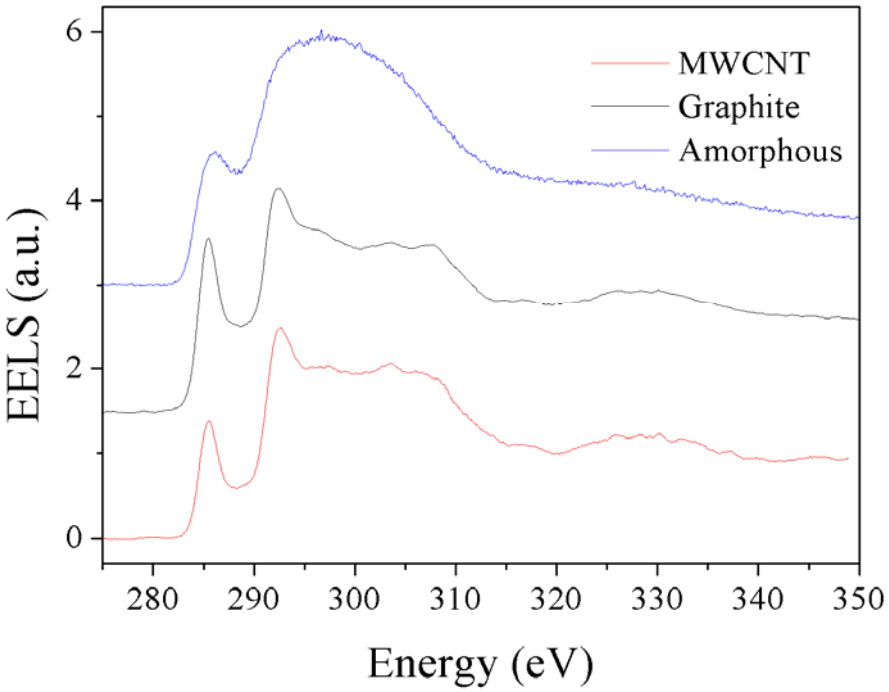

Fig. 20. Electron Energy loss spectrum at Carbon K edge of the single multiwall carbon nanotube of Fig. 19 compared the spectra of an amorphous carbon sample, and a highly oriented pyrolitic graphite (HOPG). The absorption spectrum of graphite the sharp peak near 286 eV is due to a transition from the 1s core level to the π* band, and the structures in the 293–340 eV range are due to transitions from the C1s core level towards unoccupied density of states (σ* and π*). The MWNT absorption spectrum strictly resemble the graphite one. This implies MWNT has a very high crystallinity quality and the nature and local order of chemical bonds are almost equal to that of graphite.

Analyzing high resolution images it is possible to measure CNT structural characteristics as the size of nanotube, the diameter of the inner channel, the number of walls and their reciprocal distance. In Fig. 21 an high resolution image is reported in addition to the profile, namely the number of transmitted electrons vs distances corresponding to the rectangle indicated in the HTEM image.

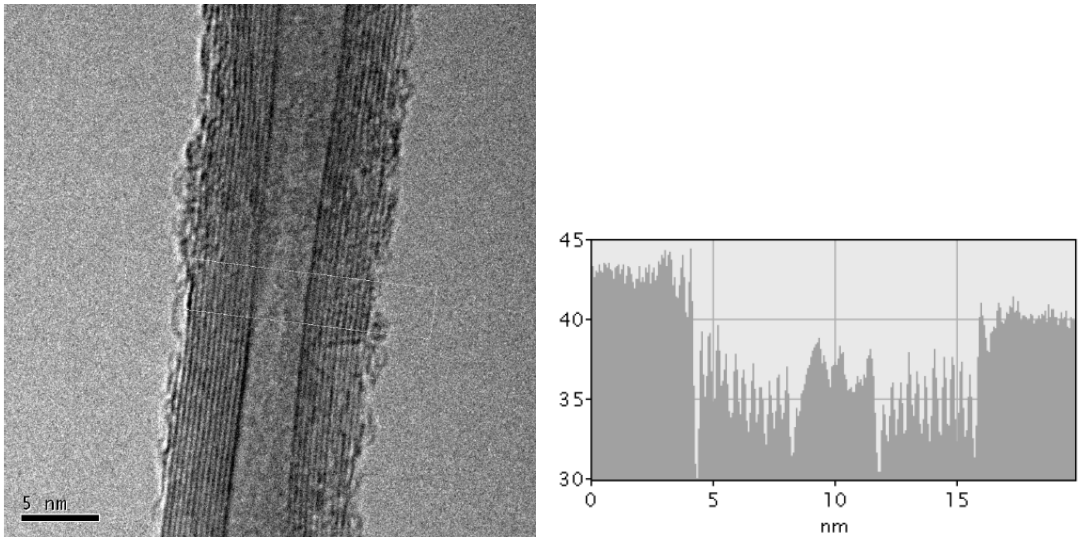

Fig. 21. Left: high resolution TEM micrograph of a MWCNT. Right: transmission profile relative to the rectangle shown in the micrograph (number of transmitted electrons as a function of the distances).

To obtain the size distribution of MWCNTs, different TEM micrographs with standard resoltuion have been acquired (see Fig.22). By means of an image elaboration software, the length of external and internal channel of many NTs have been evaluated. The images have to hold a number of NT able to give a significant statistics, moreover NTs have to be well dispersed to allow an easy measurement of diameters avoiding count repetitions of an already analyzed NT. Usually, taking into account from 4 to 10 micrographs, a number of 60 ÷ 80 MWCNTs are measured.

To give an example of the methodology by which the size distributions of MWCNT synthesised, it is reported the statistical data related to the external and internal diameters and to the number of walls for the sample "160908". This is a sample of NT grown on a SIO_2 (300 nm on Si <100>) substrate covered by 1nm of iron (growth time 10 min, C_2H_2 flux of 200 sccm, chamber pressure 12.0 ± 0.2 Torr).

The values reported in Table 2 have been obtained reporting on histograms the counts in an interval of 1nm for the diameters and of 1 unit for the number of walls. Then, a fit with a suitable number of Gaussian curves is performed (see Fig. 23). The maximum position of the Gaussian corresponds to the values of diameters (number of walls), their relative errors correspond to one sigma and the relative percentage have been obtained imposing that the sum of the integral areas of the Gaussian curves is 100.

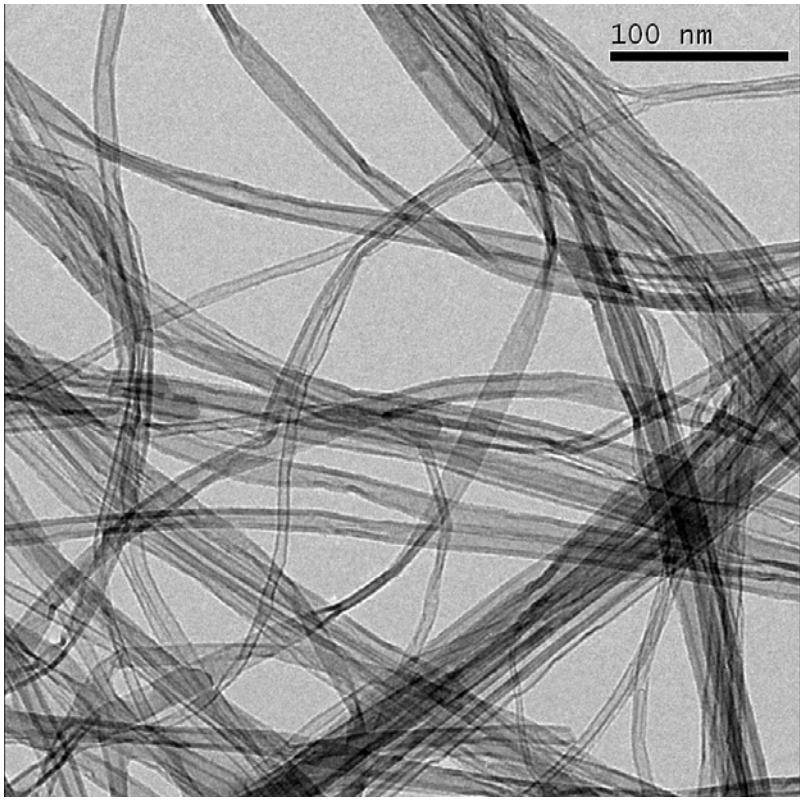

Fig. 22. Standard resolution TEM images for statistical analysis of structural MWCNT parameters. In particular, this image refers to sample "160908".

External channel (nm)	%	Internal channel (nm)	%	# walls	%
4.0 ±2.3	74%	7.9 ±2.2	33%	5.0 ± 1.0	9%
7.1 ± 2.4	26%	11.5 ±2.2	37%	8.0 ±1.0	29%
		14.5±1.7	23%	9.0 ±2.0	41%
		17.2±4.1	7%	13.0±2.0	21%

Table 2. Value of the structural parameters (in percentage): external and internal channel, and number of wall for the sample "160908". The structural data have been obtained performing a statistical analysis on 60 MWCNTs examined under TEM. For each nanotube, the parameter values have been measured by means of an image elaboration software on TEM micrographs at suitable resolution (see Fig 22).

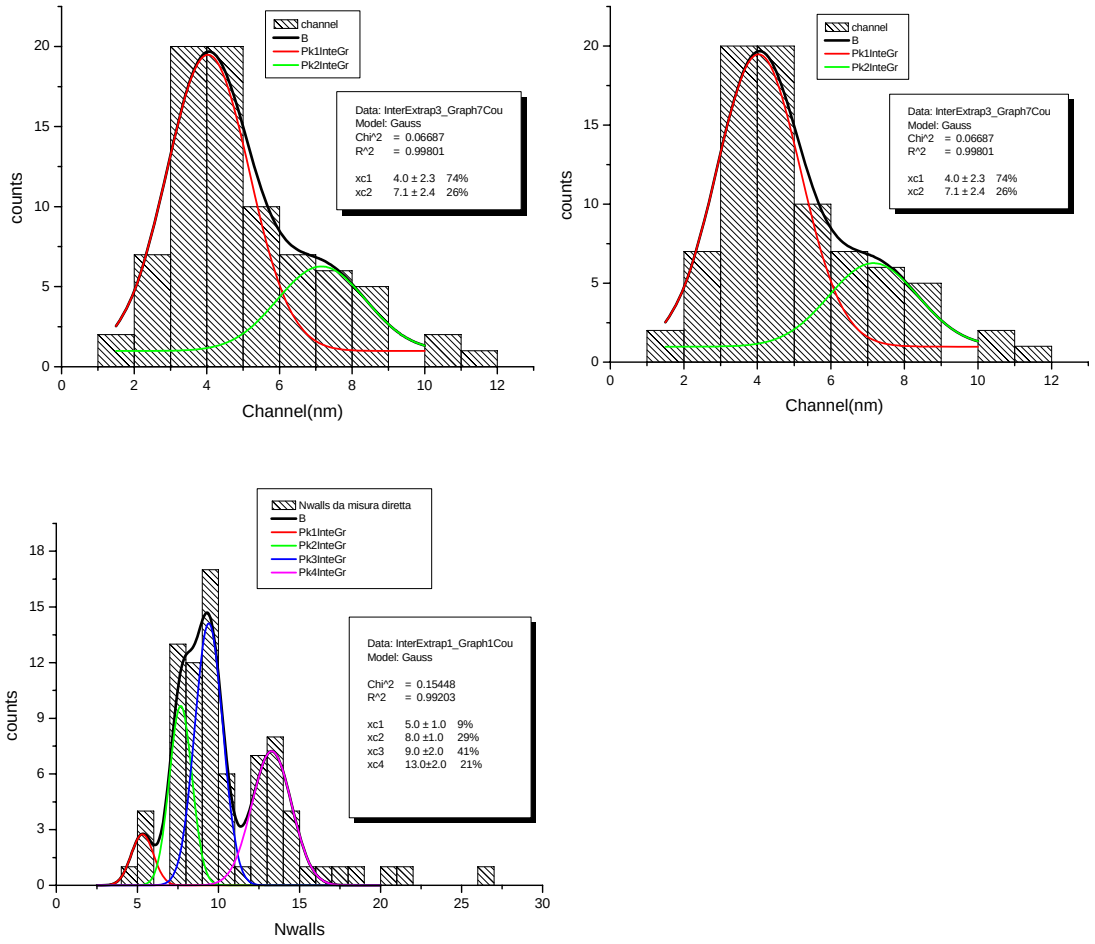

Fig. 23. Histograms of external/internal diameter and of the number of wall for the MWNTs sample "160908". A fit with a suitable number of Gaussian curves is performed to obtain the percentage of the different parameters. The positions of maximum of the Gaussian corresponds to the values of diameters (number of walls), their relative errors correspond to one sigma and the relative percentage have been obtained imposing that the sum of the subtended areas of the Gaussian curves is 100.

3.4 Decoration of MWCNT

After the growth of MWCNTs on SiO_2, Cu has been deposited *in-situ* by thermal evaporation from a Cu rod held by a tungsten crucible, in the growth chamber at a base pressure of $1x10^{-8}$ Torr. The W crucible is housed close to the catalyst one and the nominal Cu thickness has been estimated with the quartz microbalance depicted in Fig. 10. Samples with a nominal Cu deposited layer of (0.10 ± 0.01) nm thickness have been deposited[3]. In the following, a sample of this set will be named "SiO_2/MWCNT/Cu" and compared to a sample grown in the same experimental parameters excluding the Cu deposition, whose name is "SiO_2/MWCNT".

SEM and TEM measurements characterize the morphology, purity and the internal structure of the carbon nanotubes. SEM images obtained on both MWNTs and Cu-MWCNTs show the nanotubes distributed homogeneously on the substrate without showing a preferential orientation with respect to the substrate (Fig.24). The best SEM spatial resolution is insufficient to clearly identify the presence of Cu on the nanotube surface. This task has been accomplished by TEM analysis, as shown in Fig. 25. The Cu nanoparticles have been found to be randomly distributed on the outer walls of the nanotube as isolated or agglomerated (Fig. 25(a)). A high-resolution TEM micrograph obtained on a single MWCNT decorated with the nanoparticles is shown in Fig. 25(b). Focusing the CNT walls, Fig. 25(b) reveals that their 'graphitic-like' disposition is preserved after the decoration with Cu. The Cu particles frequently have a faceted shape with an average diameter of about (6.0 ± 1.0) nm.

[3]Different thicknesses have been deposited, from 0.1 to 0.5 nm. Here only the Cu decoration thickness of 0.1 nm is discussed because, until now, the photocurrent generation properties have been investigated only for these samples.

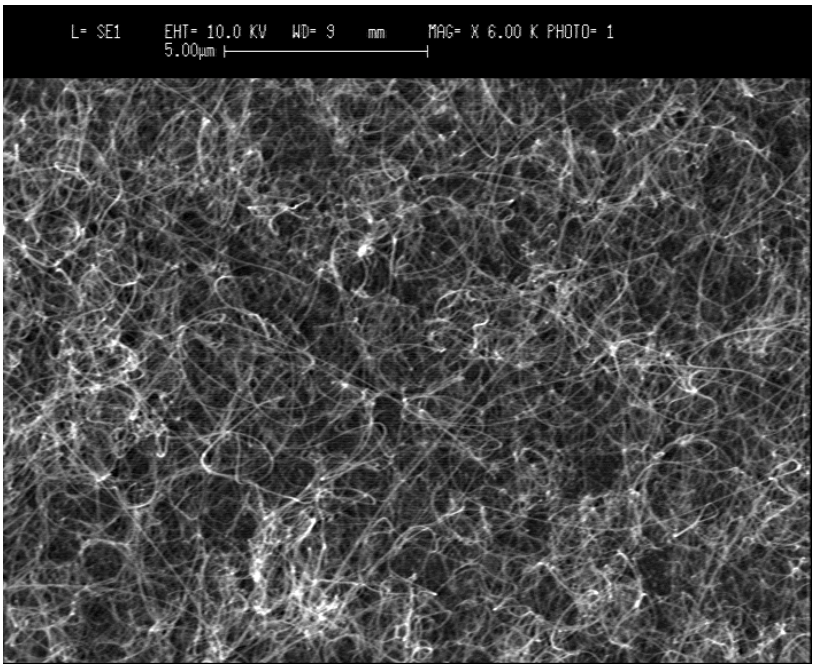

Fig. 24. SEM image obtained from MWCNT after Cu deposition (sample "SiO_2/MWCNT/Cu")

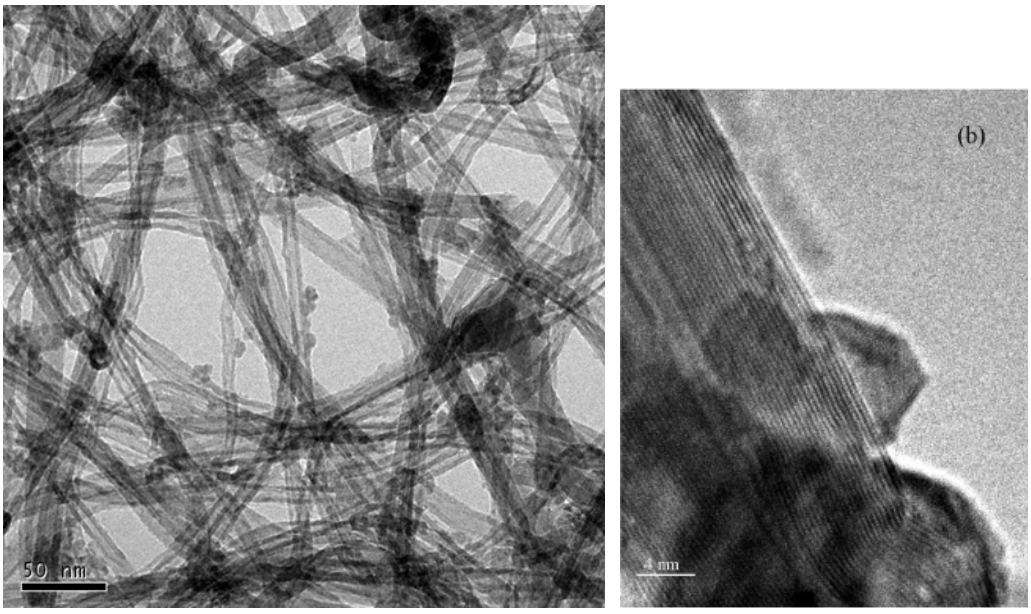

Fig. 25. a) TEM image of the Cu-MWCNT; Cu nanoparticles are randomly distributed on the outer walls of the nanotube as isolated or agglomerated. b) TEM micrograph obtained on a single MWCNT decorated with the nanoparticles.

To deeper investigate the kind of Cu–MWCNT interaction, X-ray photoelectron spectroscopy has been applied. X-ray photoelectron spectra have been collected from the MWCNTs before and after Cu nanoparticle deposition. The data have been measured with a semi-imaging analyser MAC 2 (Riber Instruments) operating in the constant pass energy mode (with a total energy resolution of 1.0 eV), using a non-

monochromatized Mg K_α (1253.6 eV) radiation source (9 kV, 700 W). The distance between the sample and the anode has been set to about 40mm, the illumination area to about 5x5 mm^2 and the takeoff angle between the sample surface and the photoelectron energy analyser has been held fixed to 45°. The energy scale with reference to the binding energy of the C1s has been calibrated at 284.7eV with respect to the Fermi level. Extended energy distribution spectra have been first recorded, followed by high resolution scans over Cu 2p photoelectron binding energy region. XPS spectra have been analysed using a standard Gaussian curve fit routine with a Shirley background subtraction [32]; the quality of the fit has been evaluated by using χ^2 minimization test.

The XPS studies have been performed to characterize the electronic properties of the Cu nanoparticles deposited on the nanotube walls. Fig. 26 reports the line spectrum of the Cu 2p core levels. A nonlinear curve fitting of the observed intensities outline two main features corresponding to the Cu $2p_{3/2}$ and Cu $2p_{1/2}$ binding energies respectively, while the energy difference between the reported energies is about 20 eV [33]. From this spectrum, it seems that the formation of

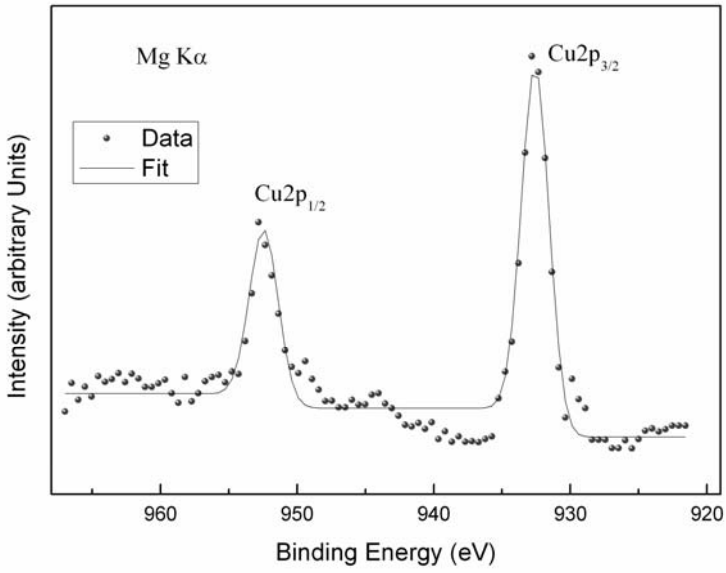

Fig. 26. XPS (Mg K_α, hν=1253.6 eV) Cu 2p core level spectrum obtained on MWCNT after Cu deposition. Full circles are experimental data (•), solid line is the fitting curve obtained summing up the gaussian components computed by a nonlinear curve fit procedure.

Several TEM micrographs identifying free-standing nanotubes have been collected both for the Cu-MWCNT and the MWCNT samples to obtain the structural parameters distributions, according to the procedure described in the last part of

paragraph 3.3.4. The results of the statistical analysis are reported in Table 3. As expected, the MWCNTs of the two samples show very similar structure properties. It makes sense to compare their physical properties to investigate the role of Cu nanoparticles.

Sample	External channel (nm)	Internal channel	N. of walls
SiO_2/MWCNT	7,6 ± 1,7 (50%) 10,8 ± 3,0 (44%) 15,4 ± 1,5 (6%)	4,0 ± 1,0 (37%) 4,9 ± 3,3 (63%)	5 ± 1 (23%) 7 ± 1 (35%) 9 ± 4 (42%)
SiO_2/MWCNT/Cu	7,9 ± 2,2 (33%) 11,5 ± 2,2 (37%) 14,5 ± 1,7 (30%)	4,0 ± 2,3 (74%) 7,1 ± 2,4 (26%)	5 ± 1 (25%) 8 ± 1 (29%) 9 ± 2 (46%)

Table 3. Structural parameters distribution for two samples of MWCNTs grown in the same experimental parameters. On the second one, Cu has been deposited.

3.5 Deposition on patterned substrates

In this paragraph the selective deposition of MWCNTs on patterned substrates will be presented. This activity, in collaboration with the "Roma Tre" University, Dept. of Physics, started as part of the PRIN 2005 project "*Carbon nanotubes based electronic and optoelectronic devices*" (Coord. Prof. De Crescenzi), funded by the Ministry of Education, University and Research. The specific goal of this research activity was the measurement of the transport electronic properties of single MWCNTs, by growing a single MWNT directly between two electrodes. After discarding the use of metallic electrodes, it has been chosen to grow MWNTs on degenerately doped Si films acting as electrodes. To verify the effectiveness of the strategy and to define the manufacturing parameters of the structures, preliminary mesa realization tests and localised MWCNTs growth have been performed on SOI substrates (Silicon On Insulator). The mesa on SOI can operate as interconnection platform for MWCNTs and as electrode at room temperature.

The used lithographic mask is composed by a series of mesas characterized by a square and rectangular shape of size from 0.5 μm to 6 μm and variable distances from 7 μm to 0.4 μm (Fig. 27). This mask is then repeated several times on substrate.

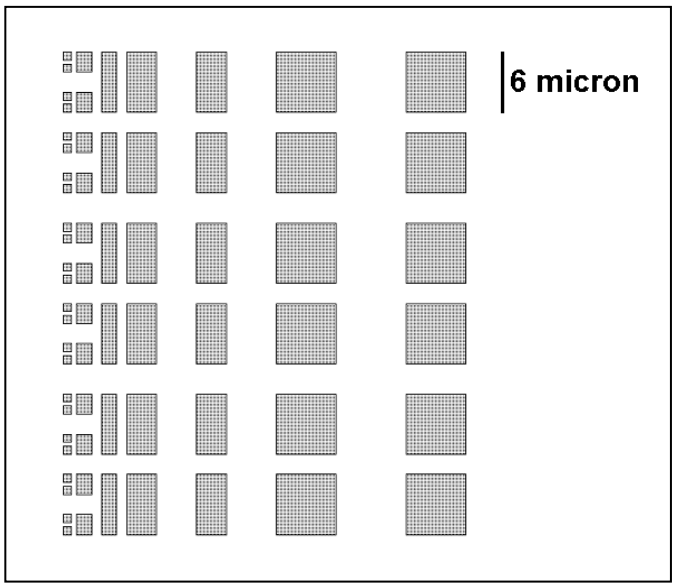

Fig. 27. Lithographic mask for the mesa pattern.

The mesas have been realized by Dr. Notargiacomo by means of electron beam lithography, starting from a SOI substrate constituted by a Si layer of 200 nm on a 200 nm thick SiO_2 layer (Fig. 28 (a)). At the end of the process, they result as structures built directly on the insulator (Fig. 28(b) and SEM image inside). To deposit the Fe catalyst only onto the mesa, another lithographic process has been performed to obtain aperture into the resist[4] in correspondence to the mesa (Fig. 28(c)). At this point the substrate is introduced in the CVD chamber to deposit 1 nm (nominal thickness) Fe layer (Fig. 28(d)). Then the sample is taken out to remove the PMMA in acetone. In this way also the Fe is lifted-off, except onto the mesa where the PMMA has been absent. The substrate is reintroduced in the chamber to grow MWCNTs (Fig. 28(e)). To test the process of PMMA windows opening and surface cleaning, the SEM images of the first sample synthesised are reported in Fig. 29. It is evident that the MWCNTs nucleation sites are localised on the mesa surfaces where the catalyst is present.

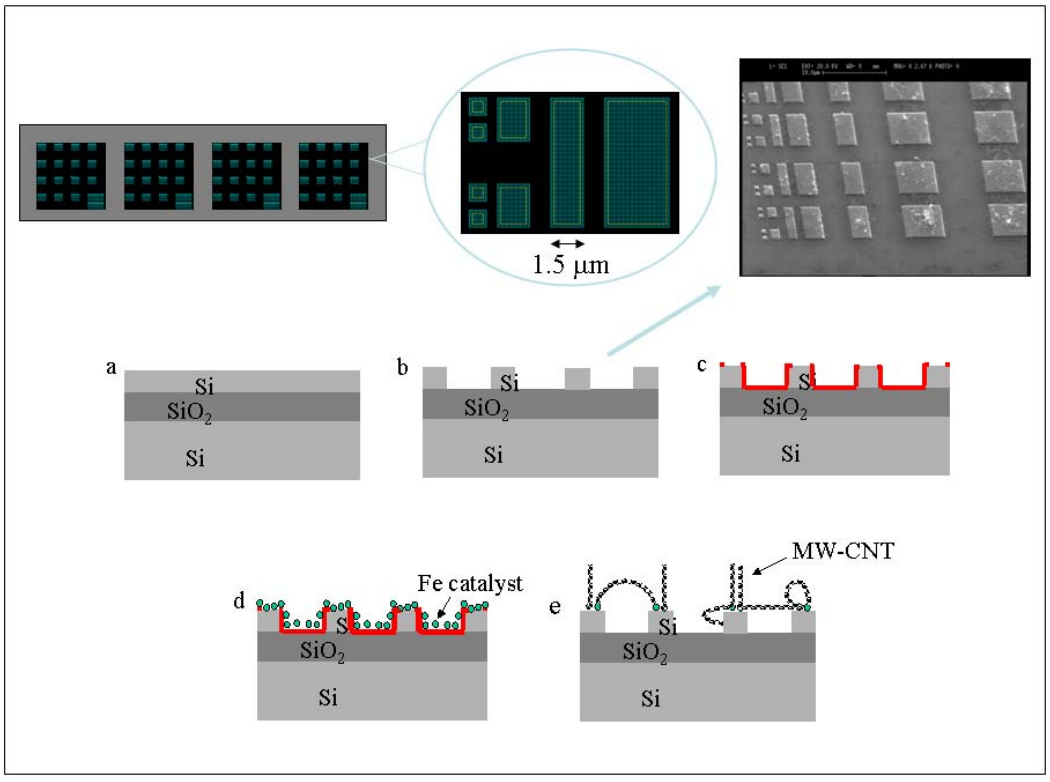

Fig. 28. Scheme of the process to obtain a selective deposition of MWCNTs on patterned substrates. On top, particular of the lithographic drawing for the mesa realization. From (a) to (e) different phases: (a) SOI substate, (b) Si mesa "built " on oxide, (c) the resist film with the opening in correspondence to the mesa, (d) Fe is evaporated on the substrate surface, (e)

[4] The used resist is Poly-(methyl-methacrylate), PMMA.

nanotubes nucleate only on the mesa surface due to the PMMA removal first of MWCNTs synthesis.

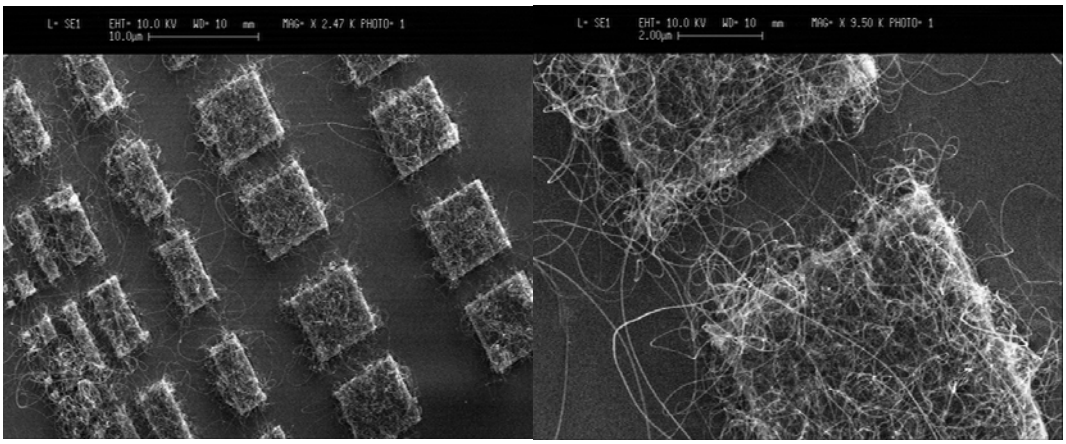

Fig. 29. First results of the MWCNTs selective deposition following the procedure described in Fig. 28.

In some structures, MWCNTs connect various mesas, demonstrating the capability of this methodology to localize single nanotube between built electrodes. However, the density of MWCNTs is still too high. Their length is too high, their distribution too disordered for measuring single MWCNT transport properties. Therefore different samples have been synthesised changing the experimental parameters. Finally a sample satisfying the initial requests has been obtained, in which isolated nanotubes connect the neighbouring mesa. Two of these nanotube are shown in Fig. 30.

The final fabrication of mesas made of degenerately doped Si and the relative electronic measurements are currently going to be performed in collaboration with "Roma Tre".

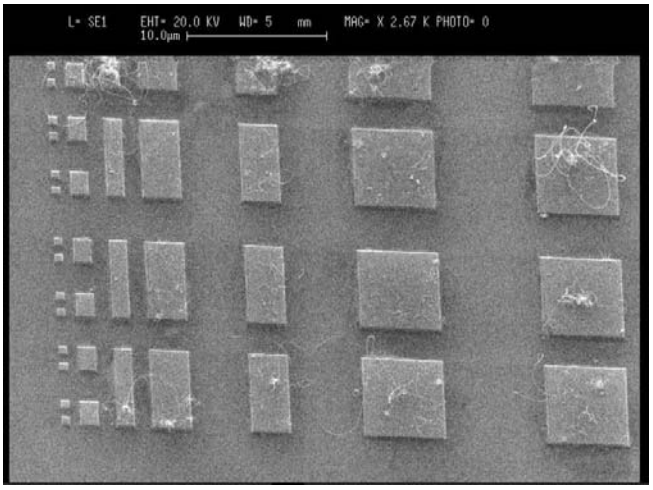

a)

b)

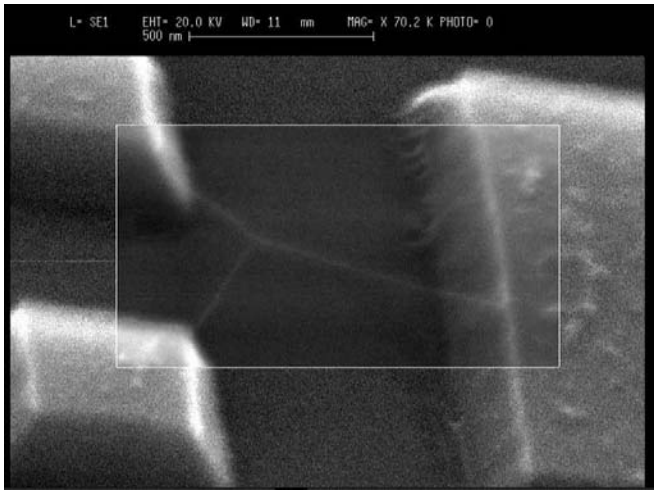

c)

Fig. 30. Best results of MWCNTs selective deposition for transport measurements. The density of MWCNTs is low (a) and many of them connect neighbouring mesa (b) and (c).

Finally, the peculiar results of another sample of MWCNTs on mesas is illustrated in the following. Increasing the hydrocarbon flux rate and the chamber pressure, a very high density of long MWCNTs is obtained resulting in a self-oriented close

packed nanotubes (Fig. 31). This sample has been obviously discarded due to the too high nanotube density on each mesa and their 3D orientation, incompatible for the foreseen kind of measurements, and to the bad removal of PMMA that allowed nanotubes to grow outside mesas, onto SiO_2. Notwithstanding this is very intriguing for building 3D architectures which can be used for specific applications, such as very high localized field emitters, or THz and IR detectors (exploiting antenna effects [34]).

In regards to the synthesis, other activity has to be carried on to fix the growth parameters in order to control the final architecture of MWCNTs, as a function of the specific application.

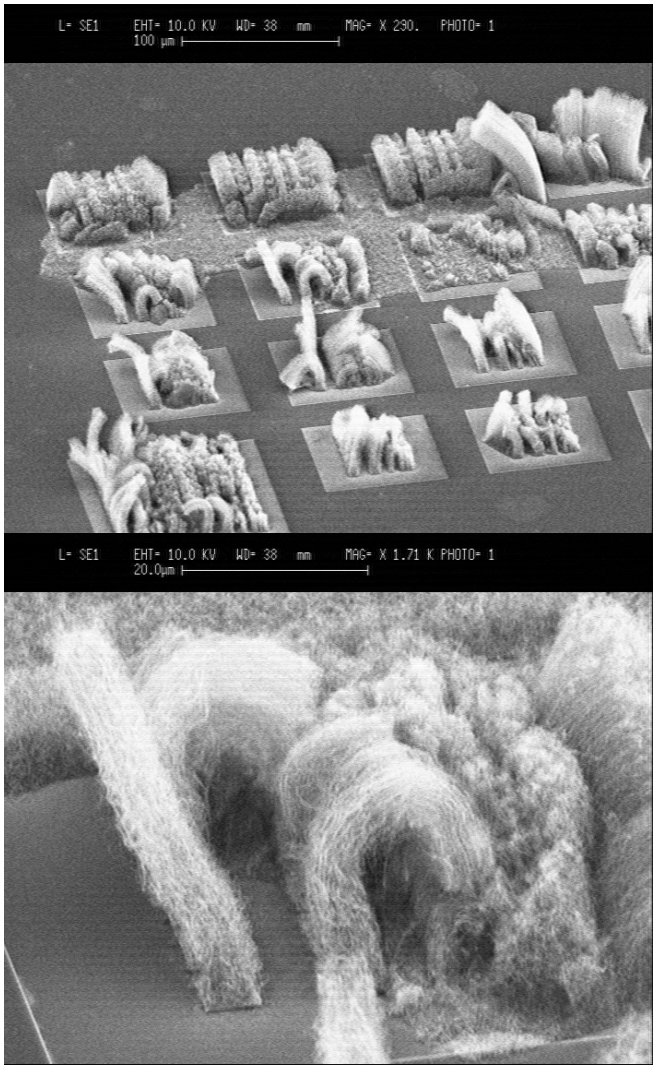

Fig. 31. SEM images of a particular sample of nanotubes on a mesa. The PMMA removal is not compelted and nanotubes are allowed to growth on oxide (top image). The density of long MWCNTs on silicon mesa is very high resulting in a self oriented close packed nanotubes.

References

[1] Y.Saito, *Carbon* **38**, 169 (2000).

[2] S. Iijima, *Nature* **354**, 56 (1991)

[3] T. W. Ebbesen and T. M. Ajayan, *Nature* **358**, 220 (1992).

[4] S. Iijima and T. Ichibashi, *Nature* **363**, 603 (1993).

[5] D. S. Bethune, C. H. Kiang, M. S. Devries, G. Gorman, R. Savoy, J. Vazquez, and R. Beyers, *Nature* **363**, 605 (1993).

[6] A. Thess, R. Lee, P. Nikolaev, H. J. Dai, P. Petit, J. Robert, C. H. Xu, Y. H. Lee, S. G. Kim, A. G. Rinzler, D. T. Colbert, G. E. Scuseria, D. Tomanek, J. E. Fischer, and R. E. Smalley, *Science* **273**, 483 (1996).

[7] J. Liu, A. G. Rinzler, H. Dai, J. H. Hafner, R. K. Bradley, P. J. Boul, A. Lu, T. Iverson, K. Shelimov, C. B. Huffman, F. Rodriguez-Macias, Y.-S. Shon, T. R. Lee, D. T. Colbert, R. E. Smalley, *Science* **280**, 1253 (1998)

[8] Z. F. Ren, Z. P. Huang, J. W. Xu, J. H. Wang, P. Bush, M. P. Siegel, and P. N. Provencio, *Science* **282**, 5391 (1998)

[9] S. Fan, M. Chapline, N. Franklin, T. Tombler, A. Cassell, H. Dai, *Science* **283**, 512 (1999)

[10] A. Cassell, N. Franklin, T. Tombler, E. Chan, J. Han, H. Dai, *J. Am. Chem. Soc.* **121**, 7975 (1999)

[11] H. Kind, J.-M. Bonard, C. Emmenegger, L.-O. Nilsson, K. Hernadi, E. Maillard-Schaller, L. Schlapbach, L. Forro and K. Kern, *Adv. Mater.* **11**, 1285 (1999).

[12] Z. F Ren, Z. P. Huang, D. Z. Wang, J. G. Wen, J. W. Xu, J. H. Wang, L. E. Calvet, J. Chen, J. F. Klemic, M. A. Reed, *App. Phys. Lett.* **75**, 8, 1999

[13] S. B. Sinnot, R. Andrews, D. Qian, A. M. Rao, Z. Mao, E. C. Dickey, F. Derbyshire, *Chem. Phys. Lett.*, **315**, 25 (1999)

[14] M. Yudasaka, R. Kikuchi, T. Matsui, Y. Ohki, S. Yoshimura, E. Ota, *App. Phys. Lett.* **67**, 2477 (1995).

[15] M. Yudasaka, R. Kikuchi, Y. Ohki, E. Ota, S. Yoshimura, *App. Phys. Lett.* **70**, 1817 (1997).

[16] A. Yasuda, N. Kawase, W. Mizutani, *J. Phys. Chem. B*, **106**, 51 (2002).

[17] M. Endo and H.W. Kroto, *J. Phys. Chem.* **96**, 6941 (1992).

[18] R. Saito, M. Fujita, G. Dresselhaus, and M.S. Dresselhaus, *Mater. Sci. Eng. B* **19**, 185 (1993).

[19] R.E. Smalley, *Mater. Sci. Eng. B* **19**, 1 (1993).

[20] S. Iijima, T. Ichihashi, and Y. Ando, *Nature* **356**, 776 (1992).

[21] S. Hofmann et al, *Nano Letters* **7**, 602 (2007).

[22] Y. Wang, K, Kempa, B. Kimball, B. Carlson, G. Benham, W.Z. Li, T. Kempa, J. Rybczynski, A. Herczynski, and Z.F. Ren, *Appl. Phys. Lett.* **85**, 2607 (2004)

[23] Y.J. Jung, Y. Homma, T. Ogino, Y. Kobayashi, D. Takagi, B. Wei, R. Vajtai, P.M. Ajayan, *J. Phys. Chem. B* **107**, 6859 (2003).

[24] [Homma_a]Y. Homma, Y. Kobayashi, T. Ogino, D. Takagi, R. Ito, Y. J. Jung, P. M. Ajayan, *J. Phys. Chem. B* **107**, 12161 (2003)

[25] R.F. Willis, B. Fitton, G.S. Painter, *Phys. Rev. B* **9**, 1926 (1974).

[26] B.M. Kincaid, A.E. Meixner, P.M. Platzman, *Phys. Rev. Lett.* **40**, 1296 (1978).

[27] R. Gunnella, I. Davoli, R. Bernardini, M. De Crescenzi, *Phys. Rev. B* **52**, 17091 (1995).

[28] D. Denley, P. Perfetti, R.S. Williams, D.A. Shirley, J. Stöhr, *Phys. Rev. B* **21**, 2267 (1980).

[29] R.A. Rosenberg, P.J. Love, Victor Rehn, *Phys. Rev. B* **33**, 4034(1986).

[30] G. Comelli, J. Stfhr, C.J. Robinson, W. Jark, *Phys. Rev. B* **38**, 7511 (1988).

[31] C. Lenardi, P. Piseri, V. Briois, C.E. Bottani, A. Li Bassi, P. Milani, *J. Appl. Phys.* **85**, 7159 (1999).

[32] D.A. Shirley, *Phys. Rev. B* **5**, 4709 (1972).

[33] J. F. Moulder, W. F. Stickle, P. E. Sobol, '*Handbook of X-Ray Photoelectron Spectroscopy'*, Perkin- Elmer, Physical Electronics Division (1993).

[34] Y. Wang, K, Kempa, B. Kimball, B. Carlson, G. Benham, W.Z. Li, T. Kempa, J. Rybczynski, A. Herczynski and Z.F. Ren, *Appl. Phys. Lett.* **85**, 2607 (2004)

Chapter 4

Photocurrent generation in MWCNTs

The experimental study described in the present Chapter examines and develops the results obtained on MWCNTs photocurrent generation inside chemical cells performed by De Crescenzi's group at Department of Physics, University of Rome "Tor Vergata", and reported in refs. [1] and [2]. In this Thesis further experiments on different MWCNTs based devices will be presented. Their optoelectronic properties will be tested and the photocurrent generation mechanisms will be investigated. A rational of the photoresponse as a function of the incident photon energy will be supported by ab-initio calculations of density of states (DOS) in agreement with the experimental findings. The effect of metal decoration will be further investigated.

4.1 Introduction

The parameter that takes into account the conversion efficiency of a sample is the Incident Photon-to-Current Efficiency (*IPCE*) or Quantum Efficiency (*QE*). It reveals how good is a specific materials/device to convert a radiation length into electricity[5]. The *IPCE* is the number of charges collected, N_{ch}, per incident photons, N_e:

1 $$IPCE = \frac{N_{ch}}{N_{ph}}$$

It is evaluated from short circuit photocurrent (I_{sc}) measurements under different incident radiation wavelengths (λ), taking into account the following equations:

2 $$\begin{aligned} P_{lamp}(Watt) &= \frac{N_{ph} \cdot h\upsilon}{\sec} = \frac{N_{ph}}{\sec} \cdot \frac{hc}{\lambda}(Joule/\mathrm{s}) \\ I_{sc}(A) &= \frac{N_{ch} \cdot q}{\sec}(Coul/\mathrm{s}) \end{aligned} ,$$

where P_{Lamp} is the power of the incident light and q the elementary charge. Normalizing Eq.s 2 to the illuminated area A, the *IPCE* become:

3 $$IPCE = \frac{(I_{sc}/A)\cdot \sec}{q \cdot \left(P_{lamp}/A\right) \cdot \sec / \left(h\frac{c}{\lambda}\right)} = \frac{I_{sc}}{P_{Lamp} \cdot \lambda} \cdot \frac{hc}{q}$$

4.2 Photoelectrochemical MWCNT Properties

4.2.1 Experimental

Two sets of experiment have been performed. First, the response of a sample of MWCNT grown on SiO_2, used as active electrode of a chemical cell under irradiation, is analyzed. The sample name is "160908" and its synthesis and structural characterization have been described in detail in Paragraph 3.3.4. Its MWCNTs are randomly distributed and the values of the structural parameters are reported in Table1.

[5] Not to confuse with the total conversion efficiency η introduced in Chapter 1.

External channel (nm)	%	Internal channel (nm)	%	N. of walls	%
4.0 ± 2.3 7.1 ± 2.4	74% 26%	7.9 ± 2.2 11.5 ± 2.2 14.5 ±1.7 17.2 ±4.1	33% 37% 23% 7%	5 ± 1 8 ± 1 9 ± 2 13 ± 2	9% 29% 41% 21%

Table 4. Values of the structural parameters, external and internal channel, and number of wall for the sample "160908". This is a sample of NTs grown on a SIO2 substrate covered by 1nm of iron (growth time 10 min, C_2H_2 flux of 200 sccm, chamber pressure 12.0 ± 0.2 Torr).

Then, the comparison between the two samples, SiO_2/MWCNT and SiO_2/MWCNT/Cu, are reported. Both have been grown according to same experimental conditions. The latter has been then decorated evaporating Cu in ultra-high-vacuum conditions (detailed characterization results of morphology and structure are described in Paragraph 3.4). The metal nanoparticles do not perturb the graphitic structure of MWCNT. Their average diameter is of about 4.0±1.0 nm. The MWCNTs are randomly growth with structural parameters described in Table2.

Sample	External channel (nm)	Internal channel	N. of walls
SiO_2/MWCNT	7,6 ± 1,7 (50%) 10,8 ± 3,0 (44%) 15,4 ± 1,5 (6%)	4,0 ± 1,0 (37%) 4,9 ± 3,3 (63%)	5 ± 1 (23%) 7 ± 1 (35%) 9 ± 4 (42%)
SiO_2/MWCNT/Cu	7,9 ± 2,2 (33%) 11,5 ± 2,2 (37%) 14,5 ± 1,7 (30%)	4,0 ± 2,3 (74%) 7,1 ± 2,4 (26%)	5 ± 1 (25%) 8 ± 1 (29%) 9 ± 2 (46%)

Table 5: Structural parameters distribution for the two samples of MWCNTs grown in the same experimental conditions. On the second one, Cu has been evaporated in a second time.

The photochemical experiments have been performed by using a three electrode chemical cell. Electrochemical cells require at least two electrodes, since the potential of a given electrode can only be measured relatively to another electrode, whose potential must be constant (reference electrode). To measure the current flowing in the cell, a precise control of the external applied voltage is required, but this is generally not possible with a two electrode system, owing to a potential drop across the cell

induced by the solution resistance (potential drop is equal to the current times the solution resistance). A better potential control is achieved using a potentiostat and a three electrode system, in which the potential of one electrode (the working electrode) is controlled relatively to the reference one, while the current passes between the working electrode (active or counter electrode) and the third electrode (the auxiliary electrode).The polarization of the counter electrode is required to complete the current measuring circuit.

The major requirement for a reference electrode is that the potential does not change as a function of time. Since the passage of current through an electrode can modify the potential, such effects for the reference electrode in a three electrode system are minimized by a) obtaining a high-input impedance for the reference electrode (thereby decreasing the current passing through the reference electrode to negligible levels) and b) using a non-polarizable electrode as the reference electrode (i.e. the passage of small currents does not alter the potential). The reference electrode used in the measurement set, whose results are reported in this chapter, has been a saturated calomel electrode (SCE). The SCE is a reference electrode based on the reaction between elemental mercury and Hg_2Cl_2. The aqueous phase in contact with the mercury and the Hg_2Cl_2 ("calomel") is a saturated solution of potassium chloride (Cl^- (4M)|Hg_2Cl_2(s)|Hg(l)|Pt) [6] in water. The electrode is normally connected via a porous frit to the solution, in which the other electrode is immersed. The electrode is normally linked via a porous plug to the solution in which the other electrode is immersed (Fig.1b))

Photoelectrochemical measurements have been performed at Science and Chemical Technologies Department of the University of Rome Tor Vergata (laboratory of Prof. M. Venanzi), using the cell sketched in Fig.1a). The working electrode is just the MWCNTs sample under investigation, while the counter electrode is a standard platinum (Pt) wire. A 0.5M NaI and 0.01M I_2 in acetonitrile solution has been used as electrolyte. A 200W Xe lamp (Osram) has been employed as excitation source (λ>300nm). The intensity of the light near the electrode surface was estimated to be about 50 mW/cm^2 by azobenzene actinometry [3]. Photocurrent measurements have been carried out using the Xe lamp equipped with a monochromator to select the incident monochromatic excitation wavelength and a PG-310 (HEKA

[6] At standard conditions, the potential of the saturated calomel electrode should be +0.241 V versus the Standard hydrogen electrode (SHE).

ELEKTRONIK) potentionstat to measure the generated current. The intensity of the photocurrent signal has been normalized to the excited area covered by the nanotubes.

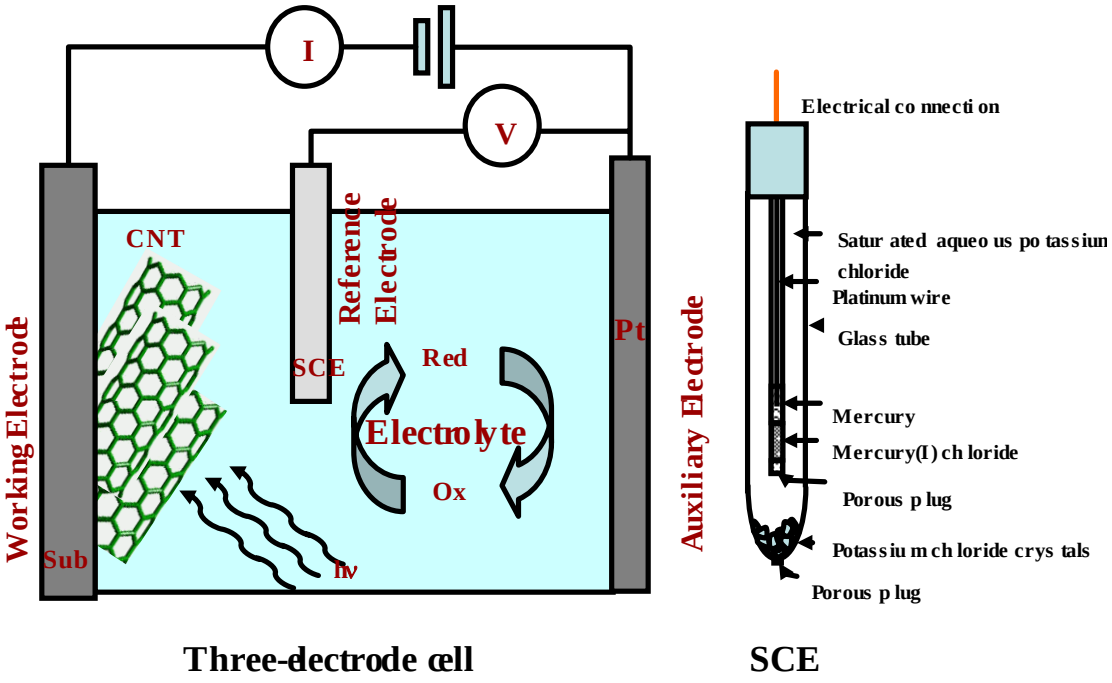

Fig. 1. a) Scheme of the three electrode cell used for photochemical measurements. b) Particular of the saturated calomel electrode (SCE) reference electrode.

4.2.2 MWCNTs photochemical current generation mechanism

The MWCNTs "160908" electrode performance has been obtained by recording the photocurrent density at different incident photon energies. We first carried out the experiment on a bare SiO_2 sample by exciting it with several optical and near IR frequencies. The photocurrent signal obtained turned out to be structureless and of negligible intensity throughout the investigated photon energy range. In Fig.2, it is reported the response under visible excitation light of 400 nm.

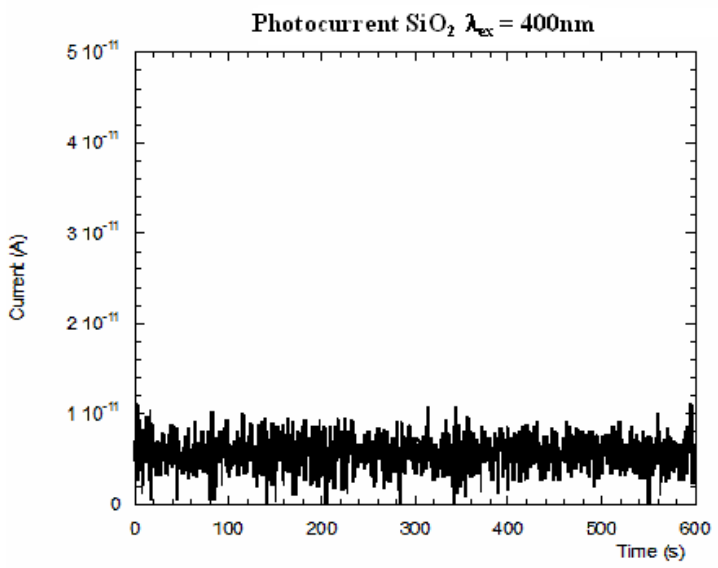

Fig. 2. Photocurrent of a bare SiO_2 sample excited with visible light $\lambda = 400$ nm.

On the other hand, when a similar experiment has been carried out on the SiO_2/MWCNT "160908" specimen, photocurrent off-on cycles have been obtained[7], (Fig.3). It is worth to notice that the intensity of the measured photocurrent remains highly sTableas a function of time, thus suggesting that nanotubes do not degrade under operative conditions.

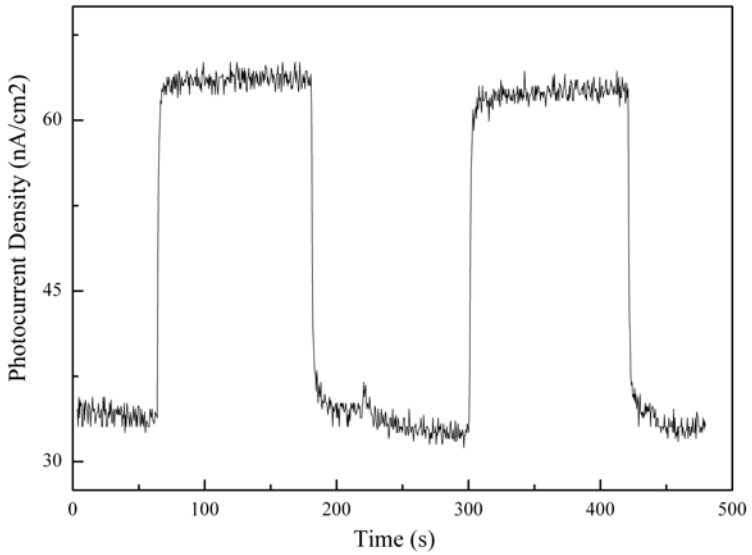

Fig. 3. Photocurrent off-on cycles of SiO_2/MWCNT "160908" sample excited with visible light $\lambda = 400$nm.

The anodic nature of the photocurrent signal, evidenced by the off-on current cycle in Fig.3, indicates the electronic character of the charge carriers. The electrons

[7] The starting phase, t = 0 s, the stat of light is off, so an increment of the net current is observed when the light is on.

are collected at the electrode surface and the holes are scavenged by the electrolyte in the solution, giving rise to a net anodic current. The regenerative I^{3-}/I^{-} redox couples facilitate the scavenging of charges at the electrodes surfaces, thus enabling the delivery of steady-state photocurrent.

Originally, photocurrent generation measured with an electrochemical cell on carbon nanotubes was obtained mainly by single-walled nanostructures. In fact, MWCNTs were not expected to show analogous low dimensional effects, owing to their close similarity to metallic graphite. In spite of this, this experiment shows that also MWCNTs are able to generate photocurrent upon irradiation. The question is what is the physical mechanism for the establishing of a steady-state photocurrent.

Although ab-initio calculations on DOS have not yet performed owing to the complexity of the multi wall nanotubes (larger number of shells and mutual interactions), it is possible to have an indirect demonstration of singularities existence in MWCNT DOS by performing adequate experiments (See Chapter 2).

Fig.4 reports the EELS spectrum reflections of the MWCNTs sample "160908", of a highly oriented pyrolitic graphite (HOPG) sample and a SWCNTs[8] one (for a detailed description of the EELS technique, see Appendix C). Reflection electron energy loss spectroscopy (REELS) measurements have been carried on using a constant kinetic primary energy of 300 eV. HOPG shows two typical features due to π and σ plasmons located at 6.5 eV and 27.0 eV, while MWCNTs and SWCNTs spectra present a shoulder at the energy range 2 - 4 eV, well below the typical plasmon π -π^* peak for HOPG. In the case of SWCNTs, such transitions have been reported and interpreted as excitations between localized electronic states related to van Hove singularities. In the case of MWCNTs, this shoulder should be associated to the same singularities that are still present in their electronic density of states. These transitions have been considered to be responsible for the photocurrent generation, since they allow the exciton generation upon illumination.

[8] SWCNTS, having a narrow diameter distribution peaking around 1.2±0.1 nm, were synthesized by ablating a CoNi-doped graphite target, using a pulsed Nd:YAG laser in the superimposed double-pulse configuration by M.A. El Khakani [Khakani].

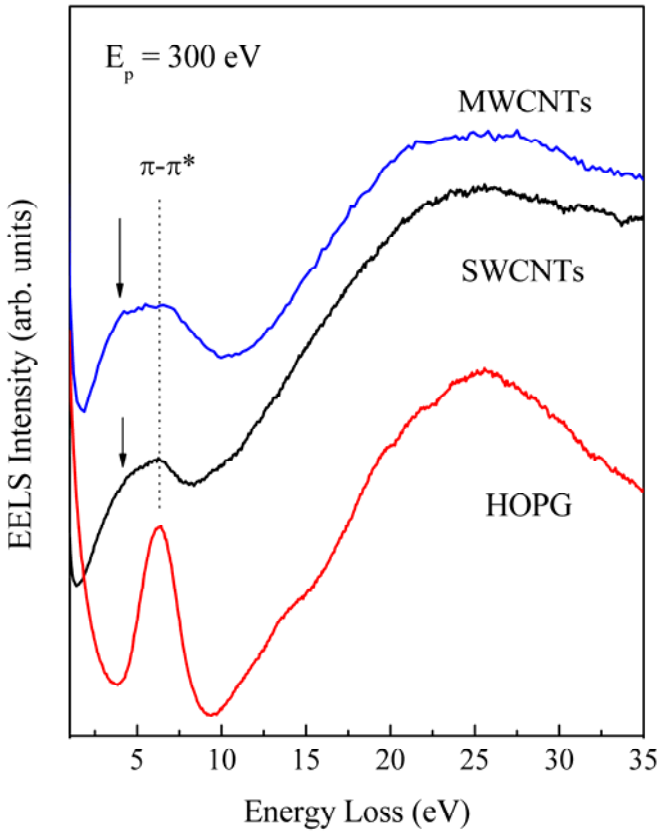

Fig. 4: Reflection electron energy loss spectra measured for HOPG, SWCNTs and MWCNTs samples. Note the shoulder in the SWCNTs and MWCTNs spectra at energies lower than the plasmon π -π* peak, typical of the graphitic systems. Primary electron beam is 300 eV.

4.2.3 Effect of decoration of MWCNTs with metal nanoparticles

It has been recently shown that the dispersion of semiconducting quantum dots [4-5], or metallic (Au) nano-particles [6], on the nanotubes sidewalls yields a significant enhancement in the photoconversion efficiency. In this regard, a great deal of research has been devoted in order to comprehend the modification of the electronic properties of carbon nanotubes/metal hybrids as a function of the type, size and shape of the dispersed metal nano-particles [7-10]. Theoretical and experimental data obtained from metal-coated nanotubes demonstrate that metals are likely to mechanically stabilize and passivate defect sites on the CNT surface. In the case of 3d elements on SWCNTs [8], it has been observed that the nature of the system contact resistance can vary significantly, and a sizeable charge transfer from metal to carbon has been theoretically predicted. The charge transfer affects not only the 4s but also the 3d electrons of copper [11].

In MWCNTs, the presence of numerous concentric cylindrical walls provides additional pathways for the flow of photogenerated charge carriers. The obvious

challenge is to use a MWCNTs network in a solar cell as a scaffold to anchor light-harvesting metal nano-particles and facilitate the electron transport to the collecting electrode surface. The intensity of the photocurrent obtained from MWCNTs and Cu-MWCNTs samples are normalized to the excited area covered by nanotubes (Fig.5). Also in this case the anodic nature of the photocurrent signal, evidenced by the off-on current cycle reported in Fig.6, indicates the electronic character of the charge carriers.

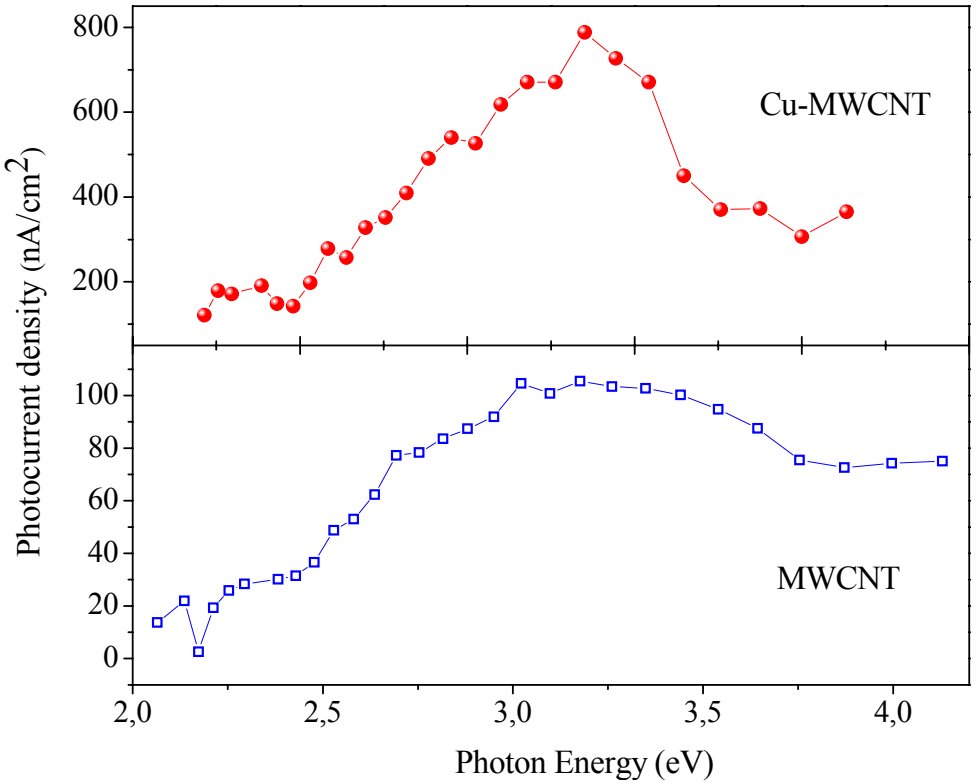

Fig. 5. Photocurrent density response in MWCNTs and Cu-MWCNTs obtained as a function of incident photon energy. Empty blue squares (□) indicate MWCNTs sample, filled red circles (●) Cu-MWCNTs sample.

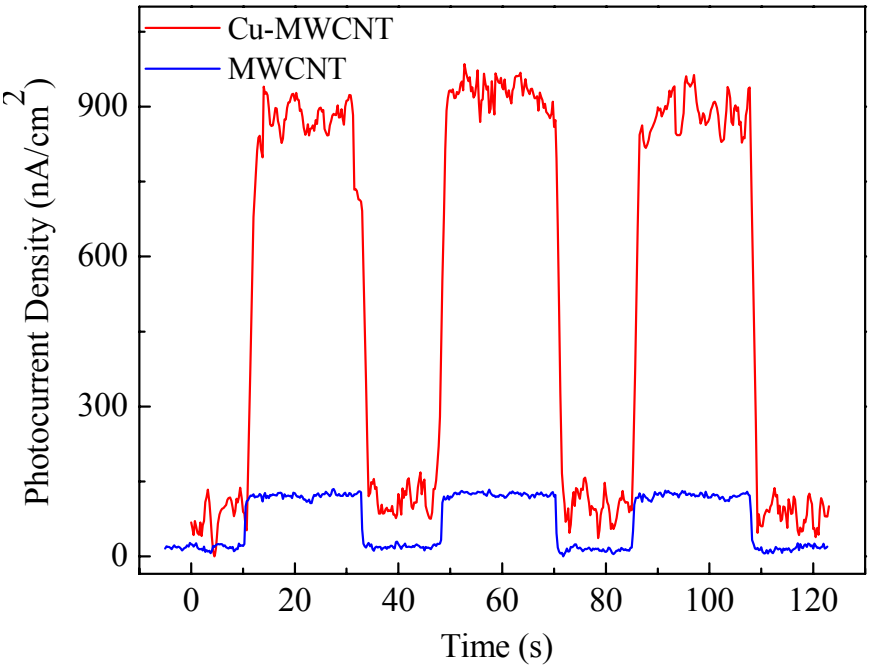

Fig. 6. Typical off-on current cycle in MWCNTs (blue line) and Cu-MWCNTs (red line) obtained at λ=400 nm.

A sketch of the apparatus, with an illustration of the electron transfer from the photoexcited Cu-nano-particles and the MWCNT, is reported in Fig.7. In the proposed scheme, the electron is collected at the electrode surface and the hole is scavenged by the electrolyte in solution giving rise to a net anodic current.

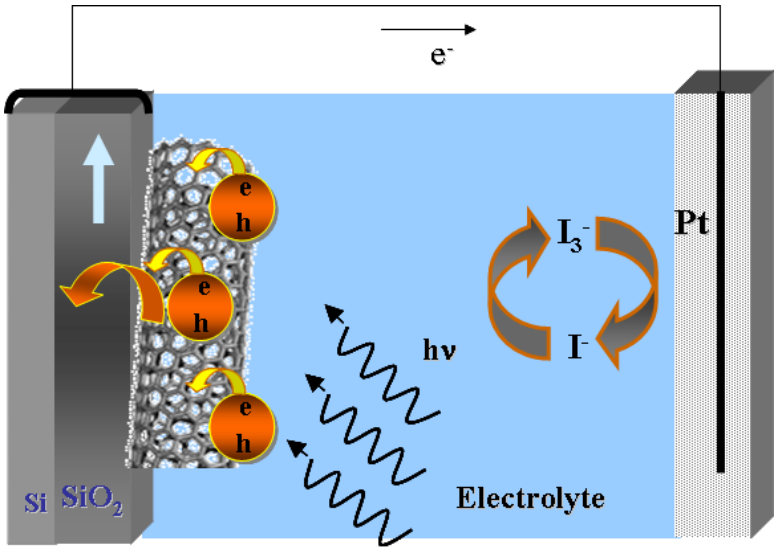

Fig. 7. Light-induced charge separation in the photoelectrochemical cell based on Cu-MWCNTs. In the proposed scheme the electron is collected at the electrode surface and the hole is scavenged by the electrolyte in solution giving rise to a net anodic current. Electrolyte: NaI 0.5M and I2 0.01M in acetonitrile.

The *IPCE* obtained from MWCNTs and Cu-MWCNTs at different photon excitation energy (Eq. 3) is reported in Fig.8. The maximum *IPCE* is around 3.3 eV for MWCNTs confirming the result reported in earlier experiments performed on similar samples [1][2]. The *IPCE*, at the emission maximum, reached 1% for bare MWCNTs while a significant increase up to 4.5% for Cu decorated multiwall CNTs is measured. The Fig.9 reports the absorption spectra. Absorption measurements on MWCNTs/SiO2 and Cu-MWCNTs/SiO2 electrodes have been carried on using a commercial apparatus (Perkin-Elmer, LAMBDA 15). The signal has been obtained by irradiating a conventional 1 mm quartz cuvette containing the synthesis product diluted in isopropyl alcohol. The absorption spectra resembles the spectra of the photocurrent density.

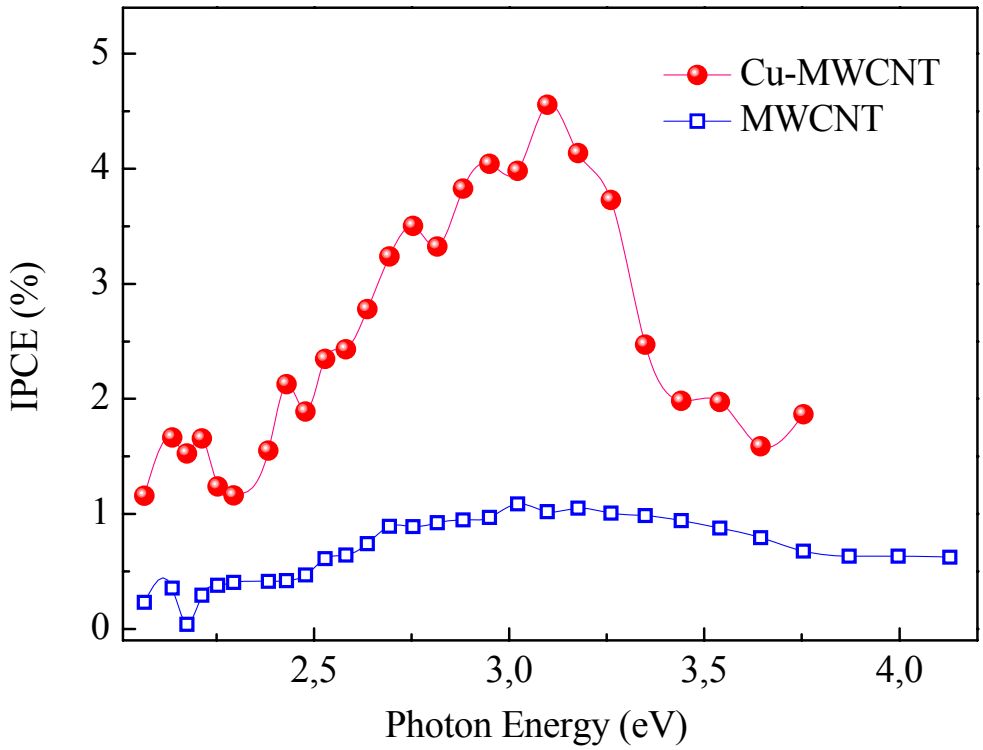

Fig. 8. Photocurrent action spectra (color on-line) of MWCNTs (empty squares □) and CuMWCNTs (full circles ●), obtained as a function of incident photon energy (CE is Pt; electrolyte is NaI 0.5 M and I_2 0.01M in acetonitrile). *IPCE* is determined using the equation 3.

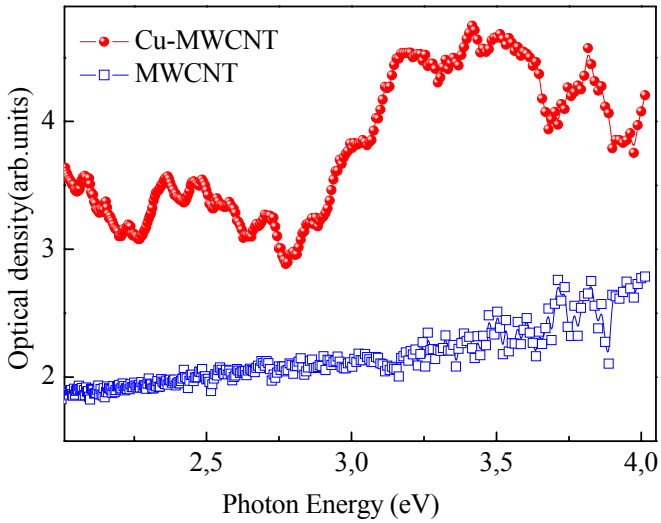

Fig. 9. Absorption spectra of MWCNTs (empty squares □) and CuMWCNTs (full circles ●) performed in solution. Note that the absorption resembles the action spectrum of the photocurrent density.

The increase in the overall photocurrent signal for Cu-MWCNTs demonstrates the ability of Cu nano-particles to notably modify the electronic properties of the entire hybrid system. Copper is known to be a good electron donor upon photo excitation. Therefore, the photocurrent signal enhancement indicates that additional electrons added by the Cu nano-particles are efficiently transferred to the numerous concentric cylindrical walls of carbon nanotubes, which offer several pathways for the flow of photogenerated charge carriers. The additional charge comes out by a localization of the electronic levels due to the reduced size of metal particles (loss of metallicity) [12-13] (Fig.10). Therefore, it is possible to vary the electronic properties of the metal nano-particles and increase the total absorption of the carbon nanotube/metal nanohybrids. Another possible reason to explain the increase of the photocurrent is the following: it is possible that the Cu nanoparticles (because of their nanometre dimension) generate a high local electric field on the wall of the carbon nanotube. This enhances the photocharge separation inside the nanotubes, thus facilitating the collection of the produced e-h carriers at the electrode.

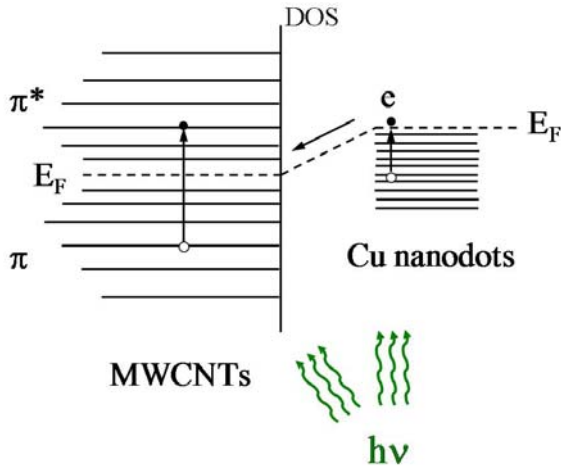

Fig. 10. Suggested picture to describe the hybrid system electronic state.

4.3 Photoconductive Properties of MWCNTs based solid state devices

In this Paragraph the results of photoconductivity measurements on solid-state devices formed by a film of MWCNTs random network grown on a SiO_2/Si substrate will be presented. The aim is the study of the photoconductive capability of MWCNTs without the contribution of the electrolyte, characteristic in photochemical cells.

A possible interpretation for the current flow in the MWCNTs random networks and of their spectral photoresponse are suggested on the base of the experimental results and theoretical calculations performed by Dr. Continenza's group (Department of Physics at University of L'Aquila, Italy).

Finally, preliminary study on the device PV performance has been carried on.

4.3.1 Experimental

The optical measurements have been performed by a chopped radiation source and a lock-in technique. The set-up for measuring the modulated photocurrent is shown schematically in Figs. 11 and 12.

The source is an 150W Xenon Arc Lamp and the radiation wavelength (energy), ranging from 200 nm up to 900 nm (1.4 eV up to 6.2 eV), has been selected by a f/3.4 monochromator. The excitation light has been monitored by a calibrated Silicon diode (sensitivity range from 350 nm to 1080 nm), the signal has been amplified by a photodiode amplifier (Thorlabs PDA200C). An optical chopper has been used to

modulate the radiation before impinging the sample. The blade of the chopper is coated by aluminum: in this way, rotating the chopper at 45° in respect to the optical axis, it is possible to deviate the radiation on the photodiode. The frequency of the chopper (6.7 Hz for measurements on MWCNTs) has been sent to a Signal Recovery DSP Lock-in Amplifier as modulation reference signal. The current signal coming from the sample has been amplified and transformed to a voltage signal by a Femto DLCPA-220 current preamplifier. Ag metal contacts with coplanar configuration have been prepared by putting conductive silver paint directly on the random network of the MWCNTs at a relative distance *d* ranging from 5 to 10 mm. Fig.13 shows a schematic picture of the experimental device realized with the MWNT/SiO_2/Si samples; the resistance measured between the electrodes of different samples is hundreds of Ohm. The photodiode and the sample signals are contemporarily acquired by a Labview program opportunely developed for these experiments.

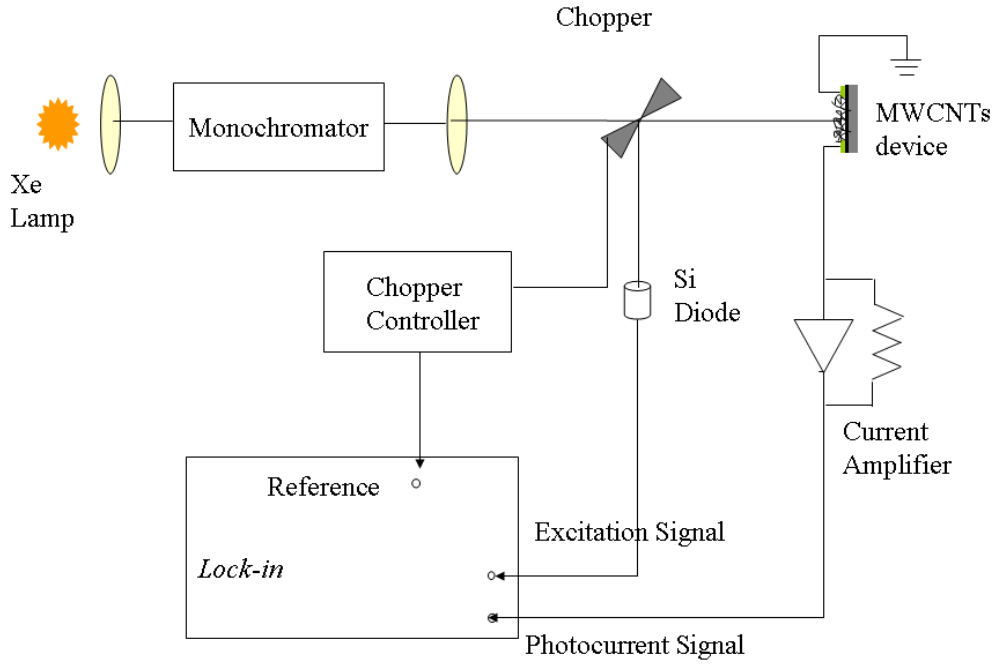

Fig. 11. Block diagram of the optoelectronic set up.

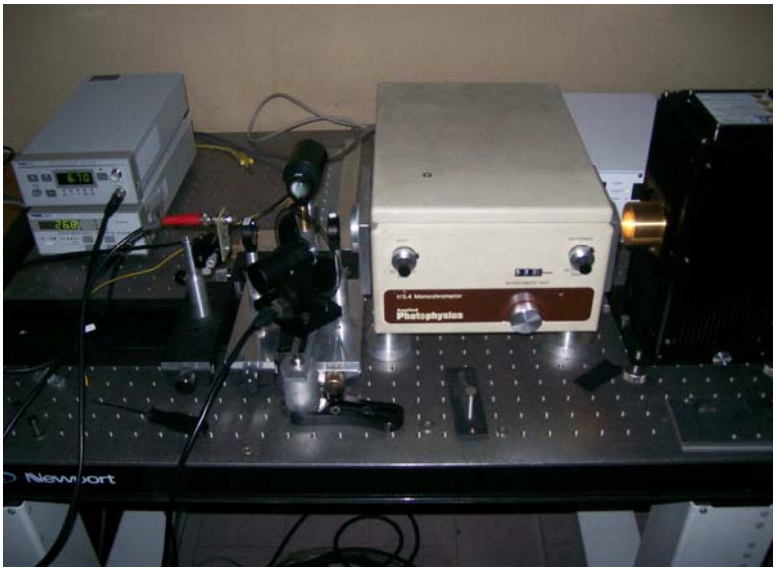

Fig. 12. Picture of the experimental optical setup.

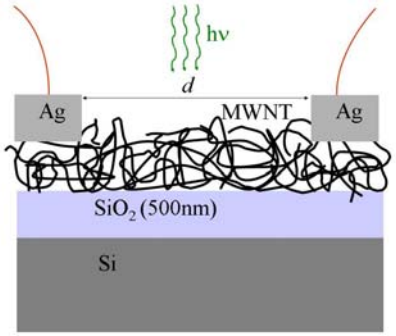

Fig. 13. Scheme of the device used to perform photocurrent measurements. Note the planar geometry of the metallic contacts.

The spectrum of lamp power is measured by the Si photodiode is reported in Fig.14 after suitable multiplication for the gain of the voltage-to-current amplifier and division for the silicon diode interpolated responsivity (see Fig.15).

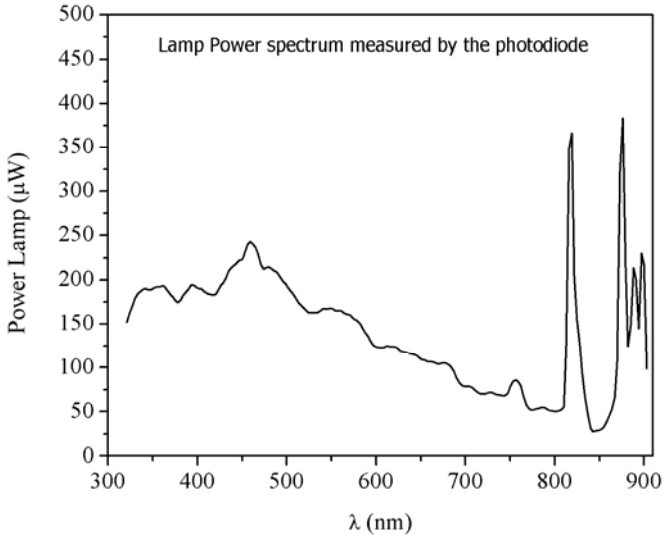

Fig. 14. Spectrum of lamp power vs wavelength measured by the photodiode

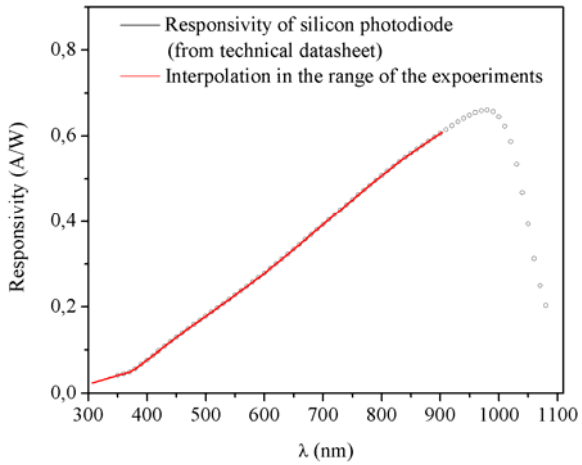

Fig. 15. Responsivity of the silicon photodiode. The open black dot curve is the responsivity given by the manufacturer. The red line is the interpolation of the responsivity in the range of interest 300 - 900 nm.

A p-n polycrystalline silicon cell has been measured to test the apparatus. In Fig.16, the *QE* obtained by Eq. 1&3 is plotted as a function of energy source. The *QE* is in agreement with those of the standard silicon cells. In fact, while quantum efficiency ideally has a square shape between 350 nm and 1115 nm (silicon band-gap is 1.11 eV), for most solar cells it is reduced due to recombination effects and optical losses, such as transmission and reflection [14].

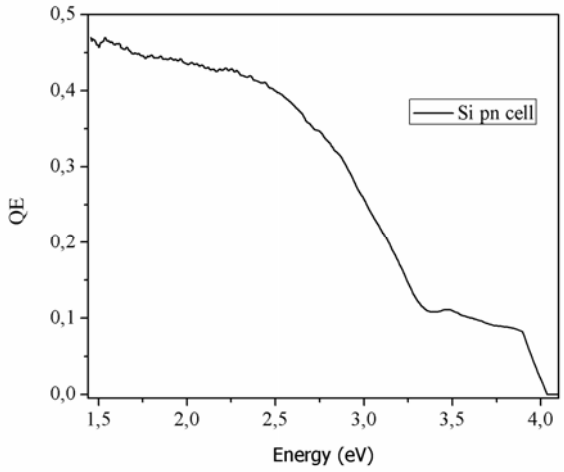

Fig. 16. Plot of *QE* of the polycrystalline Si p-n cell as a function of the radiation energy. Ideally it should be equal to unit with a square shape, but the effects both of recombination and of optical losses decrease it.

To understand if some filter is necessary to stop the wavelength higher orders, measurements on a standard polycrystalline silicon cell have been carried on using a 520 nm filter placed at the output of the monochromator. The current density flowing through the sample is compared to that acquired without the filter to verify the possible contribution of higher orders of lower wavelengths to the response of sample irradiated at a fixed (higher) wavelength. The comparison is shown in Fig.17. It is evident that, at wavelength higher than 520 nm the intensity of the current density slightly decreases, but no fingerprints, produced by the contribution of not desired orders, appear. This allows to avoid the use of any filter that could absorb part of the incident radiation power and consequently reduce the expected signal.

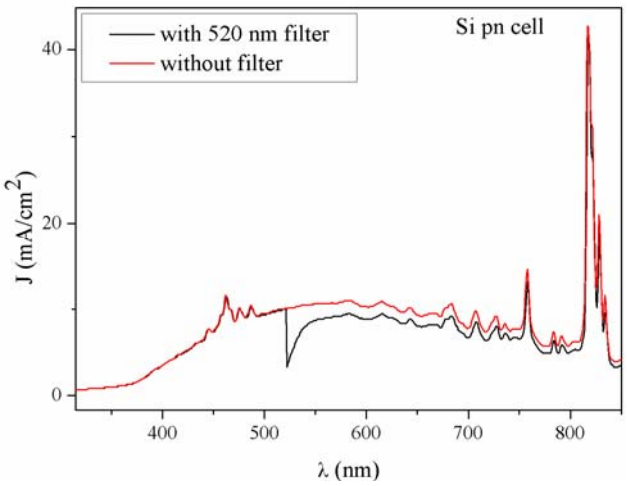

Fig. 17. Comparison of the current density flowing through a polycrystalline silicon cell irradiated by monochromatic light with and without a 520 nm filter at the output of the monochromator. Only a decrease of intensity is visible, wile there is not contribute from higher order of low wavelengths for $\lambda \geq 520$ nm.

The experiments have been performed on a set of different samples. In the following, we report the experimental results on:

a. PV silicon cell, as reference conversion device.
b. Sample of MWCNT named “0304”, whose the structural parameters are summarized in Table 3.
c. Two samples grown in the same experimental conditions, one of them has been decorated with metal nanoparticles by evaporating Cu: MWCNT and MWCNT/Cu, named respectively “2109” and “2509”, with structural parameters summarized in Table 3.

All the MWCNTs are randomly grown and the structural parameters are reported in Table3. The Cu nanoparticles, decorating the MWCNTs without perturbing their graphitic character, have an average diameter of about 3.0 ±1.0 nm. For detailed description of the synthesis methods and morphological and structural analysis the reader is referred to Chapter 3.

Sample	External channel (nm)	Internal channel	N. of walls
MWCNT “0304”	9.6 ± 1.6 (9%); 15.1 ± 2.3 (46%); 21.2 ± 2.4 (27%) 28.6 ± 2.1 (18%)	5.6 ± 1.7 (30%) 8.9 ± 2.6 (70%)	10 ± 2 (19%) 14 ± 2 (40%) 18 ± 2 (27%) 30 ± 2 (14%)
SiO_2/MWCNT “2109”	9.2 ± 1.4 (97%) 12.8 ± 0.6 (3%)	3.5 ± 1.1 (84%) 6.0 ± 1.2 (16%)	10 ± 1 (87%) 14 ± 2 (13%)
SiO_2/MWCNT/Cu “2509”	9.8 ± 1.8 (38.6%) 14.5 ± 2.5 (43.4%)	4.9 ± 1.9 (62%) 8.5 ± 2.2 (38%)	9 ± 3 (85%) 15 ± 2 (15%)

Table 6. Structural parameters distribution of samples whose photospectral response is investigated and described in this paragraph.

4.3.2 Solid-state MWCNTs device photocurrent generation mechanism

Initially the current spectra of the 0304 sample, MWCNTs on SiO_2, have been collected as a function of the photon energy using the Xenon lamp and positioning the spotlight (size 2 x 3.7 mm^2) at different distances from the metallic contact electrodes (minimum distance between electrodes is 6 mm).

The photocurrent density J by dark-light cycles at each photon energy has been recorded. The photocurrent induced by dark-light cycles results to be a square signal as a function of time. In Fig.18 the dark-light cycles at λ=500 nm and with white light are shown. It is important to stress that these results outline the presence of a non zero *QE*, revealing a true photovoltaic effect.

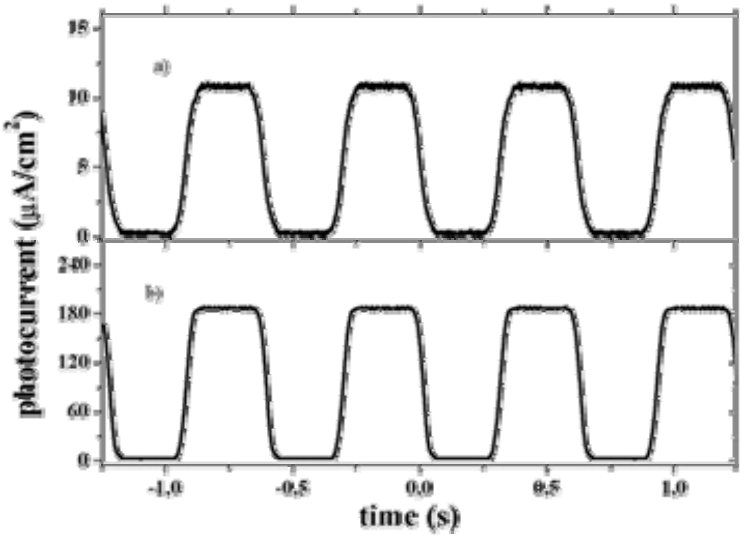

Fig. 18. Dark-light cycles at (a) λ = 500 nm and (b) white light for the 0304 sample of MWCNT on SiO_2.

In Fig.19 the current density spectra of the sample are shown. The presence of several peaks are due to the peaks of the lamp spectrum.

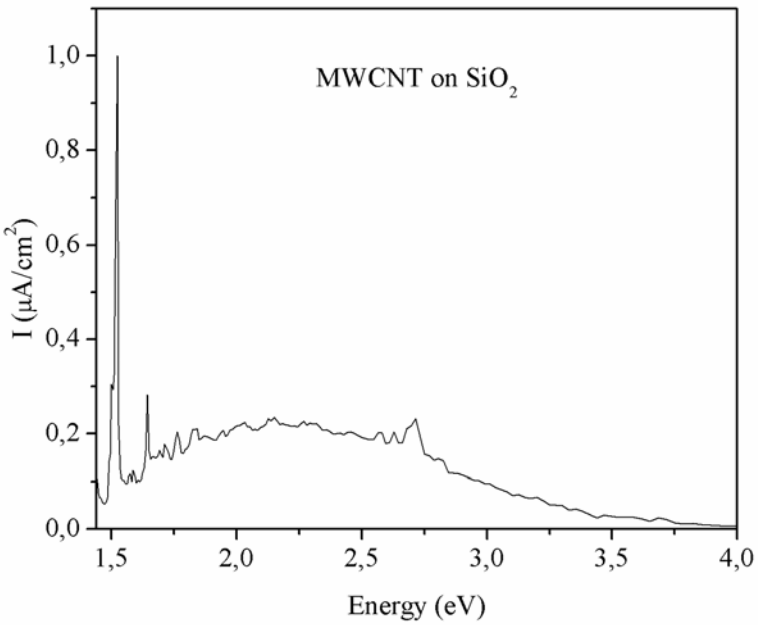

Fig. 19. Current density flowing through the MWCNTs sample "0304"

Varying the distance of the light incident point from the planar metallic contacts, the largest photocurrent value are found close to the not grounded electrode and there is a general decrease moving the light towards the ground electrode.

From Eq. 1&3, the *QE* can be calculated and its spectrum is shown in Fig.20(a) as a function of the photon energy. A much lower (three order of magnitude) *QE* has been recorded from a slice of bare SiO_2/Si substrate, suggesting that the measured photoresponse is basically induced by the carbon nanotubes (see Fig.21). Notice that this spectrum is rather noisy owing to a current signal very low and consequently less stable.

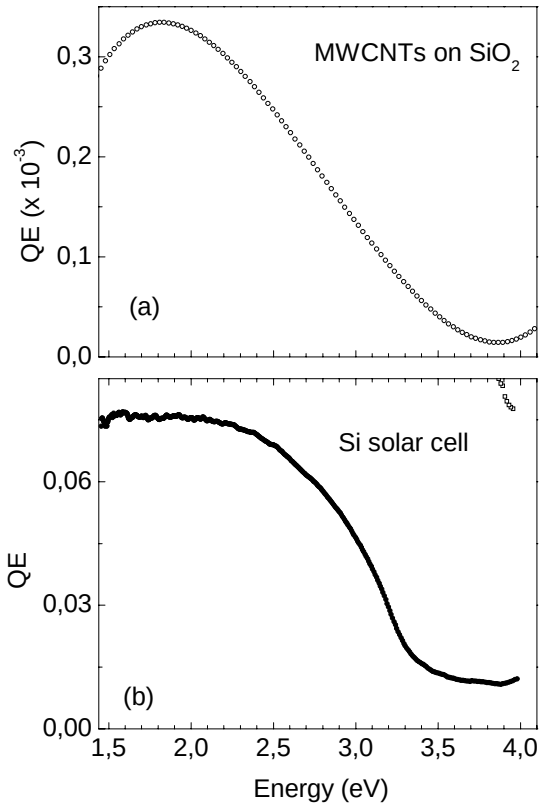

Fig. 20. (a) Quantum efficiency of MWCNTs random network (open dots); (b) QE for a conventional silicon solar cell (filled dots) calculate/obtained in the same planar geometry illustrated in Fig.13.

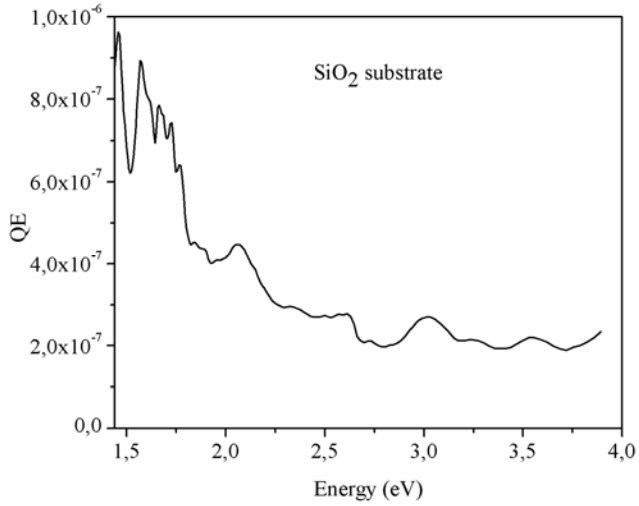

Fig. 21. *QE* spectrum of a bare SiO_2 substrate. The spectrum is rather noisy owing to a current signal very low and consequently unstable.

Fig.20 (b) shows the *QE* spectrum collected by a commercial silicon p-n solar cell and obtained measuring the photocurrent in the same planar geometry illustrated in Fig.13. The maximum external quantum efficiency achieved by the MWCNT device is two orders of magnitude lower than that of conventional silicon solar cell (planar

configuration). However, the MWCNTs *QE* spectrum (Fig.20(a)) shows a broad feature located at about 1.8 eV and it extends over a wide energy region similarly to that measured in polycrystalline silicon solar cell.

Photoinduced current generation upon light illumination, not in chemical cells, has been previously reported using SWCNTs suspended between two metallic electrodes [15-17]. These measurements have been interpreted as related to the generation in 1D systems of photoexcited electrons and holes that create strongly bound excitons. MWCNTs random networks behave in a similar way under illumination. In fact, in paragraph 2.2.2 the presence of singularities has been shown also in DOS spectrum of MWCNT, by measuring the electron energy loss spectra (Fig.4). In the next paragraph a further investigation on the MWCNTs photocurrent generation will be presented showing the results of ab-initio calculations of the electronic properties of a specific MWCNT. They demonstrate that the DOS of MWCNTs can be well reproduced by a superposition of the DOS of SWCNTs constituting the MWCNT structure, each maintaining its one-dimensional features in the electronic and transport properties. Moreover, it will be shown that metallic nanotubes have rather long Thomas-Fermi static screening length, that may induce a non-perfect screening of the e-h pairs generated within the nanotubes upon illumination. That could allow photo-induced currents even in metallic MWCNTs.

In photochemical experiments the presence of an electrolyte guarantees the charges separation and the establishment of a steady-state current. In this case another factor has to substitute the role of the electrolyte in the current establishing mechanism.

The observation of a density photocurrent implies that each electron-hole pair is separated by a built-in electric field. The electric field could be the result from several local Schottky junctions within the same tube or from the interaction between semiconducting and metallic nanotubes [15]. In particular, the former effect can be originated by atomic defects, bending, twisting and doping, producing local changes in the electronic properties and/or variations of chirality etc. [16-20]. Finally, the flux of the photogenerated charges towards the electrodes is driven by formation of two different Schottky barriers at the interfaces between the nanotubes and the metallic electrodes. Owing to the fact that the two metallic Ag electrodes are not symmetric, there is a current flow induced by the built-in-voltage, forming a Schottky barrier at the interface between nanotubes and the metallic electrode.

Finally, the lowering of the current signal, observed upon increasing the distance of the spotlight from one electrode to the sample centre, is an indication of the percolation process acting along the quantum nanotube structures immediately after the e-h generation [21]. This process significantly reduces the charge carriers ability to contribute to the current signal since they recombine before reaching the electrodes.

The quantum efficiency spectrum of our sample has been compared with those reported in literature. The MWCNTs spectral photoresponse reported in Fig.20 (a) is very different from those obtained on carbon nanotubes measured in other works, such as Ref. [22]. In that work, the spectra show an almost monotonic photoresponse trend with the highest intensity in the near-ultraviolet regions, which can be easily related to the MWCNTs absorbance. In our case, the absorbance of the MWCNTs (Fig.22), obtained dispersing few droplets of a mixture of isopropyl alcohol and scratched nanotubes on a quartz substrate, shows a maximum in the near ultraviolet region and a very low absorption where *QE* is maximum. On the other hand, in presence of an electrolyte, the photocurrent action spectra exhibit a maximum in the violet energy range.

In the following paragraph an explanation for this issue will be suggested on the basis of theoretical calculations. Starting from the calculated DOS, the MWCNTs absorbance is consequently obtained. It will demonstrate that the silicon substrate contribution to the quantum efficiency can not be neglected.

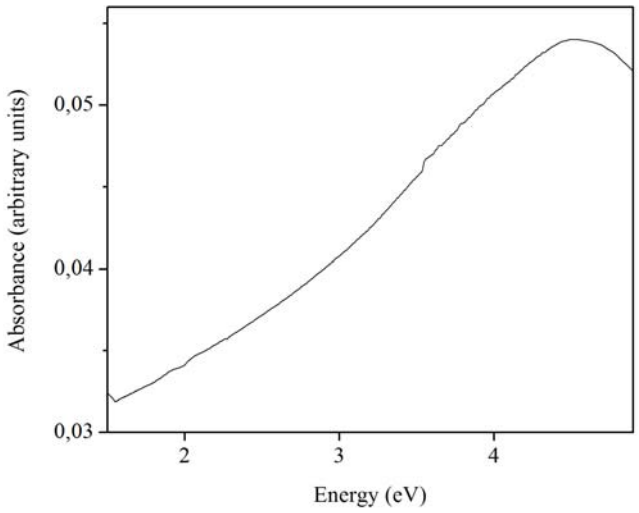

Fig. 22. Absorbance measured for the same MWCNTs after scratching of the sample and their dispersion on a quartz substrate through a several isopropyl droplets.

In principle the *QE*, as a function of the photon energy *E*, should be proportional to the absorbance, *A(E)*. For a conventional solar cell device, the photogenerated current density *J* is related to the generation rate *G(z)*, i.e. the number of charges generated at each point of the device due to the absorption of photons, and to the collection probability *P(z)*, i.e. the probability that a generated carrier absorbed in a certain region of the device will be collected. This follows the Eq. 4:

$$J = q\int_0^d G(z)P(z)dz\,, \tag{4}$$

where *d* is the total thickness of the device and *q* is the elementary charge. The electron-hole generation rate can be considered as the first derivative of the transmittance *T(E)* plus the reflectance *R(E)* with respect to z multiplied by the number of photons impinging at each photon energy and therefore. *T(E)* and *R(E)* are the percentage of the impinging light that is transmitted or reflected, respectively, at a given thickness, *d*, of the sample. If one considers a constant collection probability[9] over all the cell thickness, *QE* is proportional to the absorbance, *A(E)*.

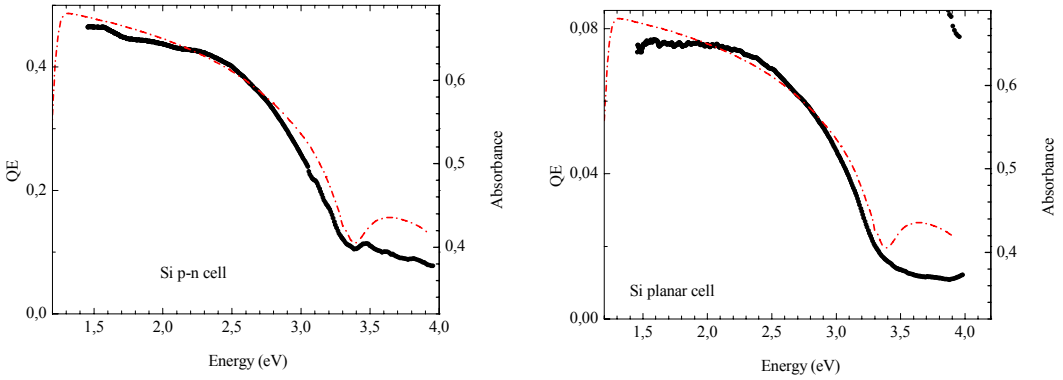

Fig. 23. Comparison of absorbance (red dot-dashed curve) calculated for a bulk silicon slab compared to the experimental *QE* (filled black dot curves) of a commercial silicon cell in sandwich configuration (plot on the left), and in planar configuration such as pictured in Fig.13 (plot on the right).

The absorbance is defined as *A(E) = 1 - T(E) - R(E)*, that can be determined in terms of the Fresnel coefficient of reflection and transmission of a multilayer system, once the complex refraction index (n,κ) is available [23]. Fig.23 shows the absorbance (red dot-dashed curve) calculated for a bulk silicon slab [14] compared to the *QE* (black filled dot curves) of a commercial silicon p-n junction, both in sandwich and in

[9] This probability, in a conventional p-n junction, is related to parameters of the device such as the diffusion lengths of the minority carriers in the p and n regions, the length of the depletion layers, the rate of surface recombination.

planar configuration. It is worth noting that the calculated absorbance reproduces all the features of the experimental *QE* quite well.

4.3.3 Theoretical calculation and experimental results interpretation

Ab initio DOS calculation and interpretation of the steady photocurrent current generation by MWCNTs device

Ab-initio calculations have been performed by the group of Dr. A. Continenza (Dept. of Physics, University of "L'Aquila") within Density Functional Theory using the Dmol3 code [24-25] for single as well as multiwall carbon nanotubes. The corresponding calculated DOS are reported in Fig.24 for an arbitrarily chosen set of SWCNTs, double and four wall (4WCNT) carbon nanotubes.

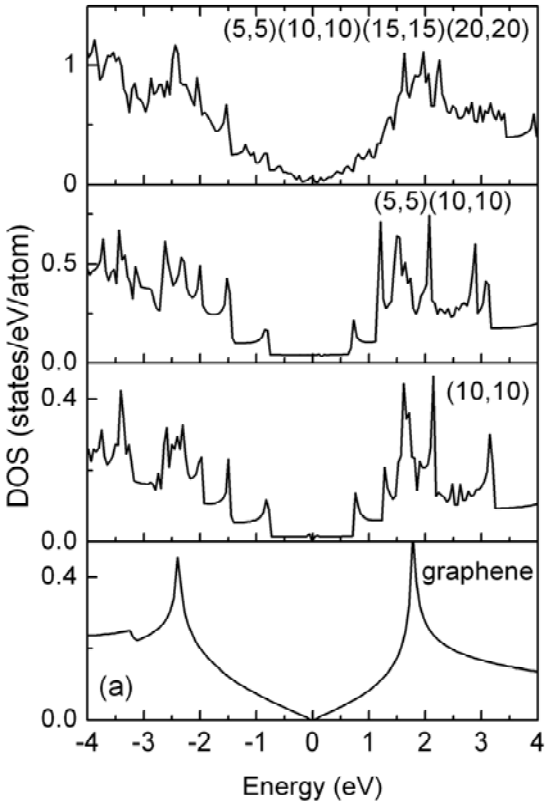

Fig. 24. Electronic DOS calculated for a graphene sheet, a (10,10) SWCNT, a (5,5)(10,10) DWCNT and a (5,5)(10,10)(15,15)(20,20) 4WCNT.

Moving from the simple graphene sheet (lower panel) towards the single wall (10, 10) nanotube, more complex structures appear due to, mainly, band-folding effects (i.e. the graphene band structure folded into the smaller Brillouin zone of the nanotube). As additional walls are considered, that is, as larger nanotubes are added

round the first one, this effect is amplified and an increasing number of singularities (peaks) are observed, consequently resulting in a smoother DOS with larger values. These results are in agreement with the experimental EELS spectra of Fig.4 reported in paragraph 2.2.2 showing a broader shoulder at energies 2-4 eV that indirectly gives information on the presence of singularities.

This can be explained taking into account two main effects: the first one is related to band-folding, as mentioned above; notice that, as the single wall diameter is increased, the 2D Brillouin zone shrinks correspondingly. The second one is related to the increasing number of nanotubes (walls): as shown in Fig.25, the total DOS of the 4WCNT structure is very close to the bare sum of the DOS of each SWCNT composing the structure. It reveals that there is a rather small interaction between nanotubes belonging to the same multi-walled structure.

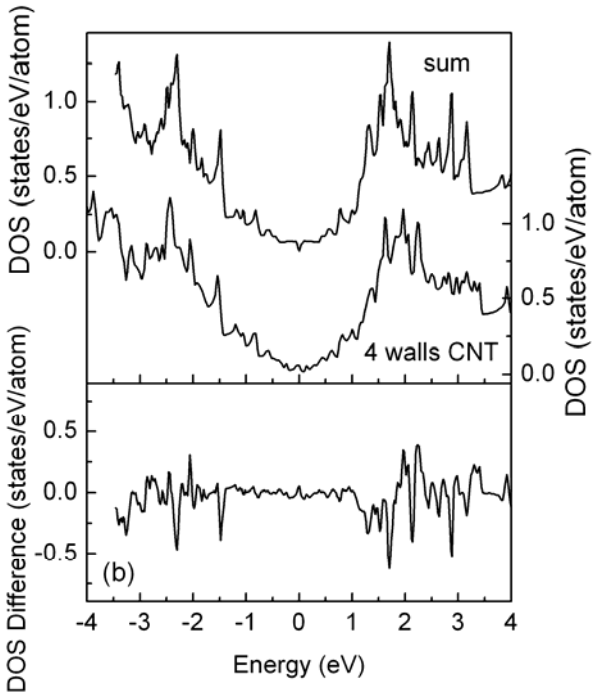

Fig. 25. Comparison between the electronic DOS calculated for (5,5)(10,10)(15,15)(20,20) 4WCNT and for the sum of four SWCNTs constituting the 4WCNT.

From the DOS at the Fermi level, the Thomas-Fermi static screening length, λ_{TF}, for the MWCNTs has been calculated. The obtained value ranges between 15 and 50 Å (14.8 Å for the one reported) corresponding to a carrier density at the Fermi level of the order of 9 x 10^{20} electrons/cm^3, quite smaller than the usual carrier densities in bulk metals (about 10^{22} electrons/cm^3). These findings imply that each e-h pair

created within the nanotube is far less screened than in a typical metal, thus explaining why even metallic nanotubes may give rise to photocurrent generation [26].

Calculation of the absorption spectrum of a multilayered MWCNTs device

To interpret the several experimental results obtained on MWCNTs, a comparison between the measured *QE* and the absorption spectra calculated for several thicknesses of the MWCNTs random network has been performed. The starting point is the four wall DOS shown in Fig.24. It is worth noting that the following simulation is only a rough interpretation of the experiment, since only this particular four-wall carbon nanotube has taken into account and the sample is not an ideal slab. Moreover, other additional physical mechanisms may likely occur in the MWCNTs random network.

The ab-initio electronic DOS has been used to calculate the imaginary part of the dielectric function and, by means of a Kramers-Kronig procedure, the real part of the dielectric function, ε_1, has been obtained. Fig.26 (a) shows the absorbance calculated for several thicknesses of the 4WCNTs film, showing an almost monotonic increase towards violet and near-ultraviolet photon energy.

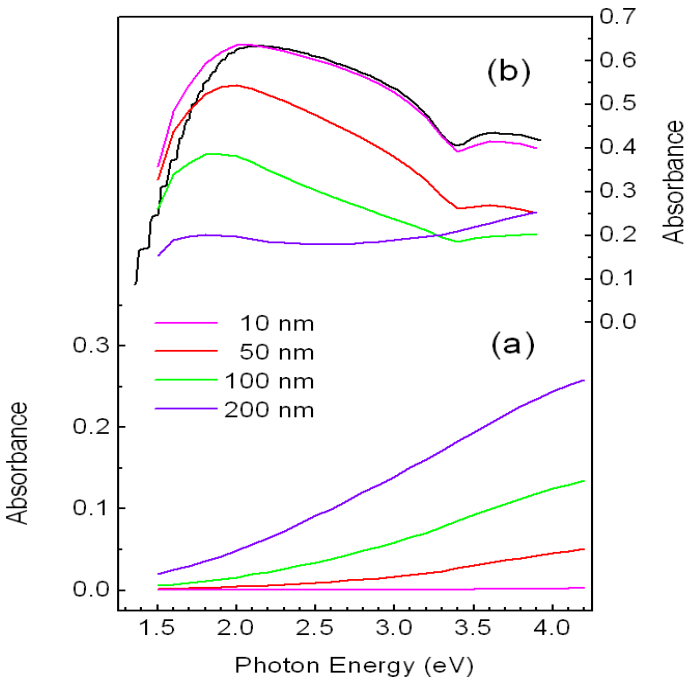

Fig. 26. (a) Absorption calculated for several thicknesses of a film constituted by the four walls carbon nanotubes reported in Fig.s 24,25. (b) Absorption calculated for several thicknesses of a film constituted by the four walls carbon nanotubes on a silicon substrate 10 μm thick.

These calculations explain the experimental absorbance (see Fig.22), the spectral photoconductivity for MWCTNs grown on an insulating substrate as sapphire [22] and the results of MWCNTs in a photochemical cell, shown in Paragraph 4.3. However, in the present device, despite the 500nm SiO_2 film, the silicon substrate underneath could have a role in contributing to the formation of several local Schottky and/or p-n junctions with the nanotubes of the network characterized by very long depletion layers. In Fig.26 (b) the absorbance calculated for a system constituted by the nanotubes film and a silicon slab about 10 μm thick on the silicon substrate is reported varying the nanotubes film thickness. It can be easily observed, that in this case the absorbance spectral distribution is very similar to that of a silicon slab, with the maximum shifting towards the red region by increasing the nanotube film thickness *d* up to a few hundreds nm and that, for *d* = 100nm, it well reproduces the features of the experimental *QE* shown in Fig.26 (a). An almost better result could be obtained if the collection probability of the photo-generated carriers would be considered, taking into account the carriers diffusion lengths, the mean free path of percolation, the surface recombination.

4.3.4 Effect of decoration of MWCNTs with metal nanoparticles on solid-state device.

Two samples are grown in the same experimental conditions, one of them has been decorated with metal nanoparticles by evaporating Cu. MWCNT (2109 sample) and MWCNT/Cu (2509 sample) whose structural parameters are summarized in Table3. In Fig.27 the current density spectra of the two samples are shown. Besides, the response of the MWCNTs sample moving the spotlight from close to one electrode towards the sample centre is reported. Away from the electrode, the intensity of current density is lower, as described in the previous paragraph, indicating the percolation process acting along the quantum nanotube structures immediately after e-h generation. In Fig.28 the calculated *QE* for both samples is compared. The results confirm the conclusion of Paragraph 4.2.

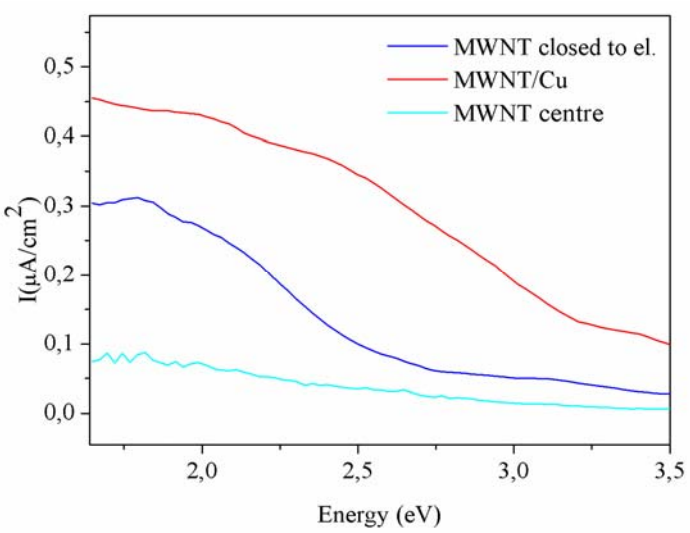

Fig. 27. Photocurrent density of MWCNTs and MWCNTs/Cu samples as a function of photon energy. The hybrid system shows an higher intensity in a wider photon energy range response: a shoulder appears in the range between 2.3 eV and 3.2 eV in respect to the MWCNTs sample. It is reported also the density of MWCNTs taking away the spotlight from close to an electrode to the centre. The intensity decreases due to the percolation process acting along the quantum nanotube structures soon after e-h generation.

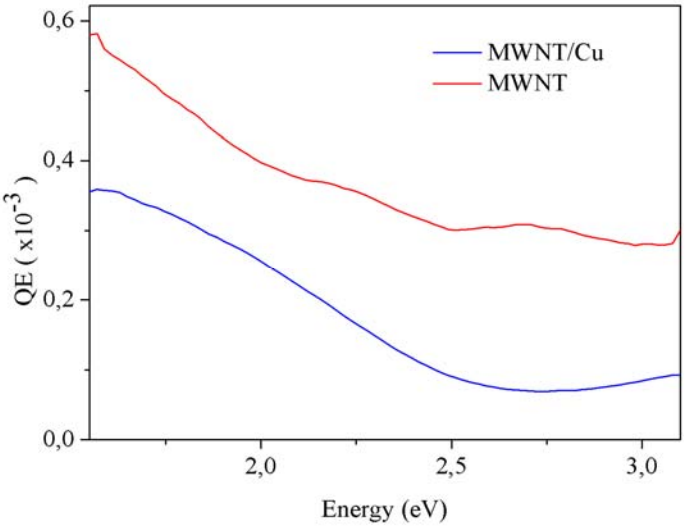

Fig. 28. Calculated *QE* as a function of photon energy for the sample MWCNTs and the hybrid system MWCNTs/Cu. The *QE* of the hybrid system is higher and it presents a wider photon energy range response in the range between 2.3 eV and 3.2 eV with respect to the MWCNTs sample.

4.4 MWCNTs based PV solar cell

As a first attempt, here the measurement of the performance of a MWCNT/SiO_2 PV cell is reported. The experiments have been carried on at the OLAB of Prof. A. Di Carlo (Department of Electronics Engineering of the University of Rome "Tor Vergata").

The device is based on the sample "0304" (Table3), made of MWCNTs on SiO_2 (500 nm thick) in planar configuration (Fig.13), previously studied in paragraph 4.3.4.

The characterization source light has been an Abbet Solar simulator, class A, able to reproduce the solar spectrum (1.5 AM). An Agilent source meter has supplied the bias voltage and measured the current flowing through the device.

The I-V of the MWCNTs device is shown in Fig.29. The shape of dark/light I-V characteristics show an Ohmic behavior that is very different from the typical one of a Si p-n cell. In any case, it shows a significant contribution in the electrical generator IV quadrant (for clearness in Fig.29 the sign has been reversed). Consequently, the I-V characteristic demonstrates that our device operates as an energy active element when illuminated by solar light. The performances of this device are very poor, as the evaluation of the fill factor (*FF*) demonstrates. The fill factor is essentially a measurement of the solar cell quality. It is calculated by comparing the maximum power available from device, P_{max}, to the theoretical power that would be the output at the open circuit voltage and short circuit current. The fill factor is equal to:

$$FF = \frac{P_{\max}}{I_{sc} \cdot V_{oc}} \sim 26\%,$$

far from the *FF* of commercial PV cells ranging from about 60% to 80%. Nevertheless this experiment represents an indication of the right pathway for developing new photovoltaic devices based on MWCNTs.

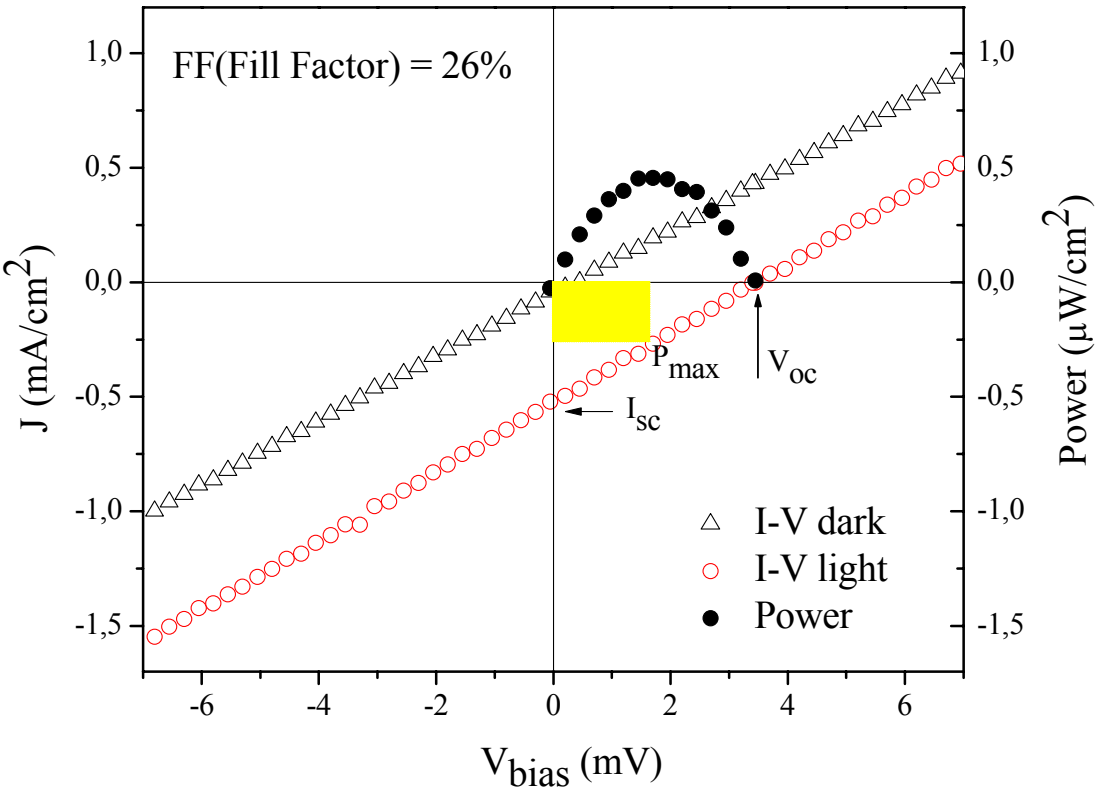

Fig. 29. I-V characteristic of a MWCNTs/SiO_2/Si device under illumination with a solar simulator (AM 1.5). The characteristic parameters are indicated: short circuit current I_{sc}, open circuit voltage *Voc*, maximum power available from device P_{max}, and fill factor *FF*. (For cleamess the sign of power has been reversed)

References

[1] P. Castrucci, F. Tombolini, M. Scarselli, E. Speiser, S. Del Gobbo, W. Richter, M. De Crescenzi, M. Diociaiuti, E. Gatto, M. Venanzi, *Appl. Phys. Lett.* **89**, 253107 (2006).

[2] M. De Crescenzi, F. Tombolini, M. Scarselli, E. Speiser, P. Castrucci, M. Diociaiuti, S. Casciardi, E. Gatto, M. Venanzi, *Surf. Sci.*, **601**, 2810 (2007).

[3] H. J. Kuhn, S. E. Braslavsky, R. Schmidt, *Pure Appl. Chem.*, **61**, 187 (1989).

[4] I. Robel, B. Bunker, P. V. Kamat, *Adv. Mater.*, **17**, 2458 (2005).

[5] F. Vietmeyer, B. Seger, P. V. Kamat , *Adv. Mater.* **19**, 2935 (2007).

[6] G. M. Aminur Rahman, D. M. Guldi, E. Zambon, L. Pasquato, N. Tagmatarchis, M. Prato, *Small* **1**, 527 (2005).

[7] Y. Cho, C. Kim, H. Moon, Y. Choi, S. Park, C.K. Lee, S. Han, *Nanoletters*, **8**, 81 (2007).

[8] A. N. Androitis, M. Menon, G. E. Froudakis, *Appl. Phys. Lett.* **76**, 3890 (2000).

[9] (a) C. Bittencourt, A. Felten, J. Ghijsen, J.J. Pireaux, W. Drube, R. Enri, G. Van Tendeloo, *Chem. Phys. Lett.* **436**, 368 (2007); (b) C. Bittencourt, A. Felten, B. Douhard, J.-F. Colomer, G. Van Tendeloo, W. Drube, J. Ghijsen, J. J. Pireaux, *Surf. Sci.* **601**, 2800 (2007).

[10] B. Xue, P. Chen, Q. Hong, J. Lin, K. L. Tan, *J. Mater. Chem.* **11**, 2378 (2001).

[11] K. Kong, S. Han, J. Ihm, *Phys. Rev. B* **60**, 6074 (1999).

[12] M. De Crescenzi, M. Diociaiuti, L. Lozzi, P. Picozzi, S. Santucci, *Solid State Commun.* **74**, 115 (1990).

[13] S. Di Nardo, L. Lozzi, M. Passacantando, P. Picozzi, S. Santucci, M. De Crescenzi, *Surf. Sci.* **922**, 307 (1994).

[14] S. M. Sze, "Physics of Semiconductor Devices", John Wiley & Sons (New York) 1969.

[15] M.S. Fuhrer et al., Crossed Nanotube Junctions, *Science* **288**, 494 (2000)

[16] J.U. Lee, Photovoltaic effect in ideal carbon nantube diodes. *Appl. Phys. Lett.* **87**, 073101 (2005).

[17] Freitag, M.; Martin, Y.; Misewich, J. A.; Martel, R.; Avouris, P. H., *Nanoletters*, **3**, 1067 (2003).

[18] J. U. Lee, P. P. Gipp, and C. M. Heller, *Appl. Phys. Lett.* **85**, 145 (2004).

[19] Castrucci, P.; Scarselli, M.; De Crescenzi M.; El Khakani, M. A.; Rosei, F.; Braidy, N.; Yi J.-H. *Appl. Phys. Lett*. **85**, 3857 (2004).

[20] Stewart, D. A.; Leonard, F. *Phys. Rev. Lett.* **93**, 107401 (2004).

[21] Kumar, S.; Murthy, J. Y.; Alam, M. A. *Phys. Rev. Lett.*, **95**, 066802 (2005).

[22] M. Passacantando, F. Bussolotti, V. Grossi, S. Santucci, A. Ambrosio, M. Ambrosio, G. Ambrosone, V. Carillo, P. Maddalena, E. Perillo, A. Raulo, *Appl. Phys. Lett.*, **93**, 051911 (2008).

[23] M. Born, E. Wolf, "*Principle of optics*", Pergamon Press, sixth Edition 1980

[24] B. Delley, *J. Chem. Phys.* **92**, 508 (1990).

[25] B. Delley, *J. Chem. Phys.* **113**, 7756 (2000).

[26] A. Mohite, S. Chakraborty, P. Gopinath, G. U. Sumanasekera, and B. W. Alphenaara, *App. Phys. Lett.*, **86**, 061114 (2005).

Conclusion

The main activities of the work described in this thesis have been devoted to obtain a controlled synthesis of MWCNTs as a function of their application and to study their behaviour in photo-to-electrical conversion devices. A deeper investigation of the underlying physical mechanisms relevant to photocurrent generation has been performed to give the proper interpretation to the experimental results.

MWCNTs have been synthesised by thermal CVD varying the experimental growth parameters. By using techniques of morphological and structural characterization, it has been possible to fix the synthesis parameters to obtain controlled MWCNTs structures on specific substrates. The evaporated layer of catalyst has been correlated by STM measurements with catalyst nanoparticles diameter that, in turn, influences the size of MWCNTs. Then by SEM techniques, the density and 3D orientation of MWCNTs have been investigated and firstly correlated to the main growth parameter (T_{sub}, P_{ch}, and C_2H_2 flux). To completely characterize the nanotubes structures, TEM investigation has been performed. The quality of synthesised MWCNTs is very good: high crystallinity (i.e. nature and local order of chemical bonds are almost equal to that of graphite), carbonaceous impurities almost absent, few structural defects. Moreover, the statistical distribution of external (internal) diameter and number of walls has been performed by analysing TEM micrographs. It has been succeeded in decoration of external wall of nanotubes using metal nanoparticles, which form a hybrid system where MWCNTs maintain their graphitic character. Finally, selective MWCNTs deposition on patterned substrates has been carried on. It has been demonstrated the capability to obtain different 3D architectures on the basis of the desired MWCNTs applications.

Experiments of photochemical current generation on MWCNTs growth on SiO_2/Si substrate have been performed. They have confirmed the capability of MWCNTs to generate a current of electrons under light irradiation, despite their close similarity to metallic graphite. EELS spectra show a shoulder at energies 2-4 eV, below the typical plasmon π -π^* peak for HOPG. That can be associated, similarly to SWCNTs, to the

presence of van Hove singularities in electronic DOS. These transitions allow the generation upon illumination of an exciton. Successively, the electrolyte inside the chemical cell separates the charges. Moreover, the presence of localized Schottky barriers inside a single MWCNT (among the semiconductive and metallic walls) and between different MWCNTs induces an increased carriers recombination time and promotes the diffusion of the optically-excited electrons towards the electrode, and the interaction of the optically-excited holes with the electrolyte, respectively.

MWCNTs have been decorated with Cu nanoparticles and their photochemical response has been studied and compared with that of bare nanotubes. The combination of MWCNTs with electron-donor groups constituted by small metal nano-particles is an innovative concept in the context of photovoltaic systems. It has been demonstrated the capability of Cu nano-particles to significantly modify the electronic properties of the entire hybrid system, without perturbing the graphitic character of the nanotube walls. The quantum efficiency of the hybrid system increases over the entire spectrum. At about 3.2 eV, *QE* increases from 1% to 4.5%. Two models have been proposed: the first indicates the localization of the electronic levels, due to the reducing size of metal particles, as responsible for the additional charge measured in photocurrent; the second attributes to Cu nanoparticles the generation of a high local electric field situated on the wall of the carbon nanotube. That enhances the photocharge separation inside the nanotubes, thus facilitating the collection of the produced e-h carriers at the electrode.

Complementary experiments of photocurrent have been performed assembling a solid-state device. The experimental apparatus has been set up and the first measurements have been carried on. Also without the presence of the electrolyte, a steady-state current flows within the MWCNT/SiO_2/Si device under modulated irradiation. This is an interesting result and confirms the presence of Schottky barriers inside the sample MWCNT and between different nanotubes. This becomes the charge separation mechanism alternative to the chemical cell electrolyte. Finally, the flux of the photogenerated charges towards the electrodes is driven by formation of two asymmetric Schottky barriers at the interfaces between the nanotubes and the metallic electrodes.

The *QE* spectrum shows a broad feature located at about 1.8 eV and it extends over a wide energy region similarly to that measured in polycrystalline silicon solar cells. This differs from the results found in literature and from the experimental absorbance of our MWCNTs. This discrepancy has been explained calculating the absorbance and verifying that the effect of nanotube substrate cannot be neglected.

DOS calculations have been performed within Density Functional Theory for single as well as multiwall carbon nanotubes. Starting from SWCNT, the number of singularities increases resulting in a smoother DOS when larger nanotubes are added round the first one. The total density of states of the a 4 walls nanotube (4WCNT) structure is very close to the bare sum of the DOS of each the for SWCNT composing the structure, showing that there is a rather small interaction between nanotubes belonging to the same multi-walled structure. This confirms the previous speculation and experimental results on the presence in MWCNTs DOS of van Hove singularities that induce the photogeneration process under study. It is worth to notice that, from such calculations, the Thomas-Fermi static screening length has been evaluated, finding that even metallic nanotubes may give rise to photocurrent generation, due to a poor screening of the e-h pair.

Considering an approximation only for 4WNTs, from the calculated DOS, the dielectric constant has been obtained. This is useful to calculate the absorbance for several thicknesses of a 4WCNTs film. The result is a monotonic function increasing towards violet and near-ultraviolet photon energy. Only taking into account a silicon slab of 10 μm, the absorbance reproduces the features of the experimentally measured *QE*, characterized by a maximum shifting towards the red region (best agreement for a theoretical 4WCNT film of 100 nm thick). This result demonstrates that MWCNTs are able to locally create p-n and/or Schottky junctions with the silicon substrate underneath giving rise to extended depletion layer, and enhancing of a 10^3 factor the *QE* of the bare SiO_2/silicon substrate.

The difference in the photocurrent spectra obtained in chemical cells is probably due to the occurring of photogeneration mechanism on the surface of the MWCNTs film in the proximity to the electrolyte.

Comparison with a MWCNTs decorated by Cu nanoparticles has been performed also for this kind of solid-state experiment, finding approximately the same results of photochemical cells.

Finally, a first measurement of the performance of a MWCNTs/SiO_2/Si device as PV cell has been performed by using a solar simulator. The I-V characteristic is not the expected well-shaped curve of a PV cell, but it shows that also our device can operate as an active power supply element under solar illumination. The results is encouraging also if the value of the obtained *FF* characteristic parameter is lower than those of the present silicon PV cells.

Concluding, the work of this thesis has succeeded in realizing controlled (selective) growth of MWCNTs on different (patterned) substrate as a function of specific applications. A strategy for the synthesis, structural and morphological characterization has been set up. The experimental evidences on photocurrent generation provide insights into the peculiar photoabsorption properties of multiwall carbon nanotubes and relative mechanism of photocurrent generation.

APPENDIX A

Scanning Tunnelling Microscopy

In the early 1980's two IBM scientists, Binnig & Rohrer, developed a new technique for studying surface structure - Scanning Tunnelling Microscopy (STM). This invention was quickly followed by the development of a whole family of related techniques which, together with STM, may be classified in the general category of Scanning Probe Microscopy (SPM) techniques. All of the techniques are based upon scanning a probe, typically called the tip in STM since it literally is a sharp metallic tip, just above a surface whilst monitoring some interaction between the probe and the surface. The interaction that is monitored in STM is the tunneling current between a metallic tip and a conducting substrate which are in very close proximity but not actually in physical contact.

For these techniques to provide information on the surface structure at the atomic level:

1. the position of the tip with respect to the surface must be very accurately controlled (to within about 0.1 Å) by moving either the surface or the tip.
2. the tip must be very sharp - ideally terminating in just a single atom at its closest point of approach to the surface.

The name of the STM technique arises from the quantum mechanical tunnelling-type mechanism by which the electrons can move between the tip and substrate. Quantum mechanical tunnelling permits particles to tunnel through a potential barrier which they could not surmount according to the classical laws of physics - in this case electrons are able to traverse the classically-forbidden region between the two solids. In this model, the probability of tunnelling is exponentially-dependent upon the distance of separation between the tip and surface: the tunnelling current is therefore a very sensitive probe of this separation. STM is able to measure the local density of states of a material at it surface as a function of lateral (x-y) position on the sample surface and energy. Within the sample, each individual electron has a specific energy

level. Only a certain number of electrons may occupy any given energy level at any one time. The distribution that gives the number of electrons allowed per energy level as a function of which energy level you consider is called density of states which can be abbreviate as DOS. The DOS is a very useful quantity to be able to measure since it can be used to derive a wealth of information about the crystal's properties. The DOS can vary as a function of position in the crystal which means that one can define a local density of states (LDOS). LDOS is then a quantity which depends on both energy and on position, LDOS(x, y, E).

An STM can typically measure and control the current that flows between the tip and the sample (I), the bias voltage between the tip and the sample (V), the xy (in sample plane) position of the tip, and the z (perpendicular to sample plane) distance between the tip and sample.

Using these variables an STM is able to measure the LDOS of a material as function of position on the surface (controlled by where the tip is above the surface) and as a function of energy (controlled by the bias voltage between the tip and sample). The LDOS is proportional to the differential increase in tunnelling current given a differential increase in bias voltage or in other words one can measure the LDOS by measuring dI/dV.

Imaging of the surface topology may be carried out in one of two ways:

1. in constant height mode (in which the tunnelling current is monitored as the tip is scanned parallel to the surface) (see Fig. 1).
2. in constant current mode (in which the tunnelling current is maintained constant as the tip is scanned across the surface) (see Fig. 2)

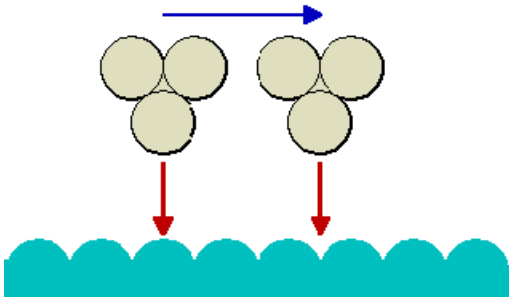

Fig. 1. *Constant height mode*. If the tip is scanned at what is nominally a constant height above the surface, then there is actually a periodic variation in the separation distance between the tip and surface atoms. At one point the tip will be directly above a surface atom and the tunnelling current will be large whilst at other points the tip will be above hollow sites on the surface and the tunnelling current will be much smaller.

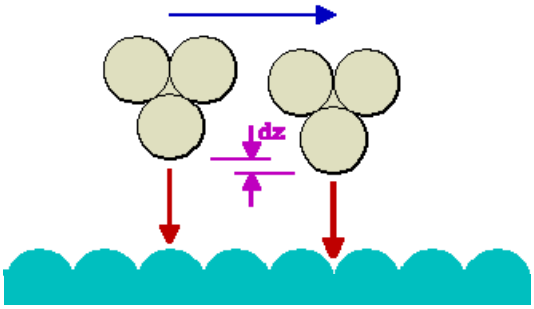

Fig. 2. *Constant current mode*. In practice, however, the normal way of imaging the surface is to maintain the tunnelling current constant whilst the tip is scanned across the surface. This is achieved by adjusting the tip's height above the surface so that the tunnelling current does not vary with the lateral tip position. In this mode the tip will move slightly upwards as it passes over a surface atom, and conversely, slightly in towards the surface as it passes over a hollow.

A scanning tunneling microscope or STM is a tool to look at individual atoms on the surface of a material. The basic components of the microscope setup are:

- the sample you want to study
- a sharp tip to be placed in very close proximity to the sample
- a mechanism to control the location of the tip in the x-y plane parallel to the sample surface (XY scan control)
- a feedback loop to control the height of the tip above the sample (the z-axis)

The Sample - The ideal sample is flat and clean, just a slice through a plane in the crystal structure of a material. It is fixed in place throughout the measurement. Because the STM works by a current to or from the sample, the sample must conduct electricity.

The Tip - The tip is just a very sharp needle, so sharp that it terminates in a single atom. It is not actually touching the sample, rather it is approximately a few Ångstroms (~ atomic diameters) away. The tip is held at zero voltage, or "ground". Meanwhile, a bias voltage is placed on the sample, on the order of a few millivolts to a few volts. This voltage bias induces a "tunnelling" current to flow between the tip and the sample. This current is exponentially dependent upon the distance between the tip and the sample which means that for a small change in the distance between the tip and the sample the current changes.

The XY Scan Control - The tip can be scanned across the surface using a crystal called a piezoelectric which changes its size by very small amounts when a voltage is applied to it. As the tip is moved in the x or y direction along the surface of the sample, the current will vary according to whether the tip is right on top of an atom (smaller distance), or on top of a space between atoms (larger distance). So an individual atom can be "seen" as an increase in the tunnelling current as the XY scan control moves the tip across the surface of the sample.

The Feedback Control - In practice, since current falls off exponentially with distance, the current when the tip is on top of an atom is much larger than the current when the tip is between atoms. We could just record the current as a function xy position on the surface, but because the current is exponential in the tip-sample distance this would give a distorted image in which the atomic peaks would look much higher than they actually are.

What we are really interested in is the actual height of atoms on the sample surface. To measure this height it is employed a feedback loop to keep the current constant by adjusting the height of the tip. The height of the tip is controlled by a piezoelectric crystal. A piezoelectric crystal is a material which expands linearly when a voltage is placed across it. The expanding crystal pushes the tip closer to the sample. So the voltage needed to expand the piezo to keep the current constant varies linearly with the actual height of the atoms on the sample. Now by reading the feedback voltage, we can just read directly the height of the tip.

APPENDIX B

Scanning Electron Microscopy

Electron Microscopes were developed due to the limitations of Light Microscopes imposed by the physics of light to 500x or 1000x magnification and a resolution of 0.2 micrometers. In the early 1930's this theoretical limit had been reached and there was a scientific desire to see the fine details of the interior structures of organic cells. This required 10,000x plus magnification which was just not possible using Light Microscopes. The Transmission Electron Microscope (TEM) was the first type of Electron Microscope to be developed and is patterned exactly on the Light Transmission Microscope except that a focused beam of electrons is used instead of light to "see through" the specimen. It was developed by Max Knoll and Ernst Ruska in Germany in 1931. The first Scanning Electron Microscope (SEM) debuted in 1942 with the first commercial instruments around 1965.

When a high-energy (~keV) electron beam interacts with a specimen then a wide range of secondary signals are formed which can give interesting information of the sample (Fig.1). In a scanning electron microscope (SEM) mainly the secondary electrons (SE), backscattered electrons (BSE) and characteristic X-rays are analysed (EDX). If the sample is thin enough the elastically scattered electrons can be investigated in a transmission electron microscope (TEM).

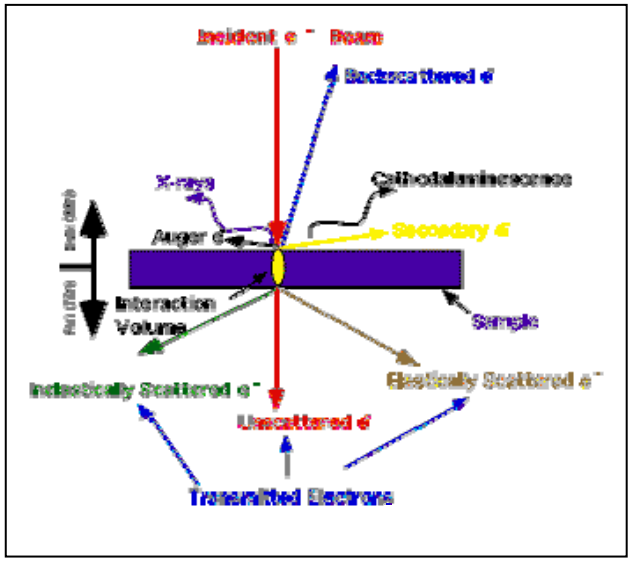

Fig. 1. Signal generated when a high-energy electron beam interacts with a thin specimen. Most signals can be detected in a SEM or TEM.

In the following tables are summarized the fundamental thin specimen interactions (Table 1).

Table 1. Principles of thin specimen interaction.

Thin* Specimen *Interactions	***Source***	***Utilization***
Unscattered Electrons	Incident electrons which are transmitted through the thin specimen without any interaction occurring inside the specimen.	The transmission of unscattered electrons is inversely proportional to the specimen thickness. Areas of the specimen that are thicker will have fewer transmitted unscattered electrons and so will appear darker, conversely the thinner areas will have more transmitted and thus will appear lighter.
Elasticity Scattered electrons	Incident electrons that are scattered (deflected from their original path) by atoms in the specimen in an elastic fashion (no loss of energy). These scattered electrons are then transmitted through the remaining portions of the specimen.	All electrons follow Bragg's Law and thus are scattered according to Wavelength=2*Space between the atoms in the specimen*sin(angle of scattering). All incident electrons have the same energy (thus wavelength) and enter the specimen normal to its surface. All incidents that are scattered by the

		same atomic spacing will be scattered by the same angle. These "similar angle" scattered electrons can be collated using magnetic lenses to form a pattern of spots; each spot corresponding to a specific atomic spacing (a plane). This pattern can then yield information about the orientation, atomic arrangements and phases present in the area being examined.
Inelastically Scattered Electrons	Incident electrons that interact with specimen atoms in a inelastic fashion, loosing energy during the interaction. These electrons are then transmitted trough the rest of the specimen	Inelasticaly scattered electrons can be utilized for Electron Energy Loss Spectroscopy: the inelastic loss of energy by the incident electrons is characteristic of the elements that were interacted with. These energies are unique to each bonding state of each element and thus can be used to extract both compositional and bonding (i.e. oxidation state) information on the specimen region being examined.

SEM (Scanning Electron Microscopy)

In a SEM an electron beam generated by field- or thermo emission is scanned over the specimen. The backscattered or secondary electrons are counted with an appropriate detector and are imaged on a screen. If the electrons are scattered inelastically then they are scattered at the electrons of the target material. Compared to impacts with the nucleus of the atom the change in direction of the electrons can be neglected provided the electron energy is not to low. The electrons are loosing their energy continuously through the interaction with the electrons of the target. The loss in energy *dE* per distance *ds* can be described by the *Bethe* equation [1]:

1 $$-\frac{dE}{ds} = \frac{e_0^4}{8\pi e_0^2}\frac{NZ}{E}\ln\left(\sqrt{\frac{e}{2}}\frac{E}{J}\right)$$

where N is the number of atoms, Z the atomic number of the target material, J the ionisation energy of the target and E the Energy of the incident electron. Through this interaction the excited secondary electrons can escape the outermost layer of the target material and they can be detected. Fig.2 shows how a typical SEM functions.

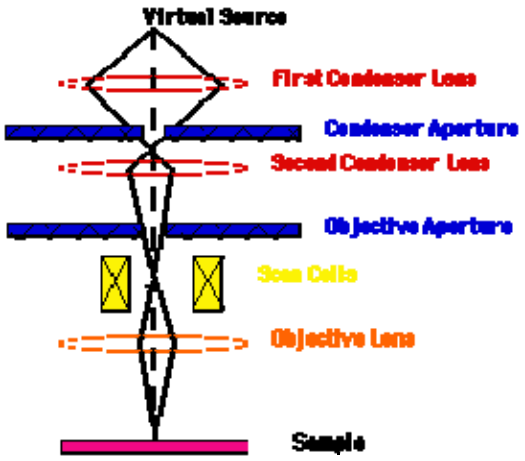

Fig. 2. Schematic picture to illustrate how a SEM microscopy works. See text below for details.

The "Virtual Source" at the top represents the electron gun producing a stream of monochromatic electrons.

1 The stream is condensed by the first condenser lens (usually controlled by the "coarse probe current knob"). This lens is used to both form the beam and limit the amount of current in the beam. It works in conjunction with the condenser aperture to eliminate the high-angle electrons from the beam
2 The beam is then constricted by the condenser aperture (usually not user selectable), eliminating some high-angle electrons
3 The second condenser lens forms the electrons into a thin, tight, coherent beam and is usually controlled by the "fine probe current knob"
4 A user selectable objective aperture further eliminates high-angle electrons from the beam
5 A set of coils then "scan" or "sweep" the beam in a grid fashion (like a television), dwelling on points for a period of time determined by the scan speed (usually in the microsecond range)
6 The final lens, the Objective, focuses the scanning beam onto the part of the specimen desired.

7 When the beam strikes the sample (and dwells for a few microseconds) interactions occur inside the sample and are detected with various instruments
8 Before the beam moves to its next dwell point these instruments count the number of interactions and display a pixel on a CRT whose intensity is determined by this number (the more reactions the brighter the pixel).
9 This process is repeated until the grid scan is finished and then repeated, the entire pattern can be scanned 30 times per second.

TEM (Transmission Electron Microscopy)

The imaging ray path in a TEM is analogous to that of an optical microscope. The operation of the objective lens allows the imaging of the object in the corresponding image plain by focusing of electrons starting with different directions from individual object points to the corresponding image points (Fig. 3). Additionally in the back focal plane of the objective all those electrons are focused to one point, which started in the same direction from any point in the object leading to the diffraction pattern of the object. A bright field image contrast can be obtained by arranging a contrast aperture in the back focal plain in order to eliminate all electrons, which are scattered and diffracted, respectively into large angles. Depending on the setting of the intermediate lens one may image either the back focal plane or the image plane of the objective lens in the image plane of the projector lens. Thus one obtains either the diffraction pattern or the image of the specimen on the
viewing screen.

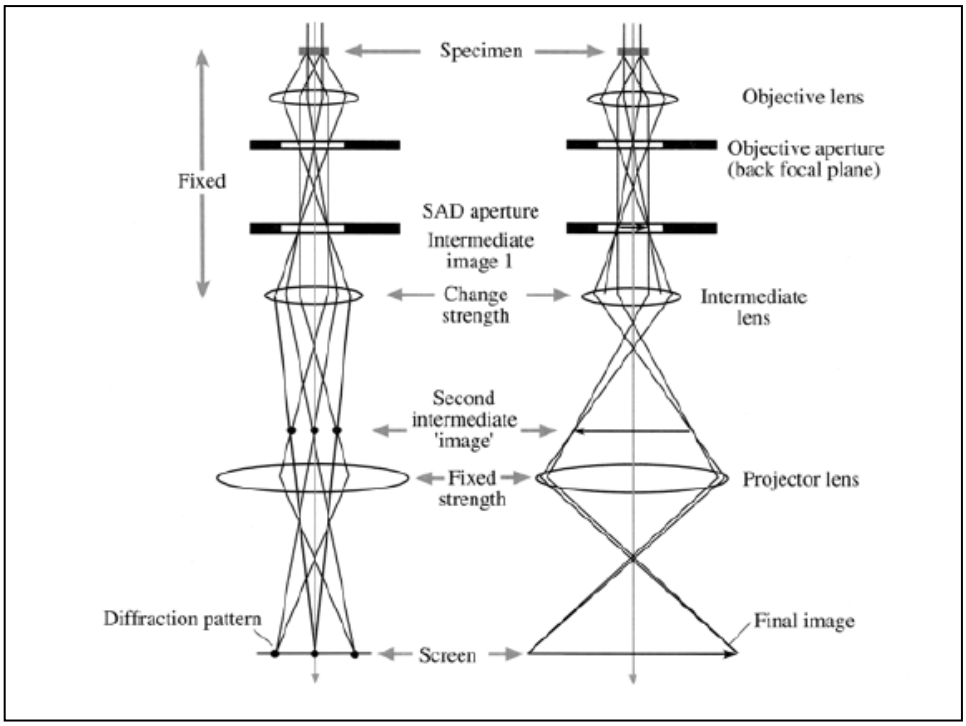

Fig. 3. The two basic operations of a TEM: projecting the diffraction pattern on the viewing screen (left) or projecting the image on the screen (right). The intermediate lens select the back focal- or the image plane of the objective lens as its object [2].

The relation between the accelerating voltage U and the electron velocity v is given by [1]:

2 $$e_0 U = \frac{m_o c^2}{\sqrt{a - (v/c)^2}} - m_o c^2$$

where m_0 is the rest mass of the electron and c the velocity of light in vacuum. The wavelength λ attributed to an electron with velocity v is given by the de Broglie relation:

3 $$\lambda = \frac{h}{m_0 v}\sqrt{1-(v/c)^2}$$

where h is Planck's constant. An electron with a kinetic energy of E_{kin} = 100 keV has a velocity v of ~ 55% light velocity and a wavelength of λ = 3.7 pm.

The inelastically scattered electrons are not focused in the image plane because of the chromatic aberration of the objective lens.

There are mainly three different ways to form the contrast [1]:

- ***scattering-absorption contrast***: Only the unscattered electrons or the electrons scattered through extremely small angles contribute to the image. The scattered electrons are removed form the imaging beam by insertion of a contrast aperture in the back focal plane of the objective lens or even unintentionally due to the effect of the spherical aberration of the objective lens. This image mode leads to the so-called bright field (BF) image (Fig.4 left). The removal of the scattered electrons from the beam by the objective aperture produces the same effect as absorption within the specimen. At low resolution the image can be described to a good approximation as two dimensional projection of the mass density into the plane normal to the beam direction.
- ***diffraction contrast***: Only the scattered electrons or part of them are used for the image formation. The unscattered electrons are e.g. stopped by the displacement of the contrast aperture. An image formed in this way is called a dark field (DF) image (Fig. 4 right).
- ***phase contrast*:** In high resolution TEM the image contrast is mainly caused by the interference of the primary beam (unscattered electrons) with the scattered electrons in the image plane leading to a bright field image. In TEM the phase contrast is formed by the phase shift relationship introduced by the spherical aberration and the aberration of defocusing. The refractive power of the outer zones of the objective lens is higher than that of the inner ones, thereby causing a phase shift between the undiffracted beam and the diffracted beams. The phase shift can be changed by an appropriate defocus in order to adjust the image phase contrast.

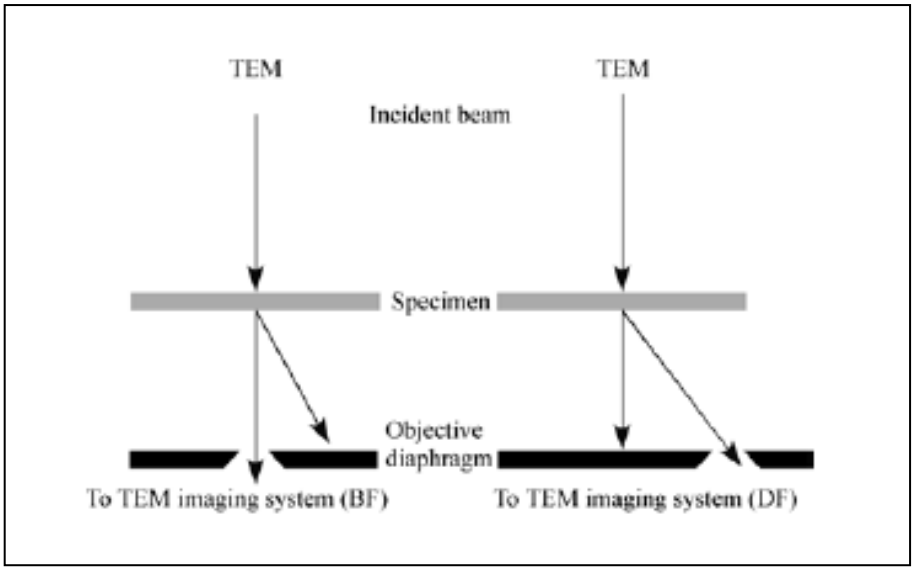

Fig. 4. Comparison of the use of an objective aperture in TEM to select the direct (left) or the scattered electrons (right) forming bright field (BF) and dark field (DF) images respectively [2].

[1] H. Bethge, J. Heydenreich, Electron Microscopy in Solid State Physics, Elsevier (Amsterdam, Oxford, New York) 1987.

[2] D.B. Williams, C.B. Carter, "*Transmission Electron Microscopy; Basics"* , Plenum Press (New York, London), 1996.

APPENDIX C

Electron Energy Loss Spectroscopy (EELS)

Electron Energy Loss Spectroscopy (EELS) concerns the analysis of energy spreading of initially almost monoenergetic electrons, after their interaction with the sample. The technique is frequently used in association with Transmission Electron Microscopy (TEM) and interaction takes place inside the specimen. Measuring the energy distribution of electrons that have passed through a thin specimen can be obtained informations about its structure. The spectral energy resolution is largely determined by the energy width of the electron source: 1 - 2 eV for a thermionic source, 0.5 to 0.7 eV for a field-emission gun and 0.1 - 0.2 eV for a FEG (Field Emission Gun) followed by a monochromator [1].
The electrons impinging on the sample may lose energy by a variety of mechanisms. These losses can reveal the composition of the sample in TEM.

-Plasmon losses are a frequent cause of energy loss. Plasmons are collective excitations of the electron gas in the material and are typically several electron Volts in magnitude (5-30 eV).

-Phonon losses can also occur, which are much smaller (less than 0.1 eV), and the energy spread of the monoenergetic beam must be particularly small to detect such losses. Phonons are quantized sound waves within the solid.
A typical energy loss spectrum is divided in two regions at low and at high energy.

Low Energy Loss:

For very thin specimens, the most prominent feature is the zero-loss peak that is due to unscattered electrons that are transmitted without any interaction with the specimen. (area I_0 , representing purely *elastic* scattering, see Fig.1). The second contribution includes the plasmon peak, due to *inelastic* scattering by outer-shell

(valence) electrons in the specimen, it is centred around a plasmon energy E_p, generally in the range 10-30 eV. Plural scattering of the transmitted electrons gives rise to additional peaks, at multiples of E_p.

The plasmon losses just mentioned are called "volume plasmons" because they arise from the interaction with the electrons in the bulk of the specimen. The incident electrons, however, can also originate a longitudinal wave of charge density which travels along the surface and is referred to as "surface plasmon". In the simplest situation, the vacuum-metal interface, the energy E_s of the surface plasmon peak in the low-loss spectrum is:

2.1 $$E_s = E_p / \sqrt{2}$$

while, in the slightly more general case, dielectric-metal interface Eq. 2.1 becomes:

2.2 $$E_s = E_p / \sqrt{1+\varepsilon_1}$$

where ε_1 is the real part of the dielectric function. Generally surface plasmons have about half the energy of bulk plasmon and their peak are much less intense than the volume plasmon peak, even in the thinnest specimen.

High Energy Loss:

At higher energy loss, ionization edges occur due to inelastic excitation of inner-shell (*core*) electrons. They are superimposed on a falling background representing the tail of lower-loss inelastic processes, which usually approximates to a power law:

2.3 $$background \sim A \cdot E^{-r}$$

where A and r are constants within a limited range of energy loss E . The threshold energy of each edge is the binding energy of the corresponding atomic shell and is tabulated for all elements and electron shells (K, L, M, etc.), allowing elements present in the specimen to be identified. The energy-loss spectrum also contains *fine structure*, in the form of intensity oscillations or local peaks.

Extended energy-loss fine structure (EXELFS) have a weaker intensity modulation starting at 50 eV or more from the ionization edge and can be analyzed to give the distance of nearest-neighbour atoms.

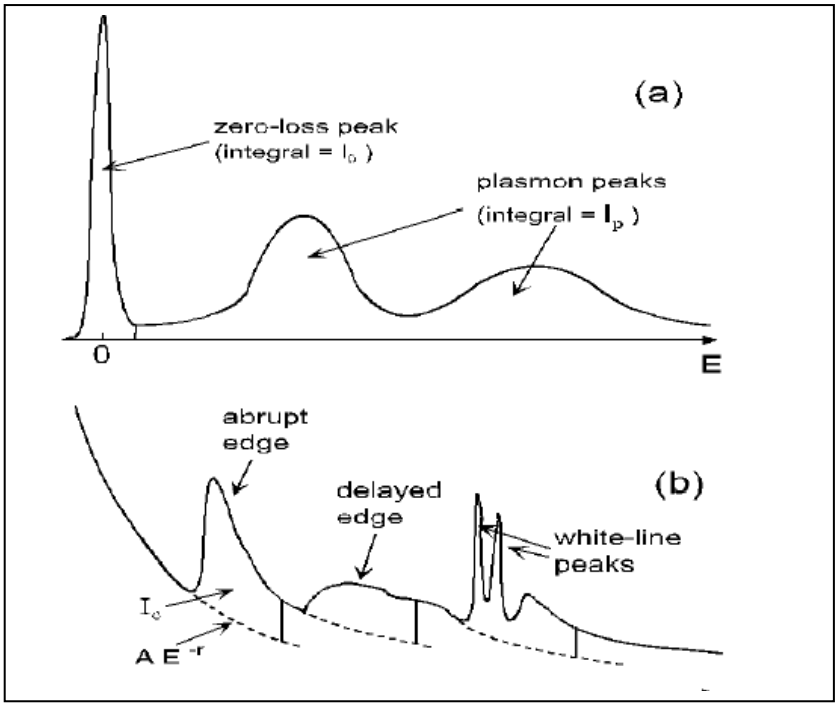

Fig. 1. (a) Low-loss spectrum and (b) the core-loss region showing several basic shapes of ionization edge, each superimposed on a spectral background (dashed curves). Image taken from [2].

[1] R.F. Egerton, '*Electron Energy-Loss Spectroscopy in the Electron Microscope*', 2nd edition, Plenum, New York, 1996.

[2] F. Hofer, '*Microbeam Analysis*', San Francisco Press, San Francisco, 1991; p. 255.

Acknowledgments

I wish to thank some of the people who helped me in this PhD work. First of all, a special thank to my tutor Prof. M. De Crescenzi for all his precious teachings and his active presence during all my path. I thank also Dr. P. Castrucci and Dr. M. Scarselli for their help in my research activity and the clarifying scientific discussions.

Working in their group has been very pleasant and it has represented an enriching experience from the professional and personal points of view.

I thank Dr. P. Ascarelli and Dr. E. Cappelli for having allowed me to attend PhD school during my research activity at CNR.

Finally I would like to thank the people that collaborated to the characterization of CNTs studied in this thesis:

Dr. F. Tombolini, Physics Department of University "Tor Vergata", for the CNTs size statistical analysis;

Dr. E. Speiser and Dr. S. Del Gobbo for photoconductivity set-up and related measurements;

Dr. M. Diociaiuti of ISS (National Institute of Health) and Dr. S. Casciardi of ISPESL (National Institute for Occupational Safety and Prevention), for TEM and EELS measurements on CNTs;

Prof. M.Venanzi and Dr. M.Gatto of the Chemical Department of University "Tor Vergata" for photocurrent measurements;

Prof. A. Di Carlo of the Electronic Engineering Department of University "Tor Vergata" for photovoltaic characterization.

List of Publications

[1] P. Castrucci, F. Tombolini, M. Scarselli, **C. Scilletta**, M. De Crescenzi, M. Diociaiuti, S. Casciardi, F. Rosei, and M. A. El Khakani,
"Comparison of the Local Order in Highly Oriented Pyrolitic Graphite and Bundles of Single-Wall Carbon Nanotubes by Nanoscale Extended Energy Loss Spectra"
J. Phys. Chem. C, 2009, **113** (12), 4848-4855

[2] M. Scarselli, **C.Scilletta**, F. Tombolini, P. Castrucci, M. De Crescenzi, M. Diociaiuti, S.Casciardi , E. Gatto, M. Venanzi,
"Photon harvesting with multi wall carbon nanotubes"
Superlattices and Microstructures **46** , 340-346, 2009

[3] M. Scarselli, **C. Scilletta**, F. Tombolini, P. Castrucci, M. Diociaiuti, S. Casciardi, E. Gatto, M. Venanzi, M. De Crescenzi,
"Multiwall Carbon Nanotubes Decorated with Copper Nanoparticles: Effect on the Photocurrent Response"
J. Phys. Chem. C, 2009, **113** (14), 5860-5864

[4] S. Casciardi, F. Tombolini, M. Diociaiuti, P. Castrucci, M. Scarselli, **C. Scilletta**, M. De Crescenzi,
"Uso della microscopia elettronica per la caratterizzazione di nanotubi di carbonio a parete multipla prodotti con la deposizione da fase vapore."
Prevenzione Oggi – Prevention Today, Accepted for pubblication

[5] M.De Crescenzi, **C.Scilletta**, F.Tombolini, M.Scarselli, P.Castrucci
"Electronic and optoelectronic nanodevices based on carbon nanotubes"
Il Nuovo Saggiatore, Accepted for pubblication

In Progress

✓ M. A. El Khakani, V. Le Borgne, B. Aissa, F. Rosei, **C. Scilletta**, E. Speiser, M. Scarselli, P. Castrucci and M. De Crescenzi
"Photocurrent generation in random networks of multiwall-carbon-nanotubes grown by an "all-laser" process"
Submitted to *Appl. Phys. Lett*.

✓ **C. Scilletta**, E. Speiser, P. Castrucci, F. Tombolini, M. Scarselli and M. De Crescenzi, M. Simeoni, A. Continenza, B. Delley,
"Photocurrent enhancement in multi wall carbon nanotubes/silicon devices"
To be submitted *Nanoletters*

✓ P. Castrucci, **C. Scilletta** , E. Speiser, M. Scarselli, M. De Crescenzi, A. Ronda and I. Berbezier,
"Enhanced quantum efficiency of silicon with Ge quantum dots"
Submitted to *Appl. Phys. Lett.*

Other Publications

[1] E. Cappelli**, C. Scilletta**, S. Orlando, V. Valentini, M. Servidori,
"Laser annealing of amorphous carbon films"
Applied Surface Science **255**, 5620 (2009)

[2] **C. Scilletta**, S. Orlando, M. Servidori, E. Cappelli, G. Conte, P. Ascarelli, "Role of growth temperature on nanostructure and field emission properties of PLD thin carbon films".
Appl Phys A **93**, 783 (2008)

[3] E. Cappelli, **C. Scilletta**, G. Mattei, V. Valentini, S. Orlando, M. Servidori, "Critical role of laser wavelength on carbon films grown by PLD of graphite"
Appl Phys A **93**, 751 (2008)

[4] E. Cappelli, **C. Scilletta**, M. Servidori , V. Valentini, S. Orlando, "Morphology, structure and density evolution of carbon nano-structures deposited by N-IR pulsed laser ablation of graphite",
Diamond and Related Materials **17**, 1476 (2008)

[5] E. Cappelli, S. Orlando, M. Servidori, **C. Scilletta**, "Nano-graphene structures deposited by NIR pulsed laser ablation of graphite on Si"
Applied Surface Science **254** (2007) 1273-1278

[6] E. Cappelli, S. Orlando, V. Morandi, M. Servidori, **C. Scilletta** , "Nano-graphene growth and texturing by Nd:YAG pulsed laser ablation of graphite on Silicon"
Journal of Physics: Conference Series ***59*** *(2007) 616–624*

[7] **C. Scilletta**, M. Servidori, L. Barba, E. Cappelli, S. Orlando, and P. Ascarelli, "Influence of Temperature on Nano-Graphene Structuring of PLD Grown Carbon Films. An X-ray Diffraction Study"
Advances in Science and Technology **48** (2006) 55-60, disponibile on line sul sito http://www.scientific.net

[8] D.M. Trucchi, **C. Scilletta**, E.Cappelli, P.G. Merli, S. Zoffoli, G. Mattei and P. Ascarelli, "Optimization of the Performance of CVD Diamond Electron Multipliers"
Diamond and Related Materials **15** (2006) 827-832

[9] **C. Scilletta**, M. Servidori, S. Orlando, E. Cappelli, L. Barba and P. Ascarelli, "Influence of substrate temperature and atmosphere on nano-graphene formation and texturing of pulsed Nd:YAG laser-deposited carbon films"
Applied Surface Science **252** (2006) 4877-4881

[10] E. Cappelli, S. Iacobucci, **C. Scilletta**, R. Flammini, S. Orlando, G. Mattei and P. Ascarelli, F. Borgatti, A. Giglio, N. Mahne, and S. Nannarone, "Orientation tendency of PLD carbon films as a function of substrate temperature: a NEXAFS study"
Diamond and Related Materials **14** (2005) 959-964

[11] E. Cappelli**, C. Scilletta**, S. Orlando, R. Flammini, S. Iacobucci and P. Ascarelli, "Surface characterisation of nano-structured carbon films deposited by Nd:YAG pulsed laser deposition."
Thin Solid Films **482** (2005) 305-310